Controls on Ice Cliff Formation, Distribution and Characteristics on Debris-Covered Glaciers

Marin Kneib[1], Catriona Lousie Fyffe[2], Evan Stewart Miles[3], Shayna Lindemann[4], Thomas E. Shaw[1], Pascal Buri[1], Michael McCarthy[1], Boris Ouvry[5], Andreas Vieli[6], Yota Sato[7], Philip D. A. Kraaijenbrink[8], Chuanxi Zhao[9], Peter Molnar[10], Francesca Pellicciotti[10], Peter Moore[11], Martin Kirkbride[12], Philip Deline[13], Owen King[14], Doug Benn[15], and Neil Glasser[16]

[1]Swiss Federal Institute for Forest, Snow and Landscape Research
[2]Northumbria University
[3]Swiss Federal Research Institute WSL
[4]High Mountain Glaciers and Hydrology Group, Swiss Federal Institute, WSL, Birmensdorf, Switzerland.
[5]Institute of Geography, University of Zurich
[6]University of Zurich
[7]Graduate School of Environmental Studies, Nagoya University
[8]Utrecht University
[9]Institute of Tibetan Plateau Research, Chinese Academy of Sciences
[10]ETH Zurich
[11]Iowa State University
[12]University of Dundee
[13]Laboratoire Edytem
[14]University of St Andrews
[15]Department of Geography and Sustainable Development, University of St Andrews
[16]Aberystwyth University

December 8, 2022

Abstract

Ice cliff distribution plays a major role in determining the melt of debris-covered glaciers but its controls are largely unknown. We assembled a dataset of 37537 ice cliffs and determined their characteristics across 86 debris-covered glaciers within High Mountain Asia (HMA). We complemented this dataset with the analysis of 202 cliff formation events from multi-temporal UAV observations for a subset of glaciers. We find that 38.9% of the cliffs are stream-influenced, 19.5% pond-influenced and 19.7% are crevasses. Surface velocity is the main predictor of cliff distribution at both local and glacier scale, indicating its dependence on the dynamic state and hence evolution stage of debris-covered glacier tongues. Supraglacial ponds contribute to maintaining cliffs in areas of thicker debris, but this is only possible if water accumulates at the surface. Overall, total cliff density decreases exponentially with debris thickness as soon as debris gets thicker than 10 cm.

Controls on Ice Cliff Formation, Distribution and Characteristics on Debris-Covered Glaciers

M. Kneib[1, 2], Catriona Fyffe[3], Evan S. Miles[1], Shayna Lindemann[1], Thomas E. Shaw[1], Pascal Buri[1], Michael McCarthy[1], Boris Ouvry[4], Andreas Vieli[4], Yota Sato[5], Philip D.A Kraaijenbrink[6], Chuanxi Zhao[7,8], Peter Molnar[2], Francesca Pellicciotti[1,3]

[1] High Mountain Glaciers and Hydrology Group, Swiss Federal Institute, WSL, Birmensdorf, Switzerland.

[2] Institute of Environmental Engineering, ETH Zürich, Zürich, Switzerland

[3] Department of Geography and Environmental Sciences, Northumbria University, Newcastle upon Tyne, UK

[4] Department of Geography, University of Zurich, 8057 Zurich, Switzerland

[5] Graduate School of Environmental Studies, Nagoya University, Nagoya, Japan

[6] Utrecht University, Department of Physical Geography, PO Box 80115, 3508 TC, Utrecht, The Netherlands.

[7] College of Earth and Environmental Sciences, Lanzhou University, Lanzhou 730000, China

[8] State Key Laboratory of Tibetan Plateau Earth System, Environment and Resources (TPESER), Institute of Tibetan Plateau Research, Chinese Academy of Sciences

Corresponding author: Marin Kneib (marin.kneib@gmail.com)

Key Points:

- We derived an unprecedented dataset of 37537 ice cliffs and their characteristics across 86 debris-covered glaciers in High Mountain Asia
- We find that 38.9% of the cliffs are stream-influenced, 19.5% pond-influenced and 19.7% are crevasses
- Ice cliff distribution can be predicted by velocity as an indicator of both the dynamics and state of evolution of debris-covered glaciers

Abstract

Ice cliff distribution plays a major role in determining the melt of debris-covered glaciers but its controls are largely unknown. We assembled a dataset of 37537 ice cliffs and determined their characteristics across 86 debris-covered glaciers within High Mountain Asia (HMA). We complemented this dataset with the analysis of 202 cliff formation events from multi-temporal UAV observations for a subset of glaciers. We find that 38.9% of the cliffs are stream-influenced, 19.5% pond-influenced and 19.7% are crevasses. Surface velocity is the main predictor of cliff distribution at both local and glacier scale, indicating its dependence on the dynamic state and hence evolution stage of debris-covered glacier tongues. Supraglacial ponds contribute to maintaining cliffs in areas of thicker debris, but this is only possible if water accumulates at the surface. Overall, total cliff density decreases exponentially with debris thickness as soon as debris gets thicker than 10 cm.

Plain Language Summary

Debris-covered glaciers are common throughout the world's mountain ranges and are characterised by the presence of steep ice cliffs among the debris-covered ice. It is well-known that the cliffs are responsible for a large portion of the melt of these glaciers but the way they form, and as a result the controls on their development and distribution across glaciers remains poorly understood. Novel mapping approaches combined with high-resolution satellite and drone products enabled us to disentangle some of these controls and to show that the ice cliffs are generally formed and maintained by the surface hydrology (ponds or streams) or by the opening of crevasses. As a result, they depend both at the local and glacier scale on the dynamic state of

the glaciers as well as the evolution stage of their debris cover. This provides a pathway to better represent their contribution to glacier melt in predictive glacier models.

1 Introduction

Debris-covered glaciers are found in all mountain ranges (Scherler et al., 2018), and supraglacial debris extents and thickness are expected to increase in a warming climate (Compagno et al., 2022; Herreid & Pellicciotti, 2020; Stokes et al., 2007). However, despite considerable recent advances, modelling the mass balances of these glaciers remains challenging (Rounce et al., 2021). This is partly due to the presence of supraglacial ice cliffs, which melt up to 20 times faster than the surrounding debris-covered ice, therefore compensating for the relatively well constrained debris insulating effect (Anderson, Armstrong, Anderson, & Buri, 2021; Brun et al., 2018; E. S. Miles, Willis, et al., 2018; Reid & Brock, 2014; Sakai et al., 1998, 2002). In one catchment in High Mountain Asia (HMA) ice cliffs were shown to contribute 17+/-4% of the melt of the debris-covered ice (Buri et al., 2021). This has major implications for the mass balance of debris-covered glaciers (Pellicciotti et al., 2015) and their long-term evolution (Ferguson & Vieli, 2021; Racoviteanu et al., 2022).

While models accurately simulate the energy and mass balance contribution of individual ice cliffs (Buri et al., 2016; Kneib et al., 2022), their application at large spatial scales is limited by our understanding of the controls of ice cliff distribution. Indeed, estimates of ice cliff density are difficult to make (Anderson, Armstrong, Anderson, & Buri, 2021; Herreid & Pellicciotti, 2018; Kneib et al., 2020) and vary widely in time and space, between 1 and 15% of the debris-covered area (e.g. Falaschi et al., 2021; Kneib et al., 2021; Loriaux & Ruiz, 2021; Sato et al., 2021; Steiner et al., 2019; Watson et al., 2017). Remote sensing studies have shown that cliffs are often associated with ponds (Steiner et al., 2019; Watson, Quincey, Carrivick, et al., 2017), hinting at a preferential location of ice cliffs where lower glacier longitudinal gradient and surface velocities promote surface ponding (Bolch et al., 2008; Quincey et al., 2007; Quincey & Glasser, 2009; Racoviteanu et al., 2021; Reynolds, 2000; Sakai & Fujita, 2010; Salerno et al., 2012). Other limited observations indicate that ice cliffs preferentially develop at the confluence of glacial tributaries, in locations of high compressive strain rates, and areas of thinner debris (Anderson, Armstrong, Anderson, & Buri, 2021; Anderson, Armstrong, Anderson, Scherler, et al., 2021; Benn et al., 2012; Kraaijenbrink et al., 2016; Steiner et al., 2019; Watson, Quincey, Carrivick, et al., 2017). However, the lack of consistent observations of cliff distribution makes it difficult to include ice cliffs in predictive glacier models in a way that accounts for their spatial distribution and temporal evolution.

Ice cliff survival is inherently linked to debris stability, which is a function of local slope, debris thickness and water content, as well as undercutting by streams or ponds (Moore, 2018). The local slope can change in relatively short time scales with differential melt caused by heterogeneous debris thicknesses (Moore, 2021; Nicholson et al., 2018; Sharp, 1949), which results in the surface of debris-covered glaciers being particularly hummocky where the debris gets thicker than 20-30 cm (Bartlett et al., 2020; King et al., 2020). Slope undercutting and destabilisation by streams or ponds is expected to be one of the main triggers for ice cliff formation (Mölg et al., 2019; Röhl, 2006, 2008; Sakai & Takeuchi, 2000) and survival (Benn et al., 2001, 2012; Brun et al., 2016; Kneib et al., 2022; Sato et al., 2021; Watson, Quincey, Smith, et al., 2017). Other hypothesised cliff formation mechanisms include crevasse opening (Reid & Brock, 2014; Steiner et al., 2019) or the collapse of englacial conduits (Egli et al., 2021; Gulley et al., 2009; Immerzeel et al., 2014; E. S. Miles, Watson, et al., 2018; K. E. Miles et al., 2020; Sakai & Takeuchi, 2000), but these hypotheses have never been tested in a quantitative way.

In this study, we therefore 1) map ice cliffs across 86 glaciers in HMA, 2) determine their physical characteristics, 3) attribute their distribution to potential local and glacier-wide controlling factors. The findings are further corroborated by complementary observations on ice cliff formation from high-resolution, multi-temporal Unoccupied Aerial Vehicle (UAV) data at five of the studied glaciers (Text S1).

2 Data and Methods

We used 14 Pléiades stereo-images acquired between 2017 and 2021 to derive 2m-resolution multi-spectral images and Digital Elevation Models (DEMs) covering 86 debris-covered glaciers across HMA (Berthier et al., 2014; Shean et al., 2016; Fig. 1; Table S2), 70 of which had more than 65% of their debris-covered area that could be classified after removal of clouds, shadows and fresh-snow (Table S3). The DEMs were used to derive surface slope and aspect, the glacier 'hummockiness', which we defined as the percentage of area for which the Statistical Measure of Relief (SMR) calculated over a 8 m window was greater than 50 m (King et al., 2020), as well as supraglacial channels (Schwanghart & Scherler, 2014; Text S2). The multi-spectral images were used to manually update the glacier and debris outlines of the RGI 6.0 (Pfeffer et al., 2014; Scherler et al., 2018; Table S3). Glacier longitudinal gradient was computed using the 30m resolution AW3D DEM (Dehecq et al., 2019; Tadono et al., 2014) and combined with glacier ice thicknesses (Farinotti et al., 2019) to estimate driving stress over a distance of two ice thicknesses. Distributed glacier velocity, compressive and tensile strain rates were obtained from the global 50m resolution composite by Millan et al. (2022). We additionally used the distributed debris thickness dataset of McCarthy et al. (2022) for all glaciers larger than 2 km^2 (64 glaciers, 47 of which have more than 65% of their debris-covered area that could be classified). All these datasets were aggregated 1) in 500 m distance bins along the glacier flowlines (Kienholz et al., 2014; King et al., 2020) and 2) for each glacier. Data gaps within the bins were filled using a nearest neighbour interpolation.

Ice cliffs and ponds were derived automatically in each Pléiades scene following the Spectral Curvature method for cliffs, which is based solely on spectral characteristics (Kneib et al., 2020), and the Normalized Difference Water Index (NDWI) for ponds (McFeeters, 1996; E. S. Miles et al., 2017; Watson et al., 2016, 2018; Text S2). The ice cliffs are then implicitly defined here as exposed ice in an otherwise debris-covered domain, therefore likely to undergo 'enhanced' melt locally. Some of these features were clearly identifiable as crevasses due to their elongated, straight or slightly curved shapes and these zones were outlined manually. Past studies have only examined high-relief (several meters) ice cliffs, but here our interest is in all exposed ice in the debris-covered area, so we include smaller features common for thin-debris areas, such as crevasses, which similarly enhance surface ablation (Colgan et al., 2016).

Multi-temporal UAV data with a monitoring period longer than 2 years and with at least 3 high-resolution (<1 m) DEMs and orthoimages were available at five of the studied glaciers distributed across HMA. This complementary data was used to identify ice cliff formation events and derive the characteristics of newly formed ice cliffs (Text S1).

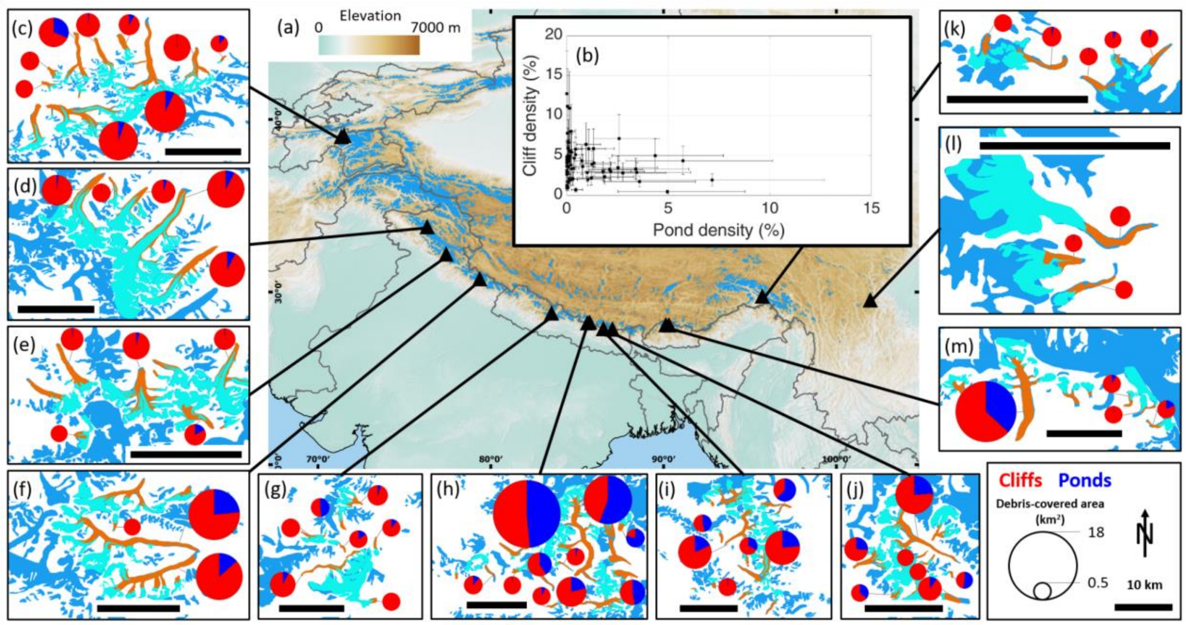

Figure 1: *(a) Map of HMA with each triangle representing one of the 14 Pléiades scenes (some scenes are very close to each other) and the boxes to the side (c-m) showing a zoomed view of the glaciers in these areas. The background is the GTOPO 30 arc seconds (~1 km) DEM, and the glacierised areas are indicated in blue. The inset boxes show the glacier RGI 6.0 outlines in dark blue, the glaciers visible in the Pléiades images in turquoise and their debris-covered areas in brown. The pie charts are scaled to the absolute size of the debris-covered areas and show the relative proportion of ponds (dark blue) and cliffs (red) for each glacier for*

which more than 65% of their debris-covered area could be classified. (b) Cliff and pond density of each of these glaciers. The bars show the uncertainties.

3 Results

3.1. Influence of supraglacial hydrology on ice cliff distribution

Cliffs are preferentially located in the vicinity of ponds and streams, as their density strongly decreases with distance from these hydrological features (Fig. 2a, b), and a large majority of the ponds are related to at least one neighbouring cliff (Fig. 2d). This is further confirmed by field observations (Fig. 2e-g) and multitemporal UAV observations showing that the presence of streams or ponds is responsible for more than 79% of the newly-formed cliff area (Fig. S2). This leads us to define a 40m-buffer around ponds and streams within which we classify the cliff pixels as pond-influenced or stream-influenced (Fig. 2h). With this definition, pond-influenced cliffs account for 19.5% and stream-influenced cliffs for 38.9% of the total cliff area (Fig. 2c). In addition, crevasses represent 19.7% of the cliff area across all glaciers. They are mostly located in the upper extents of the debris-covered areas but also appear lower down glacier, at shear margins, and in the vicinity of proglacial lakes or lateral streams entering the glacier (Fig. S6). The remaining cliffs are qualified as undefined. The stream mapping parameters and choice of buffer size have little influence on this classification (Fig. 2h, S12).

The slope and density of ice cliffs vary between categories, while this is less the case for aspect and size (Fig. S13). Crevasses are usually more densely distributed (15.2% of buffer area), followed by the pond-influenced (6.7%), stream-influenced (4.3%) and undefined cliffs (2.1% of remaining area, Fig. S13a). Despite a variety of glacier aspects (Table S3), there is a clear preferential cliff aspect distribution in the NNW direction for all categories (Fig. S13d), while the newly formed cliffs do not appear to have a preferential aspect (Sato et al., 2021; Fig. S4).

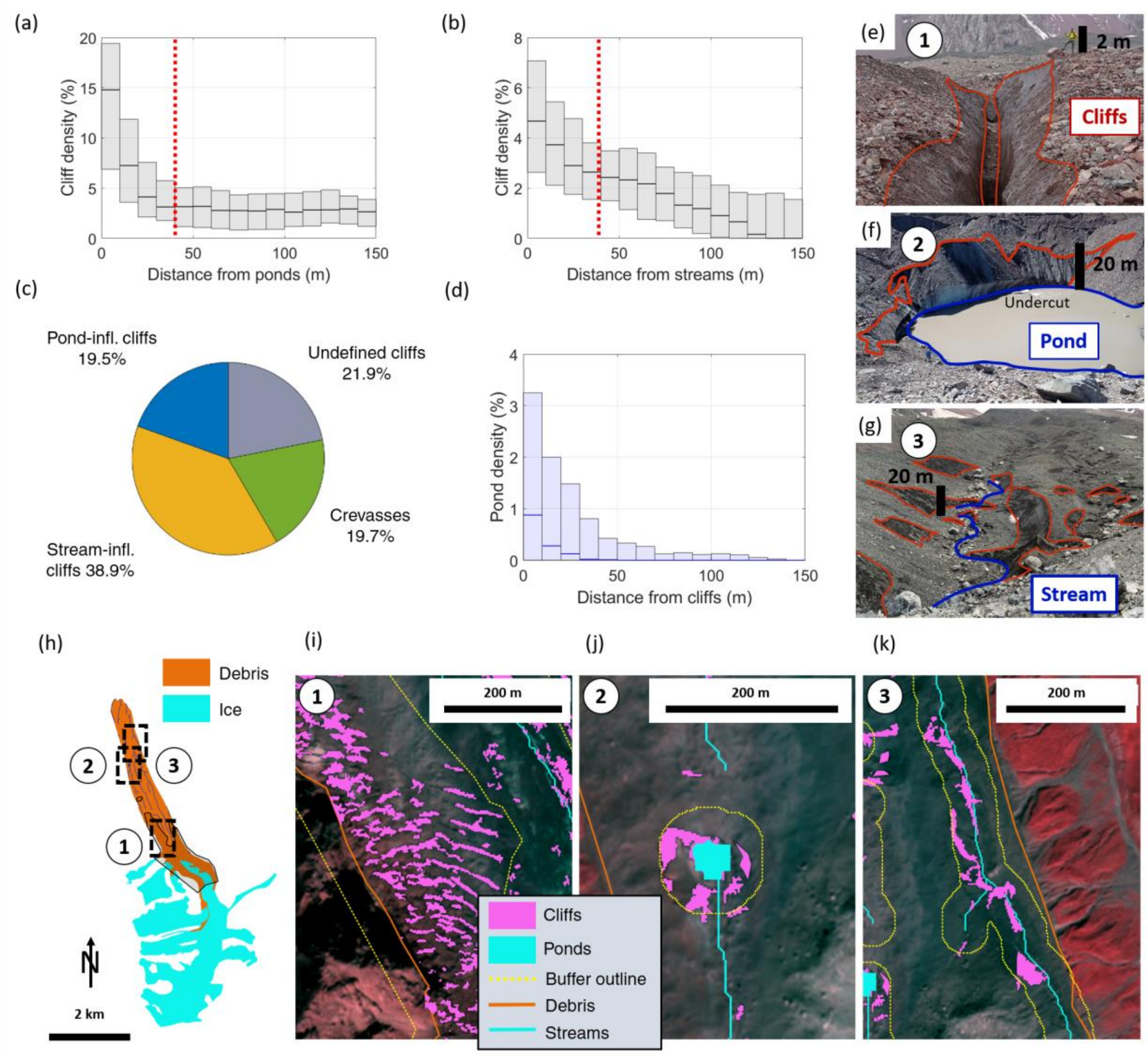

Figure 2: *Cliff density for all glaciers as a function of (a) distance from ponds after removal of the crevasses and (b) distance from streams, after removal of the pond-influenced cliffs. The box plots indicate the median, 25th and 75th percentiles of the cliff density within each 10m bin for each glacier. The red dotted lines show the 40m buffers. (c) Area proportion of undefined, pond- and stream-influenced cliffs and crevasses across all debris-covered glaciers. (d) Pond density for all glaciers as a function of distance from cliffs. (h) Example of classification of ice cliffs from Kyzylsu Glacier, Tajikistan: 1/ crevassed-areas, 2/ pond-influenced cliffs and 3/ stream-influenced cliffs, with the pictures (e-g) and Pléiades view (i-k) of the corresponding zones. Image credit: Marin Kneib and Evan S. Miles. Background of (i-k) is the Pléiades false-colour multispectral image (19/09/2021). Pléiades © CNES 2021, Distribution AIRBUS DS.*

3.2. Controls on ice cliff distribution

The variables associated with ice cliff distribution vary depending on the category of cliff considered (Fig. 3, S15, Table S5). Stream-influenced and undefined cliffs follow a similar distribution for all predictors (Fig. S15), which could indicate that a majority of the undefined cliffs were formerly stream-influenced and backwasted away from the channels. 80% of stream-influenced cliffs are located in areas with debris estimated to be thinner than 33 cm, while 45% of the pond-influenced cliffs are located in areas with thicker debris (Fig. S15). This results in the total cliff density decreasing exponentially ($Y = 5.8e^{-\frac{X}{2}}$, R^2 = 0.73) when debris gets thicker than 10 cm (Fig. 3a, S16). Furthermore, crevasses and pond-influenced cliffs have a clearly contrasting response to the different controls investigated. Indeed, 80% of the crevasses are located in areas with surface velocities higher than the 13 $m.yr^{-1}$ threshold or in areas with debris thinner than 20 cm (Fig. S15). Pond-influenced cliffs clearly depend on pond density, and are thus preferentially located in non-dynamic areas with lower longitudinal gradient and velocity and with thicker debris (Fig. 3, S15, S17).

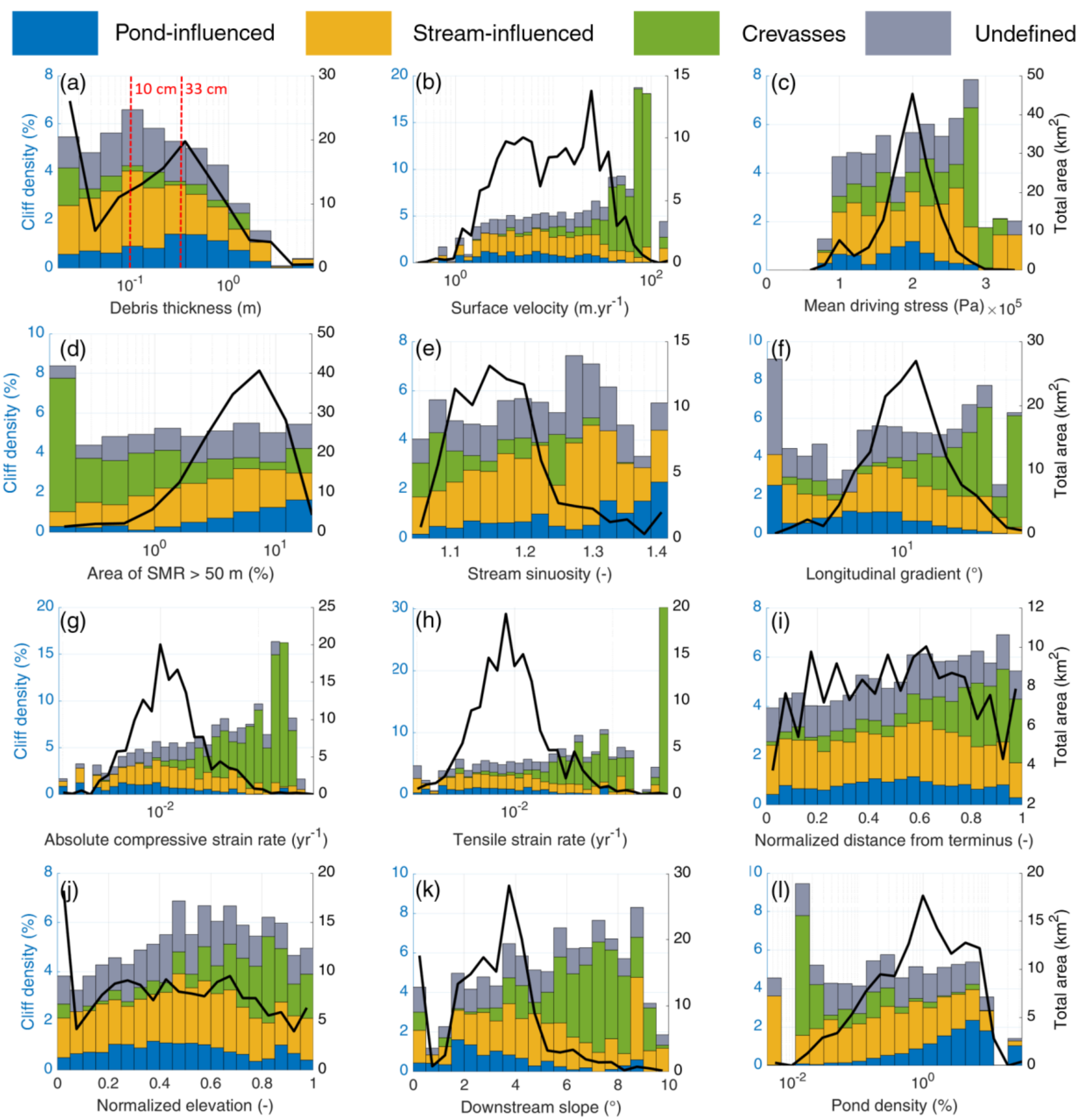

Figure 3: *Mean cliff density split by cliff category for all bins of all glaciers where more than 65% of the debris-covered area could be classified as a function of (a) debris thickness, (b) surface velocity, (c) mean driving stress, (d) 'hummockiness', (e) stream sinuosity, (f) longitudinal gradient, (g) absolute compressive strain rate, (h) tensile strain rate, (i) normalized distance from terminus, (j) normalized elevation above terminus, (k) downstream slope to terminus and (l) pond density. The black line shows the area distribution of all the bins.*

3.2. Ice cliff dependence on glacier state

When aggregating the metrics per glacier, a clear relationship between mean surface velocity across the debris-covered area and cliff density becomes apparent (Fig. 4, S18). The influence of climatic variables seems instead to be limited (Fig. S19). Cliff density decreases with decreasing velocity, up to a point where the trajectory seems to bifurcate. The debris-covered tongues with the highest cliff density and fastest velocity have a larger proportion of crevasses (state 1, Fig. 4). At slower velocities (<10 $m.yr^{-1}$), two trajectories are apparent: 1) glaciers with a large proportion (> ⅓) of pond-influenced cliffs and higher cliff densities (state 3a, Fig 4), and 2) glaciers with a majority of stream-influenced cliffs, which tend to have lower cliff densities (state 3b, Fig. 4). The majority of the glaciers are found at an intermediary stage between these three end-members, with a decreasing proportion of crevasses and an increasing proportion of stream- and pond-influenced cliffs as velocity decreases (state 2, Fig. 4).

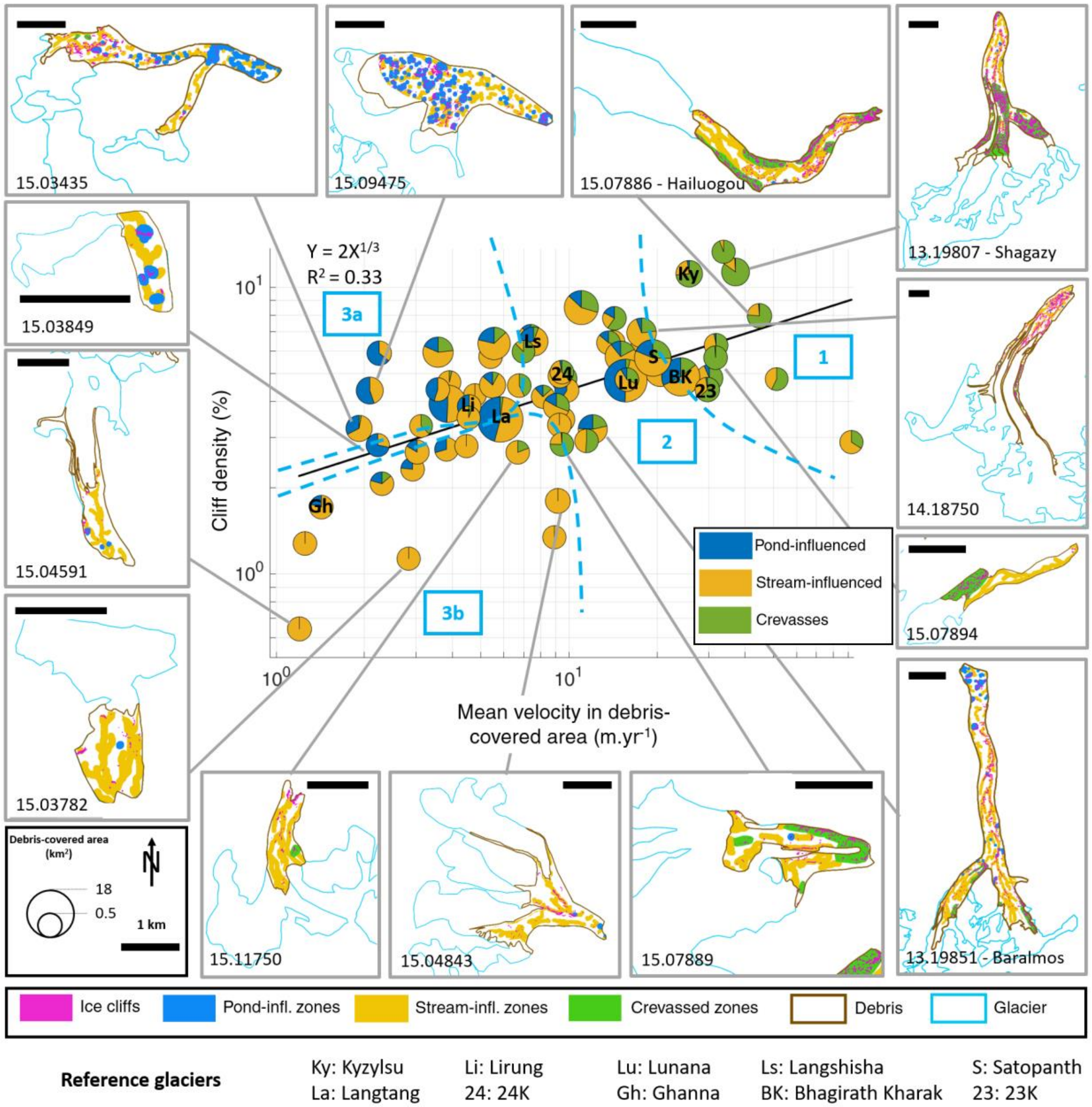

Figure 4: *Glacier-wide cliff density as a function of mean velocity in the debris-covered area for all glaciers where more than 65% of the debris-covered area could be classified. The proportion of undefined cliffs was not represented for readability. The boxes to the side show example maps of some of the glaciers with their surface classifications. Some additional reference glaciers are indicated in the main plot in black. The expression and* R^2 *of the black linear regression are indicated in the upper left corner. In light blue are shown four glacier clusters.*

4 Discussion and conclusions

We have identified the presence of supraglacial streams and ponds, along with the opening of crevasses, to be the main mechanisms responsible for ice cliff formation and development. Newly-formed cliffs tend to be smaller in size and do not have any preferential aspect (Kneib et al., 2021; Fig. S4, S5). Cliffs get reburied when they backwaste away from these supraglacial features (Fig. 2a, b), with the strong control of solar radiation on cliff survival resulting in the preferentially poleward orientation of the total ice cliff population (Buri & Pellicciotti, 2018).

4.1. Ice cliff distribution and glacier state

Velocity stands out as the main control on ice cliff density both at the local and glacier scale (Fig. 3, 4). Interlinkages with other variables means that the cliff density also responds to other local controls, and debris thickness especially, although each category of cliffs responds differently (Fig. 3). The distribution of ice cliffs therefore depends on the glacier dynamics and state. A dynamic debris-covered glacier (mean surface velocity > 10 $m.yr^{-1}$, Fig. 4, 5a, S20a) is usually characterised by thin debris and crevasses which comprise the majority of exposed ice and drain supraglacial streams. Glacier slow-down results in reduced strain rates and the migration of crevasses to the upper sections of the debris-covered area and their eventual disappearance (Fig. 3j, S20b), the extension of stream-influenced cliffs through debris destabilisation and thermo-erosional undercutting (Moore, 2018; Fig. 3a) and possibly the emergence of pond-influenced cliffs. Ponds maintain cliffs in more stagnant zones of thicker debris, also characterised by low longitudinal gradients and driving stress as well as increased hummock prevalence (Benn et al., 2017; Steiner et al., 2019; Watson, Quincey, Carrivick, et al., 2017; Fig. 5c). Such evolution has been observed on other glaciers: on Zmutt Glacier, where it was linked to the development of supraglacial valleys driven by stream incision (Mölg et al., 2020); and on Khumbu Glacier, where high relief zones characterised by growing cliffs and ponds have developed as the glacier has slowed (King et al., 2020; Rowan et al., 2021). Our large dataset enables us to show that this evolution holds across a large number of glaciers, and to identify predictors of cliff type and distribution. The development of large pond-influenced cliffs however requires the accumulation of water in surface depressions, which occurs for larger glaciers with lower longitudinal gradients (Fig. 4, 5c, S17). Most HMA glaciers in this stage of evolution are located in the Central and Eastern Himalaya (Benn et al., 2012, 2017; Racoviteanu et al., 2021; Watson et al., 2016; Watson, Quincey, Carrivick, et al., 2017; Fig. 1). However, some glaciers do not develop such drainage systems due to their relative steepness and small size, resulting in lower ice cliff densities (Fig. 4, 5d, S20d).

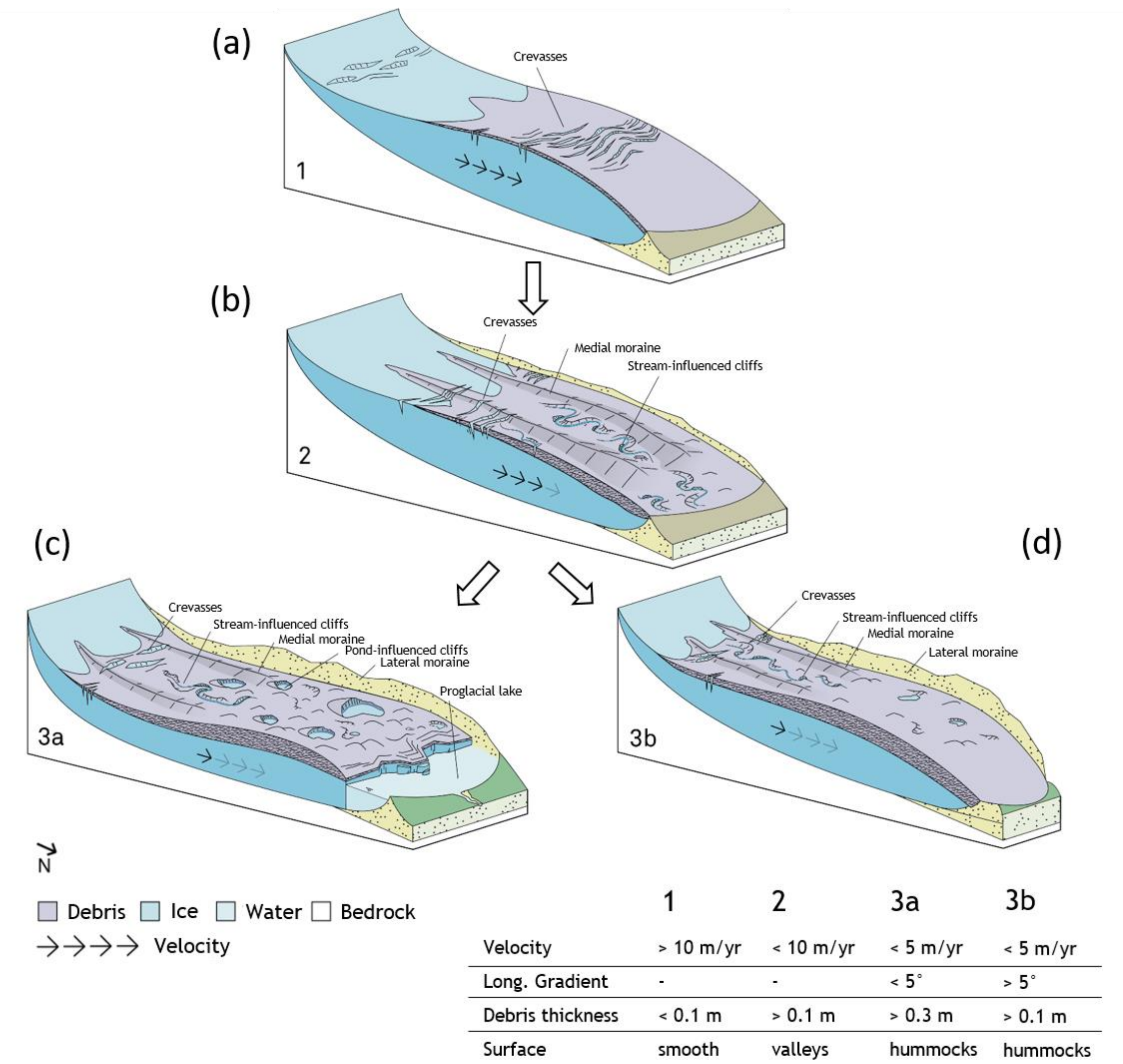

Figure 5: *The four glacier evolution states, with their ice cliff distributions. State 1: fast flowing glacier with thin debris and extensive crevassing. State 2: advanced debris cover, with thicker debris and lower velocities enabling the development of supraglacial valleys and stream-*

influenced cliffs in the non-crevassed areas. State 3a: large stagnating debris-covered tongues, characterised by hummocks, thick debris and ponds maintaining cliffs in these zones. State 3b: stagnating tongues with thick debris, but high enough longitudinal gradient or low enough surface meltwater to prevent the formation of ponds and therefore the survival of cliffs. Figure credit: Martin Heynen.

4.2. Implications for glacier mass balance

We have shown that ice cliff density and characteristics depend on the evolution state of the debris-covered glacier (Fig. 5), which is controlled mainly by dynamics (velocity) and debris thickness. Leveraging this new understanding of how glacier stage affects the presence of cliffs on their surfaces, we have provided the distribution of each type of cliff on glaciers at different stages of evolution (Fig. 3, 4, S20, Table S5). Future efforts should focus on testing the framework developed here by substantially expanding the number of data points with particular attention to include glaciers at distinct stages. Most of the debris-covered glaciers that have been the object of detailed investigations belong to glacier states 2 and 3 and efforts should be made to explore the whole range of evolution when targeting field studies. Already at this stage, however, the relationships detailed in this study outline a framework to estimate ice cliff distribution based on glacier flow characteristics, that are usually available in prognostic flow models, and debris thickness, without having to map the cliffs. Combined with cliff melt enhancement factors (E. S. Miles et al., 2022), this would allow long term estimation of the contribution of ice cliffs to debris-covered glacier mass balance - representing a key modelling advance.

Future work should also target the contribution of crevasses to glacier mass balance. Indeed, these features would likely enhance melt even more than traditional stream- and pond-influenced cliffs due to greater surface roughness at their location increasing turbulent fluxes, and additional reflected shortwave contributions from the opposite crevasse walls (Cathles et al., 2011; Colgan et al., 2016; W. T. Pfeffer & Bretherton, 1987; Purdie et al., 2022). Time-lapse images actually show the upper walls of crevasses backwasting as traditional ice cliffs would (Fig. S21).

Furthermore, their longer-term evolution and influence on shaping the debris-covered glacier surface remains unclear (Kirkbride & Deline, 2013).

Acknowledgments

This project has received funding from the European Research Council (ERC) under the European Union's Horizon 2020 programme (grant agreement 772751) and from the Royal Society via a Newton Advanced Fellowship award (NA170325). The majority of the Pléiades stereo-pairs were provided by Etienne Berthier via the Pléiades Glacier Observatory (PGO) initiative of the French Space Agency (CNES). The remaining images were acquired through the CNES ISIS Programme. We thank the team of the Centre for Research on Glaciers at the Academy of Sciences of Tajikistan who enabled our 2021 fieldwork on Kyzylsu Glacier.

Open Research

The glacier, debris, crevasse, cliff and pond outlines will be made available on Zenodo. Other datasets used include surface velocity from Millan et al. (2022), climate data from ERA5-Land (Muñoz Sabater, 2019), RGI 6.0. glacier outlines (https://nsidc.org/data/nsidc-0770/versions/6), the AW3D 30m DEM (Tadono et al., 2014) and ice thicknesses (Farinotti et al., 2019). Atmospherically-corrected Sentinel-2 images prior to 2019 were obtained from CNES through the PEPS platform (Hagolle et al., 2015). From 2019 and later they were processed directly in Google Earth Engine.

References

Anderson, L. S., Armstrong, W. H., Anderson, R. S., & Buri, P. (2021). Debris cover and the thinning of Kennicott Glacier, Alaska: In situ measurements, automated ice cliff delineation and distributed melt estimates. *Cryosphere*, *15*(1), 265–282. https://doi.org/10.5194/tc-15-265-2021

Anderson, L. S., Armstrong, W. H., Anderson, R. S., Scherler, D., & Petersen, E. (2021). The Causes of Debris-Covered Glacier Thinning: Evidence for the Importance of Ice Dynamics

From Kennicott Glacier, Alaska. *Frontiers in Earth Science, 0*, 723. https://doi.org/10.3389/FEART.2021.680995

Bartlett, O. T., Ng, F. S. L., & Rowan, A. V. (2020). Morphology and evolution of supraglacial hummocks on debris-covered Himalayan glaciers. *Earth Surface Processes and Landforms*, esp.5043. https://doi.org/10.1002/esp.5043

Benn, D. I., Wiseman, S., & Hands, K. A. (2001). Growth and drainage of supraglacial lakes on debrismantled Ngozumpa Glacier, Khumbu Himal, Nepal. *Journal of Glaciology*, *47*(159), 626–638. https://doi.org/10.3189/172756501781831729

Benn, D. I., Bolch, T., Hands, K., Gulley, J., Luckman, A., Nicholson, L. I., et al. (2012, August). Response of debris-covered glaciers in the Mount Everest region to recent warming, and implications for outburst flood hazards. *Earth-Science Reviews*. https://doi.org/10.1016/j.earscirev.2012.03.008

Benn, Douglas I, Thompson, S., Gulley, J., Mertes, J., Luckman, A., & Nicholson, L. (2017). Structure and evolution of the drainage system of a Himalayan debris-covered glacier, and its relationship with patterns of mass loss. *The Cryosphere*, *11*. https://doi.org/10.5194/tc-11-2247-2017

Berthier, E., Vincent, C., Magnússon, E., Gunnlaugsson, Á. Þ., Pitte, P., Le Meur, E., et al. (2014). Glacier topography and elevation changes derived from Pléiades sub-meter stereo images. *The Cryosphere*, *8*, 2275–2291. https://doi.org/10.5194/tc-8-2275-2014

Bolch, T., Buchroithner, M. F., Peters, J., Baessler, M., & Bajracharya, S. (2008). Identification of glacier motion and potentially dangerous glacial lakes in the Mt. Everest region/Nepal using spaceborne imagery. *Natural Hazards and Earth System Sciences*, *8*(6), 1329–1340. https://doi.org/10.5194/nhess-8-1329-2008

Brun, F., Buri, P., Miles, E. S., Wagnon, P., Steiner, J., Berthier, E., et al. (2016). Quantifying volume loss from ice cliffs on debris-covered glaciers using high-resolution terrestrial and aerial photogrammetry. *Journal of Glaciology*. https://doi.org/10.1017/jog.2016.54

Brun, F., Wagnon, P., Berthier, E., Shea, J. M., Immerzeel, W. W., Kraaijenbrink, P. D. A., et al. (2018). Ice cliff contribution to the tongue-wide ablation of Changri Nup Glacier, Nepal, central Himalaya. *The Cryosphere*, *12*(11), 3439–3457. https://doi.org/10.5194/tc-12-3439-2018

Buri, P., & Pellicciotti, F. (2018). Aspect controls the survival of ice cliffs on debris-covered glaciers. *Proceedings of the National Academy of Sciences*, *115*(17), 4369–4374. https://doi.org/10.1073/pnas.1713892115

Buri, P., Pellicciotti, F., Steiner, J. F., Miles, E. S., & Immerzeel, W. W. (2016). A grid-based model of backwasting of supraglacial ice cliffs on debris-covered glaciers. *Annals of Glaciology*, *57*(71), 199–211. https://doi.org/10.3189/2016AoG71A059

Buri, P., Miles, E. S., Steiner, J. F., Ragettli, S., & Pellicciotti, F. (2021). Supraglacial Ice Cliffs Can Substantially Increase the Mass Loss of Debris-Covered Glaciers. *Geophysical Research Letters*, *48*(6). https://doi.org/10.1029/2020GL092150

Cathles, L. M., Abbot, D. S., Bassis, J. N., & MacAyeal, D. R. (2011). Modeling surface-roughness/solar-ablation feedback: application to small-scale surface channels and crevasses of the Greenland ice sheet. *Annals of Glaciology*, *52*(59), 99–108. https://doi.org/10.3189/172756411799096268

Colgan, W., Rajaram, H., Abdalati, W., McCutchan, C., Mottram, R., Moussavi, M. S., & Grigsby, S. (2016, March 1). Glacier crevasses: Observations, models, and mass balance implications. *Reviews of Geophysics*. Blackwell Publishing Ltd.

https://doi.org/10.1002/2015RG000504

Compagno, L., Huss, M., Miles, E. S., McCarthy, M. J., Zekollari, H., Dehecq, A., et al. (2022). Modelling supraglacial debris-cover evolution from the single-glacier to the regional scale: an application to High Mountain Asia. *The Cryosphere*, *16*(5), 1697–1718. https://doi.org/10.5194/tc-16-1697-2022

Dehecq, A., Gourmelen, N., Gardner, A. S., Brun, F., Goldberg, D., Nienow, P. W., et al. (2019). Twenty-first century glacier slowdown driven by mass loss in High Mountain Asia. *Nature Geoscience*, *12*(1), 22–27. https://doi.org/10.1038/s41561-018-0271-9

Egli, P. E., Belotti, B., Ouvry, B., Irving, J., & Lane, S. N. (2021). Subglacial Channels, Climate Warming, and Increasing Frequency of Alpine Glacier Snout Collapse. *Geophysical Research Letters*, *48*(21). https://doi.org/10.1029/2021GL096031

Falaschi, D., Rivera, A., Lo Vecchio Repetto, A., Moragues, S., Villalba, R., Rastner, P., et al. (2021). Evolution of Surface Characteristics of Three Debris-Covered Glaciers in the Patagonian Andes From 1958 to 2020. *Frontiers in Earth Science*, *9*. https://doi.org/10.3389/feart.2021.671854

Farinotti, D., Huss, M., Fürst, J. J., Landmann, J., Machguth, H., Maussion, F., & Pandit, A. (2019). A consensus estimate for the ice thickness distribution of all glaciers on Earth. *Nature Geoscience*, *12*(3), 168–173. https://doi.org/10.1038/s41561-019-0300-3

Ferguson, J. C., & Vieli, A. (2021). Modelling steady states and the transient response of debris-covered glaciers. *The Cryosphere*, *15*(7), 3377–3399. https://doi.org/10.5194/tc-15-3377-2021

Gulley, J. D., Benn, D. I., Screaton, E., & Martin, J. (2009). Mechanisms of englacial conduit formation and their implications for subglacial recharge. *Quaternary Science Reviews*, *28*(19–20), 1984–1999. https://doi.org/10.1016/j.quascirev.2009.04.002

Hagolle, O., Huc, M., Villa Pascual, D., & Dedieu, G. (2015). A Multi-Temporal and Multi-Spectral Method to Estimate Aerosol Optical Thickness over Land, for the Atmospheric Correction of FormoSat-2, LandSat, VENμS and Sentinel-2 Images. *Remote Sensing*, *7*(3), 2668–2691. https://doi.org/10.3390/rs70302668

Herreid, S., & Pellicciotti, F. (2018). Automated detection of ice cliffs within supraglacial debris cover. *The Cryosphere*, *12*, 1811–1829. https://doi.org/10.5194/tc-12-1811-2018

Herreid, S., & Pellicciotti, F. (2020). The state of rock debris covering Earth's glaciers. *Nature Geoscience*, 1–7. https://doi.org/10.1038/s41561-020-0615-0

Immerzeel, W. W., Kraaijenbrink, P. D. A., Shea, J. M., Shrestha, A. B., Pellicciotti, F., Bierkens, M. F. P., & De Jong, S. M. (2014). High-resolution monitoring of Himalayan glacier dynamics using unmanned aerial vehicles. *Remote Sensing of Environment*, *150*, 93–103. https://doi.org/10.1016/j.rse.2014.04.025

Kienholz, C., Rich, J. L., Arendt, A. A., & Hock, R. (2014). A new method for deriving glacier centerlines applied to glaciers in Alaska and northwest Canada. *The Cryosphere*, *8*(2), 503–519. https://doi.org/10.5194/tc-8-503-2014

King, O., Turner, A. G. D., Quincey, D. J., & Carrivick, J. L. (2020). Morphometric evolution of Everest region debris-covered glaciers. *Geomorphology*, *371*, 107422. https://doi.org/10.1016/j.geomorph.2020.107422

Kirkbride, M. P., & Deline, P. (2013). The formation of supraglacial debris covers by primary dispersal from transverse englacial debris bands. *Earth Surface Processes and Landforms*, *38*(15), 1779–1792. https://doi.org/10.1002/esp.3416

Kneib, M., Miles, E. S., Jola, S., Buri, P., Herreid, S., Bhattacharya, A., et al. (2020). Mapping ice cliffs on debris-covered glaciers using multispectral satellite images. *Remote Sensing of Environment*, 112201. https://doi.org/10.1016/j.rse.2020.112201

Kneib, M., Miles, E. S., Buri, P., Molnar, P., McCarthy, M., Fugger, S., & Pellicciotti, F. (2021). Interannual Dynamics of Ice Cliff Populations on Debris-Covered Glaciers From Remote Sensing Observations and Stochastic Modeling. *Journal of Geophysical Research: Earth Surface*, *126*(10). https://doi.org/10.1029/2021JF006179

Kneib, Marin, Miles, E. S., Buri, P., Fugger, S., McCarthy, M., Shaw, T. E., et al. (2022). Sub-seasonal variability of supraglacial ice cliff melt rates and associated processes from time-lapse photogrammetry. *The Cryosphere*, *16*(11), 4701–4725. https://doi.org/10.5194/tc-16-4701-2022

Kraaijenbrink, P. D. A., Shea, J. M., Pellicciotti, F., De Jong, S. M., & Immerzeel, W. W. (2016). Object-based analysis of unmanned aerial vehicle imagery to map and characterise surface features on a debris-covered glacier. *Remote Sensing of Environment*, *186*, 581–595. https://doi.org/10.1016/j.rse.2016.09.013

Loriaux, T., & Ruiz, L. (2021). Spatio-Temporal Distribution of Supra-Glacial Ponds and Ice Cliffs on Verde Glacier, Chile. *Frontiers in Earth Science*, *9*. https://doi.org/10.3389/feart.2021.681071

McCarthy, M., Miles, E., Kneib, M., Buri, P., Fugger, S., & Pellicciotti, F. (2022). Supraglacial debris thickness and supply rate in High-Mountain Asia. *Communications Earth & Environment*, *3*(1), 269. https://doi.org/10.1038/s43247-022-00588-2

McFeeters, S. K. (1996). The use of the Normalized Difference Water Index (NDWI) in the delineation of open water features. *International Journal of Remote Sensing*, *17*(7), 1425–1432. https://doi.org/10.1080/01431169608948714

Miles, E. S., Willis, I. C., Arnold, N. S., Steiner, J., & Pellicciotti, F. (2017). Spatial, seasonal and interannual variability of supraglacial ponds in the Langtang Valley of Nepal, 1999-2013. https://doi.org/10.1017/jog.2016.120

Miles, E. S., Watson, C. S., Brun, F., Berthier, E., Esteves, M., Quincey, D. J., et al. (2018). Glacial and geomorphic effects of a supraglacial lake drainage and outburst event, Everest region, Nepal Himalaya. *The Cryosphere*, *12*, 3891–3905. https://doi.org/10.5194/tc-12-3891-2018

Miles, E. S., Willis, I., Buri, P., Steiner, J. F., Arnold, N. S., & Pellicciotti, F. (2018). Surface Pond Energy Absorption Across Four Himalayan Glaciers Accounts for 1/8 of Total Catchment Ice Loss. *Geophysical Research Letters*, *45*(19), 10,464-10,473. https://doi.org/10.1029/2018GL079678

Miles, E. S., Steiner, J. F., Buri, P., Immerzeel, W. W., & Pellicciotti, F. (2022). Controls on the relative melt rates of debris-covered glacier surfaces. *Environmental Research Letters*, *17*(6), 064004. https://doi.org/10.1088/1748-9326/ac6966

Miles, K. E., Hubbard, B., Irvine-Fynn, T. D. L., Miles, E., Quincey, D. J., & Rowan, A. V. (2020, August 1). Hydrology of debris-covered glaciers in High Mountain Asia. *Earth-Science Reviews*. Elsevier B.V. https://doi.org/10.1016/j.earscirev.2020.103212

Millan, R., Mouginot, J., Rabatel, A., & Morlighem, M. (2022). Ice velocity and thickness of the world's glaciers. *Nature Geoscience*, *15*(2), 124–129. https://doi.org/10.1038/s41561-021-00885-z

Mölg, N., Bolch, T., Walter, A., & Vieli, A. (2019). Unravelling the evolution of Zmuttgletscher and its debris cover since the end of the Little Ice Age. *The Cryosphere*, *13*(7), 1889–1909. https://doi.org/10.5194/tc-13-1889-2019

Mölg, N., Ferguson, J., Bolch, T., & Vieli, A. (2020). On the influence of debris cover on glacier morphology: How high-relief structures evolve from smooth surfaces. *Geomorphology*, *357*, 107092. https://doi.org/10.1016/j.geomorph.2020.107092

Moore, P. L. (2018). Stability of supraglacial debris. *Earth Surface Processes and Landforms*, *43*(1), 285–297. https://doi.org/10.1002/esp.4244

Moore, P. L. (2021). Numerical Simulation of Supraglacial Debris Mobility: Implications for Ablation and Landform Genesis. *Frontiers in Earth Science*, *9*. https://doi.org/10.3389/feart.2021.710131

Muñoz Sabater, J. (2019). ERA5-Land monthly averaged data from 1981 to present. *Copernicus Climate Change Service (C3S) Climate Data Store (CDS)*. https://doi.org/10.24381/cds.68d2bb30

Nicholson, L. I., McCarthy, M., Pritchard, H. D., & Willis, I. (2018). Supraglacial debris thickness variability: Impact on ablation and relation to terrain properties. *Cryosphere*, *12*(12), 3719–3734. https://doi.org/10.5194/tc-12-3719-2018

Pellicciotti, F., Stephan, C., Miles, E. S., Herreid, S., Immerzeel, W. W., & Bolch, T. (2015). Mass-balance changes of the debris-covered glaciers in the Langtang Himal, Nepal, from 1974 to 1999. *Journal of Glaciology*, *61*(226), 373–386. https://doi.org/10.3189/2015JoG13J237

Pfeffer, W. T., & Bretherton, C. S. (1987). The effect of crevasses on the solar heating of a glacier surface. *The Physical Basis of Ice Sheet Modelling*, *170*, 191–205.

Pfeffer, W. Tad, Arendt, A. A., Bliss, A., Bolch, T., Cogley, J. G., Gardner, A. S., et al. (2014). The randolph glacier inventory: A globally complete inventory of glaciers. *Journal of Glaciology*, *60*(221), 537–552. https://doi.org/10.3189/2014JoG13J176

Purdie, H., Zawar-Reza, P., Katurji, M., Schumacher, B., Kerr, T., & Bealing, P. (2022). Variability in the vertical temperature profile within crevasses at an alpine glacier. *Journal of Glaciology*, 1–15. https://doi.org/10.1017/jog.2022.73

Quincey, D. J., & Glasser, N. F. (2009). Morphological and ice-dynamical changes on the Tasman Glacier, New Zealand, 1990-2007. *Global and Planetary Change*, *68*(3), 185–197. https://doi.org/10.1016/j.gloplacha.2009.05.003

Quincey, D. J., Richardson, S. D., Luckman, A., Lucas, R. M., Reynolds, J. M., Hambrey, M. J., & Glasser, N. F. (2007). Early recognition of glacial lake hazards in the Himalaya using remote sensing datasets. *Global and Planetary Change*, *56*(1–2), 137–152. https://doi.org/10.1016/j.gloplacha.2006.07.013

Racoviteanu, A. E., Nicholson, L., & Glasser, N. F. (2021). Surface composition of debris-covered glaciers across the Himalaya using linear spectral unmixing of Landsat 8 OLI imagery. *The Cryosphere*, *15*, 4557–4588. https://doi.org/10.5194/tc-15-4557-2021

Racoviteanu, A. E., Glasser, N. F., Robson, B. A., Harrison, S., Millan, R., Kayastha, R. B., & Kayastha, R. (2022). Recent Evolution of Glaciers in the Manaslu Region of Nepal From Satellite Imagery and UAV Data (1970–2019). *Frontiers in Earth Science*, *9*. https://doi.org/10.3389/feart.2021.767317

Reid, T. D., & Brock, B. W. (2014). Assessing ice-cliff backwasting and its contribution to total ablation of debris-covered Miage glacier, Mont Blanc massif, Italy. *Journal of Glaciology*. https://doi.org/10.3189/2014JoG13J045

Reynolds, J. (2000). On the formation of supraglacial lakes on debris-covered glaciers. *IAHS-AISH Publication*, *264*, 153–161.

Röhl, K. (2006). Thermo-erosional notch development at fresh-water-calving Tasman Glacier, New Zealand. *Journal of Glaciology*, *52*(177), 203–213. https://doi.org/10.3189/172756506781828773

Röhl, K. (2008). Characteristics and evolution of supraglacial ponds on debris-covered Tasman Glacier, New Zealand. *Journal of Glaciology*. https://doi.org/10.3189/002214308787779861

Rounce, D. R., Hock, R., McNabb, R. W., Millan, R., Sommer, C., Braun, M. H., et al. (2021). Distributed global debris thickness estimates reveal debris significantly impacts glacier mass balance. *Geophysical Research Letters*, e2020GL091311. https://doi.org/10.1029/2020GL091311

Rowan, A. V., Egholm, D. L., Quincey, D. J., Hubbard, B., King, O., Miles, E. S., et al. (2021). The Role of Differential Ablation and Dynamic Detachment in Driving Accelerating Mass Loss From a Debris-Covered Himalayan Glacier. *Journal of Geophysical Research: Earth Surface*, *126*(9), e2020JF005761. https://doi.org/10.1029/2020JF005761

Sakai, A., & Fujita, K. (2010). Formation conditions of supraglacial lakes on debriscovered glaciers in the Himalaya. *Journal of Glaciology*, *56*(195), 177–181. https://doi.org/10.3189/002214310791190785

Sakai, A., & Takeuchi, N. (2000). *Debris-Covered Glaciers*. IAHS Publ.

Sakai, A., Nakawo, M., & Fujita, K. (1998). Melt rate of ice cliffs on the Lirung Glacier, Nepal Himalayas, 1996. *Bulletin of Glacier Research*, *16*, 57–66.

Sakai, A., Nakawo, M., & Fujita, K. (2002). Distribution Characteristics and Energy Balance of Ice Cliffs on Debris-covered Glaciers, Nepal Himalaya. *Arctic, Antarctic, and Alpine Research*, *34*(1), 12–19. https://doi.org/10.1080/15230430.2002.12003463

Salerno, F., Thakuri, S., D'Agata, C., Smiraglia, C., Manfredi, E. C., Viviano, G., & Tartari, G.

(2012). Glacial lake distribution in the Mount Everest region: Uncertainty of measurement and conditions of formation. *Global and Planetary Change*, *92–93*, 30–39. https://doi.org/10.1016/j.gloplacha.2012.04.001

Sato, Y., Fujita, K., Inoue, H., Sunako, S., Sakai, A., Tsushima, A., et al. (2021). Ice Cliff Dynamics of Debris-Covered Trakarding Glacier in the Rolwaling Region, Nepal Himalaya. *Frontiers in Earth Science*, *9*, 398. https://doi.org/10.3389/FEART.2021.623623/BIBTEX

Scherler, D., Wulf, H., & Gorelick, N. (2018). Global Assessment of Supraglacial Debris-Cover Extents. *Geophysical Research Letters*. https://doi.org/10.1029/2018GL080158

Schwanghart, W., & Scherler, D. (2014). Short Communication: TopoToolbox 2 – MATLAB-based software for topographic analysis and modeling in Earth surface sciences. *Earth Surface Dynamics*, *2*(1), 1–7. https://doi.org/10.5194/esurf-2-1-2014

Sharp, R. P. (1949). Studies of superglacial debris on valley glaciers. *American Journal of Science*, *247*(5), 289–315. https://doi.org/10.2475/ajs.247.5.289

Shean, D. E., Alexandrov, O., Moratto, Z. M., Smith, B. E., Joughin, I. R., Porter, C., & Morin, P. (2016). An automated, open-source pipeline for mass production of digital elevation models (DEMs) from very-high-resolution commercial stereo satellite imagery. *ISPRS Journal of Photogrammetry and Remote Sensing*, *116*, 101–117. https://doi.org/10.1016/j.isprsjprs.2016.03.012

Steiner, J. F., Buri, P., Miles, E. S., Ragettli, S., & Pellicciotti, F. (2019). Supraglacial ice cliffs and ponds on debris-covered glaciers: Spatio-temporal distribution and characteristics. *Journal of Glaciology*, *65*(252), 617–632. https://doi.org/10.1017/jog.2019.40

Stokes, C. R., Popovnin, V., Aleynikov, A., Gurney, S. D., & Shahgedanova, M. (2007). Recent glacier retreat in the Caucasus Mountains, Russia, and associated increase in supraglacial debris cover and supra-/proglacial lake development. In *Annals of Glaciology* (Vol. 46, pp. 195–203). https://doi.org/10.3189/172756407782871468

Tadono, T., Ishida, H., Oda, F., Naito, S., Minakawa, K., & Iwamoto, H. (2014). Precise Global DEM Generation by ALOS PRISM. *ISPRS Annals of the Photogrammetry, Remote Sensing and Spatial Information Sciences*, *II–4*, 71–76. https://doi.org/10.5194/isprsannals-II-4-71-2014

Watson, C. S., Quincey, D. J., Carrivick, J. L., & Smith, M. W. (2016). The dynamics of supraglacial ponds in the Everest region, central Himalaya. *Global and Planetary Change*, *142*, 14–27. https://doi.org/https://doi.org/10.1016/j.gloplacha.2016.04.008

Watson, C. S., Quincey, D. J., Carrivick, J. L., & Smith, M. W. (2017). Ice cliff dynamics in the Everest region of the Central Himalaya. *Geomorphology*, *278*, 238–251. https://doi.org/10.1016/j.geomorph.2016.11.017

Watson, C. S., Quincey, D. J., Smith, M. W., Carrivick, J. L., Rowan, A. V, & James, M. R. (2017). Quantifying ice cliff evolution with multi-temporal point clouds on the debris-covered Khumbu Glacier, Nepal. https://doi.org/10.1017/jog.2017.47

Watson, C. S., King, O., Miles, E. S., & Quincey, D. J. (2018). Optimising NDWI supraglacial pond classification on Himalayan debris-covered glaciers. *Remote Sensing of Environment*, *217*, 414–425. https://doi.org/10.1016/j.rse.2018.08.020

Additional references in supporting information

Fugger, S., Fyffe, C.L., Fatichi, S., Miles, E., McCarthy, M., Shaw, T.E., Ding, B., Yang, W., Wagnon, P., Immerzeel, W., Liu, Q., Pellicciotti, F., 2022. Understanding monsoon controls on the energy and mass balance of glaciers in the Central and Eastern Himalaya. Cryosph. 16, 1631–1652. https://doi.org/10.5194/tc-16-1631-2022

Controls on Ice Cliff Formation, Distribution and Characteristics on Debris-Covered Glaciers

M. Kneib[1, 2], Catriona Fyffe[3], Evan S. Miles[1], Shayna Lindemann[1], Thomas E. Shaw[1], Pascal Buri[1], Michael McCarthy[1], Boris Ouvry[4], Andreas Vieli[4], Yota Sato[5], Philip D.A Kraaijenbrink[6], Chuanxi Zhao[7,8], Peter Molnar[2], Francesca Pellicciotti[1,3]

[1] High Mountain Glaciers and Hydrology Group, Swiss Federal Institute, WSL, Birmensdorf, Switzerland.

[2] Institute of Environmental Engineering, ETH Zürich, Zürich, Switzerland

[3] Department of Geography and Environmental Sciences, Northumbria University, Newcastle upon Tyne, UK

[4] Department of Geography, University of Zurich, 8057 Zurich, Switzerland

[5] Graduate School of Environmental Studies, Nagoya University, Nagoya, Japan

[6] Utrecht University, Department of Physical Geography, PO Box 80115, 3508 TC, Utrecht, The Netherlands.

[7] College of Earth and Environmental Sciences, Lanzhou University, Lanzhou 730000, China

[8] State Key Laboratory of Tibetan Plateau Earth System, Environment and Resources (TPESER), Institute of Tibetan Plateau Research, Chinese Academy of Sciences

Corresponding author: Marin Kneib (marin.kneib@gmail.com)

Key Points:

- We derived an unprecedented dataset of 37537 ice cliffs and their characteristics across 86 debris-covered glaciers in High Mountain Asia
- We find that 38.9% of the cliffs are stream-influenced, 19.5% pond-influenced and 19.7% are crevasses
- Ice cliff distribution can be predicted by velocity as an indicator of both the dynamics and state of evolution of debris-covered glaciers

Abstract

Ice cliff distribution plays a major role in determining the melt of debris-covered glaciers but its controls are largely unknown. We assembled a dataset of 37537 ice cliffs and determined their characteristics across 86 debris-covered glaciers within High Mountain Asia (HMA). We complemented this dataset with the analysis of 202 cliff formation events from multi-temporal UAV observations for a subset of glaciers. We find that 38.9% of the cliffs are stream-influenced, 19.5% pond-influenced and 19.7% are crevasses. Surface velocity is the main predictor of cliff distribution at both local and glacier scale, indicating its dependence on the dynamic state and hence evolution stage of debris-covered glacier tongues. Supraglacial ponds contribute to maintaining cliffs in areas of thicker debris, but this is only possible if water accumulates at the surface. Overall, total cliff density decreases exponentially with debris thickness as soon as debris gets thicker than 10 cm.

Plain Language Summary

Debris-covered glaciers are common throughout the world's mountain ranges and are characterised by the presence of steep ice cliffs among the debris-covered ice. It is well-known that the cliffs are responsible for a large portion of the melt of these glaciers but the way they form, and as a result the controls on their development and distribution across glaciers remains poorly understood. Novel mapping approaches combined with high-resolution satellite and drone products enabled us to disentangle some of these controls and to show that the ice cliffs are generally formed and maintained by the surface hydrology (ponds or streams) or by the opening of crevasses. As a result, they depend both at the local and glacier scale on the dynamic state of

the glaciers as well as the evolution stage of their debris cover. This provides a pathway to better represent their contribution to glacier melt in predictive glacier models.

1 Introduction

Debris-covered glaciers are found in all mountain ranges (Scherler et al., 2018), and supraglacial debris extents and thickness are expected to increase in a warming climate (Compagno et al., 2022; Herreid & Pellicciotti, 2020; Stokes et al., 2007). However, despite considerable recent advances, modelling the mass balances of these glaciers remains challenging (Rounce et al., 2021). This is partly due to the presence of supraglacial ice cliffs, which melt up to 20 times faster than the surrounding debris-covered ice, therefore compensating for the relatively well constrained debris insulating effect (Anderson, Armstrong, Anderson, & Buri, 2021; Brun et al., 2018; E. S. Miles, Willis, et al., 2018; Reid & Brock, 2014; Sakai et al., 1998, 2002). In one catchment in High Mountain Asia (HMA) ice cliffs were shown to contribute 17+/-4% of the melt of the debris-covered ice (Buri et al., 2021). This has major implications for the mass balance of debris-covered glaciers (Pellicciotti et al., 2015) and their long-term evolution (Ferguson & Vieli, 2021; Racoviteanu et al., 2022).

While models accurately simulate the energy and mass balance contribution of individual ice cliffs (Buri et al., 2016; Kneib et al., 2022), their application at large spatial scales is limited by our understanding of the controls of ice cliff distribution. Indeed, estimates of ice cliff density are difficult to make (Anderson, Armstrong, Anderson, & Buri, 2021; Herreid & Pellicciotti, 2018; Kneib et al., 2020) and vary widely in time and space, between 1 and 15% of the debris-covered area (e.g. Falaschi et al., 2021; Kneib et al., 2021; Loriaux & Ruiz, 2021; Sato et al., 2021; Steiner et al., 2019; Watson et al., 2017). Remote sensing studies have shown that cliffs are often associated with ponds (Steiner et al., 2019; Watson, Quincey, Carrivick, et al., 2017), hinting at a preferential location of ice cliffs where lower glacier longitudinal gradient and surface velocities promote surface ponding (Bolch et al., 2008; Quincey et al., 2007; Quincey & Glasser, 2009; Racoviteanu et al., 2021; Reynolds, 2000; Sakai & Fujita, 2010; Salerno et al., 2012). Other limited observations indicate that ice cliffs preferentially develop at the confluence of glacial tributaries, in locations of high compressive strain rates, and areas of thinner debris (Anderson, Armstrong, Anderson, & Buri, 2021; Anderson, Armstrong, Anderson, Scherler, et al., 2021; Benn et al., 2012; Kraaijenbrink et al., 2016; Steiner et al., 2019; Watson, Quincey, Carrivick, et al., 2017). However, the lack of consistent observations of cliff distribution makes it difficult to include ice cliffs in predictive glacier models in a way that accounts for their spatial distribution and temporal evolution.

Ice cliff survival is inherently linked to debris stability, which is a function of local slope, debris thickness and water content, as well as undercutting by streams or ponds (Moore, 2018). The local slope can change in relatively short time scales with differential melt caused by heterogeneous debris thicknesses (Moore, 2021; Nicholson et al., 2018; Sharp, 1949), which results in the surface of debris-covered glaciers being particularly hummocky where the debris gets thicker than 20-30 cm (Bartlett et al., 2020; King et al., 2020). Slope undercutting and destabilisation by streams or ponds is expected to be one of the main triggers for ice cliff formation (Mölg et al., 2019; Röhl, 2006, 2008; Sakai & Takeuchi, 2000) and survival (Benn et al., 2001, 2012; Brun et al., 2016; Kneib et al., 2022; Sato et al., 2021; Watson, Quincey, Smith, et al., 2017). Other hypothesised cliff formation mechanisms include crevasse opening (Reid & Brock, 2014; Steiner et al., 2019) or the collapse of englacial conduits (Egli et al., 2021; Gulley et al., 2009; Immerzeel et al., 2014; E. S. Miles, Watson, et al., 2018; K. E. Miles et al., 2020; Sakai & Takeuchi, 2000), but these hypotheses have never been tested in a quantitative way.

In this study, we therefore 1) map ice cliffs across 86 glaciers in HMA, 2) determine their physical characteristics, 3) attribute their distribution to potential local and glacier-wide controlling factors. The findings are further corroborated by complementary observations on ice cliff formation from high-resolution, multi-temporal Unoccupied Aerial Vehicle (UAV) data at five of the studied glaciers (Text S1).

2 Data and Methods

We used 14 Pléiades stereo-images acquired between 2017 and 2021 to derive 2m-resolution multi-spectral images and Digital Elevation Models (DEMs) covering 86 debris-covered glaciers across HMA (Berthier et al., 2014; Shean et al., 2016; Fig. 1; Table S2), 70 of which had more than 65% of their debris-covered area that could be classified after removal of clouds, shadows and fresh-snow (Table S3). The DEMs were used to derive surface slope and aspect, the glacier 'hummockiness', which we defined as the percentage of area for which the Statistical Measure of Relief (SMR) calculated over a 8 m window was greater than 50 m (King et al., 2020), as well as supraglacial channels (Schwanghart & Scherler, 2014; Text S2). The multi-spectral images were used to manually update the glacier and debris outlines of the RGI 6.0 (Pfeffer et al., 2014; Scherler et al., 2018; Table S3). Glacier longitudinal gradient was computed using the 30m resolution AW3D DEM (Dehecq et al., 2019; Tadono et al., 2014) and combined with glacier ice thicknesses (Farinotti et al., 2019) to estimate driving stress over a distance of two ice thicknesses. Distributed glacier velocity, compressive and tensile strain rates were obtained from the global 50m resolution composite by Millan et al. (2022). We additionally used the distributed debris thickness dataset of McCarthy et al. (2022) for all glaciers larger than 2 km^2 (64 glaciers, 47 of which have more than 65% of their debris-covered area that could be classified). All these datasets were aggregated 1) in 500 m distance bins along the glacier flowlines (Kienholz et al., 2014; King et al., 2020) and 2) for each glacier. Data gaps within the bins were filled using a nearest neighbour interpolation.

Ice cliffs and ponds were derived automatically in each Pléiades scene following the Spectral Curvature method for cliffs, which is based solely on spectral characteristics (Kneib et al., 2020), and the Normalized Difference Water Index (NDWI) for ponds (McFeeters, 1996; E. S. Miles et al., 2017; Watson et al., 2016, 2018; Text S2). The ice cliffs are then implicitly defined here as exposed ice in an otherwise debris-covered domain, therefore likely to undergo 'enhanced' melt locally. Some of these features were clearly identifiable as crevasses due to their elongated, straight or slightly curved shapes and these zones were outlined manually. Past studies have only examined high-relief (several meters) ice cliffs, but here our interest is in all exposed ice in the debris-covered area, so we include smaller features common for thin-debris areas, such as crevasses, which similarly enhance surface ablation (Colgan et al., 2016).

Multi-temporal UAV data with a monitoring period longer than 2 years and with at least 3 high-resolution (<1 m) DEMs and orthoimages were available at five of the studied glaciers distributed across HMA. This complementary data was used to identify ice cliff formation events and derive the characteristics of newly formed ice cliffs (Text S1).

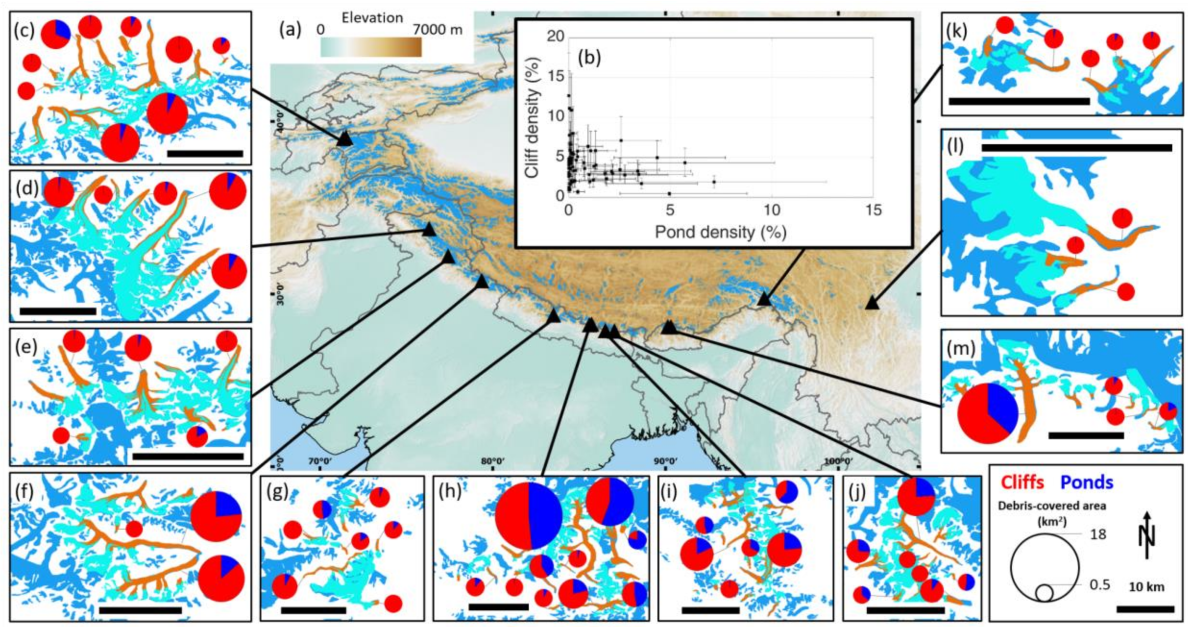

Figure 1: *(a) Map of HMA with each triangle representing one of the 14 Pléiades scenes (some scenes are very close to each other) and the boxes to the side (c-m) showing a zoomed view of the glaciers in these areas. The background is the GTOPO 30 arc seconds (~1 km) DEM, and the glacierised areas are indicated in blue. The inset boxes show the glacier RGI 6.0 outlines in dark blue, the glaciers visible in the Pléiades images in turquoise and their debris-covered areas in brown. The pie charts are scaled to the absolute size of the debris-covered areas and show the relative proportion of ponds (dark blue) and cliffs (red) for each glacier for*

which more than 65% of their debris-covered area could be classified. (b) Cliff and pond density of each of these glaciers. The bars show the uncertainties.

3 Results

3.1. Influence of supraglacial hydrology on ice cliff distribution

Cliffs are preferentially located in the vicinity of ponds and streams, as their density strongly decreases with distance from these hydrological features (Fig. 2a, b), and a large majority of the ponds are related to at least one neighbouring cliff (Fig. 2d). This is further confirmed by field observations (Fig. 2e-g) and multitemporal UAV observations showing that the presence of streams or ponds is responsible for more than 79% of the newly-formed cliff area (Fig. S2). This leads us to define a 40m-buffer around ponds and streams within which we classify the cliff pixels as pond-influenced or stream-influenced (Fig. 2h). With this definition, pond-influenced cliffs account for 19.5% and stream-influenced cliffs for 38.9% of the total cliff area (Fig. 2c). In addition, crevasses represent 19.7% of the cliff area across all glaciers. They are mostly located in the upper extents of the debris-covered areas but also appear lower down glacier, at shear margins, and in the vicinity of proglacial lakes or lateral streams entering the glacier (Fig. S6). The remaining cliffs are qualified as undefined. The stream mapping parameters and choice of buffer size have little influence on this classification (Fig. 2h, S12).

The slope and density of ice cliffs vary between categories, while this is less the case for aspect and size (Fig. S13). Crevasses are usually more densely distributed (15.2% of buffer area), followed by the pond-influenced (6.7%), stream-influenced (4.3%) and undefined cliffs (2.1% of remaining area, Fig. S13a). Despite a variety of glacier aspects (Table S3), there is a clear preferential cliff aspect distribution in the NNW direction for all categories (Fig. S13d), while the newly formed cliffs do not appear to have a preferential aspect (Sato et al., 2021; Fig. S4).

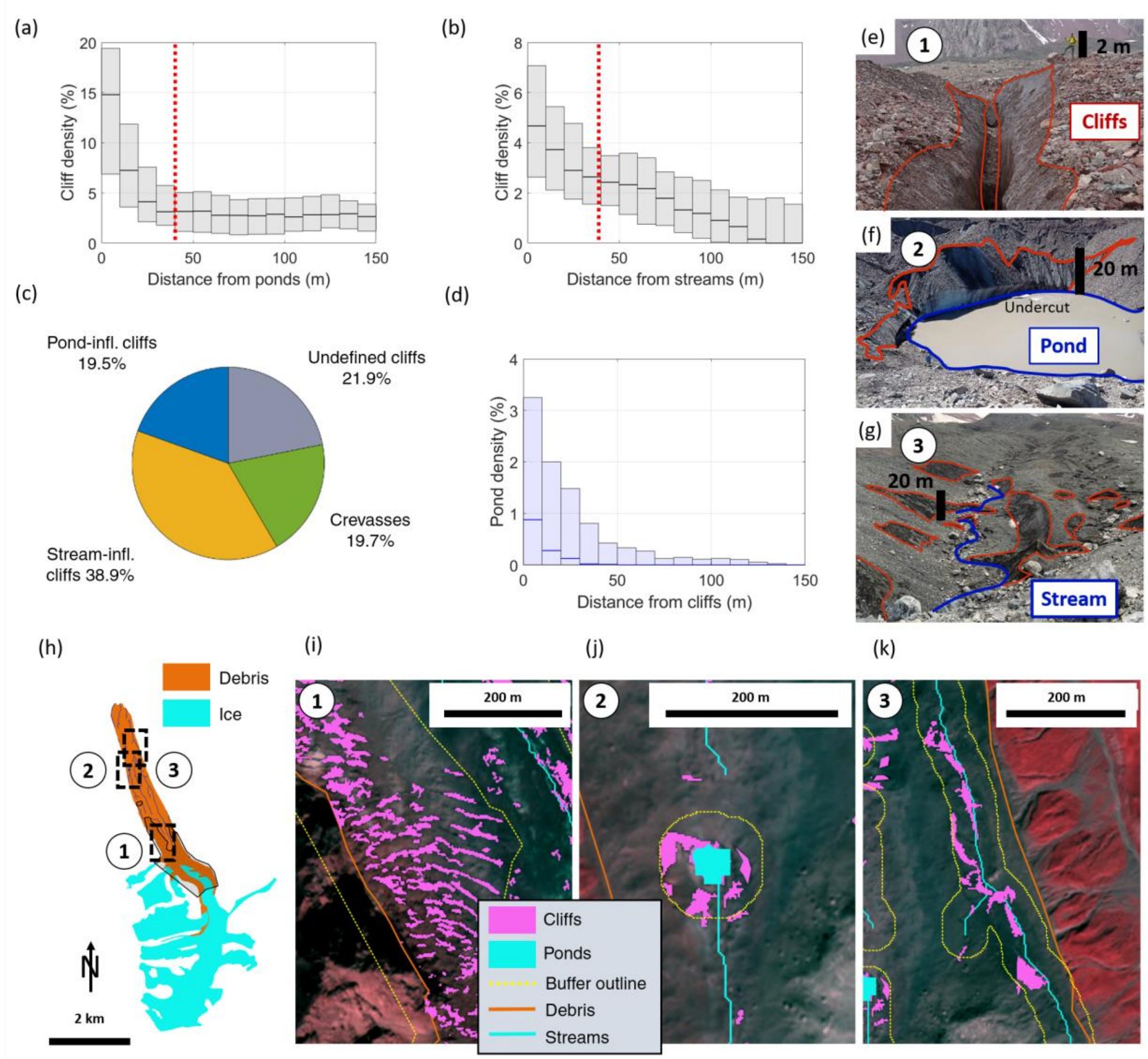

Figure 2: *Cliff density for all glaciers as a function of (a) distance from ponds after removal of the crevasses and (b) distance from streams, after removal of the pond-influenced cliffs. The box plots indicate the median, 25th and 75th percentiles of the cliff density within each 10m bin for each glacier. The red dotted lines show the 40m buffers. (c) Area proportion of undefined, pond- and stream-influenced cliffs and crevasses across all debris-covered glaciers. (d) Pond density for all glaciers as a function of distance from cliffs. (h) Example of classification of ice cliffs from Kyzylsu Glacier, Tajikistan: 1/ crevassed-areas, 2/ pond-influenced cliffs and 3/ stream-influenced cliffs, with the pictures (e-g) and Pléiades view (i-k) of the corresponding zones. Image credit: Marin Kneib and Evan S. Miles. Background of (i-k) is the Pléiades false-colour multispectral image (19/09/2021). Pléiades © CNES 2021, Distribution AIRBUS DS.*

3.2. Controls on ice cliff distribution

The variables associated with ice cliff distribution vary depending on the category of cliff considered (Fig. 3, S15, Table S5). Stream-influenced and undefined cliffs follow a similar distribution for all predictors (Fig. S15), which could indicate that a majority of the undefined cliffs were formerly stream-influenced and backwasted away from the channels. 80% of stream-influenced cliffs are located in areas with debris estimated to be thinner than 33 cm, while 45% of the pond-influenced cliffs are located in areas with thicker debris (Fig. S15). This results in the total cliff density decreasing exponentially ($Y = 5.8e^{-\frac{X}{2}}$, $R^2 = 0.73$) when debris gets thicker than 10 cm (Fig. 3a, S16). Furthermore, crevasses and pond-influenced cliffs have a clearly contrasting response to the different controls investigated. Indeed, 80% of the crevasses are located in areas with surface velocities higher than the 13 $m.yr^{-1}$ threshold or in areas with debris thinner than 20 cm (Fig. S15). Pond-influenced cliffs clearly depend on pond density, and are thus preferentially located in non-dynamic areas with lower longitudinal gradient and velocity and with thicker debris (Fig. 3, S15, S17).

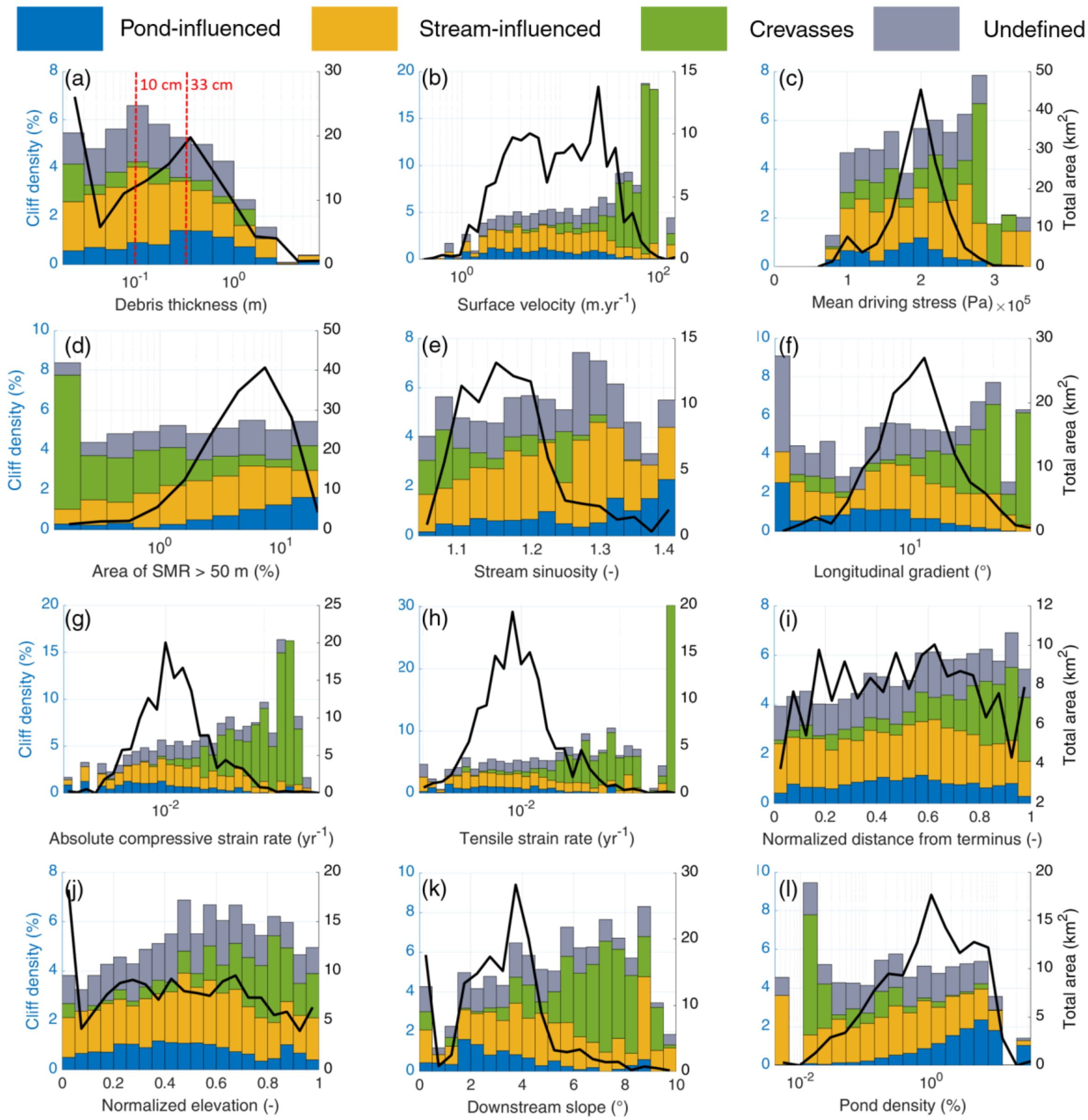

Figure 3: *Mean cliff density split by cliff category for all bins of all glaciers where more than 65% of the debris-covered area could be classified as a function of (a) debris thickness, (b) surface velocity, (c) mean driving stress, (d) 'hummockiness', (e) stream sinuosity, (f) longitudinal gradient, (g) absolute compressive strain rate, (h) tensile strain rate, (i) normalized distance from terminus, (j) normalized elevation above terminus, (k) downstream slope to terminus and (l) pond density. The black line shows the area distribution of all the bins.*

3.2. Ice cliff dependence on glacier state

When aggregating the metrics per glacier, a clear relationship between mean surface velocity across the debris-covered area and cliff density becomes apparent (Fig. 4, S18). The influence of climatic variables seems instead to be limited (Fig. S19). Cliff density decreases with decreasing velocity, up to a point where the trajectory seems to bifurcate. The debris-covered tongues with the highest cliff density and fastest velocity have a larger proportion of crevasses (state 1, Fig. 4). At slower velocities (<10 $m.yr^{-1}$), two trajectories are apparent: 1) glaciers with a large proportion (> ⅓) of pond-influenced cliffs and higher cliff densities (state 3a, Fig 4), and 2) glaciers with a majority of stream-influenced cliffs, which tend to have lower cliff densities (state 3b, Fig. 4). The majority of the glaciers are found at an intermediary stage between these three end-members, with a decreasing proportion of crevasses and an increasing proportion of stream- and pond-influenced cliffs as velocity decreases (state 2, Fig. 4).

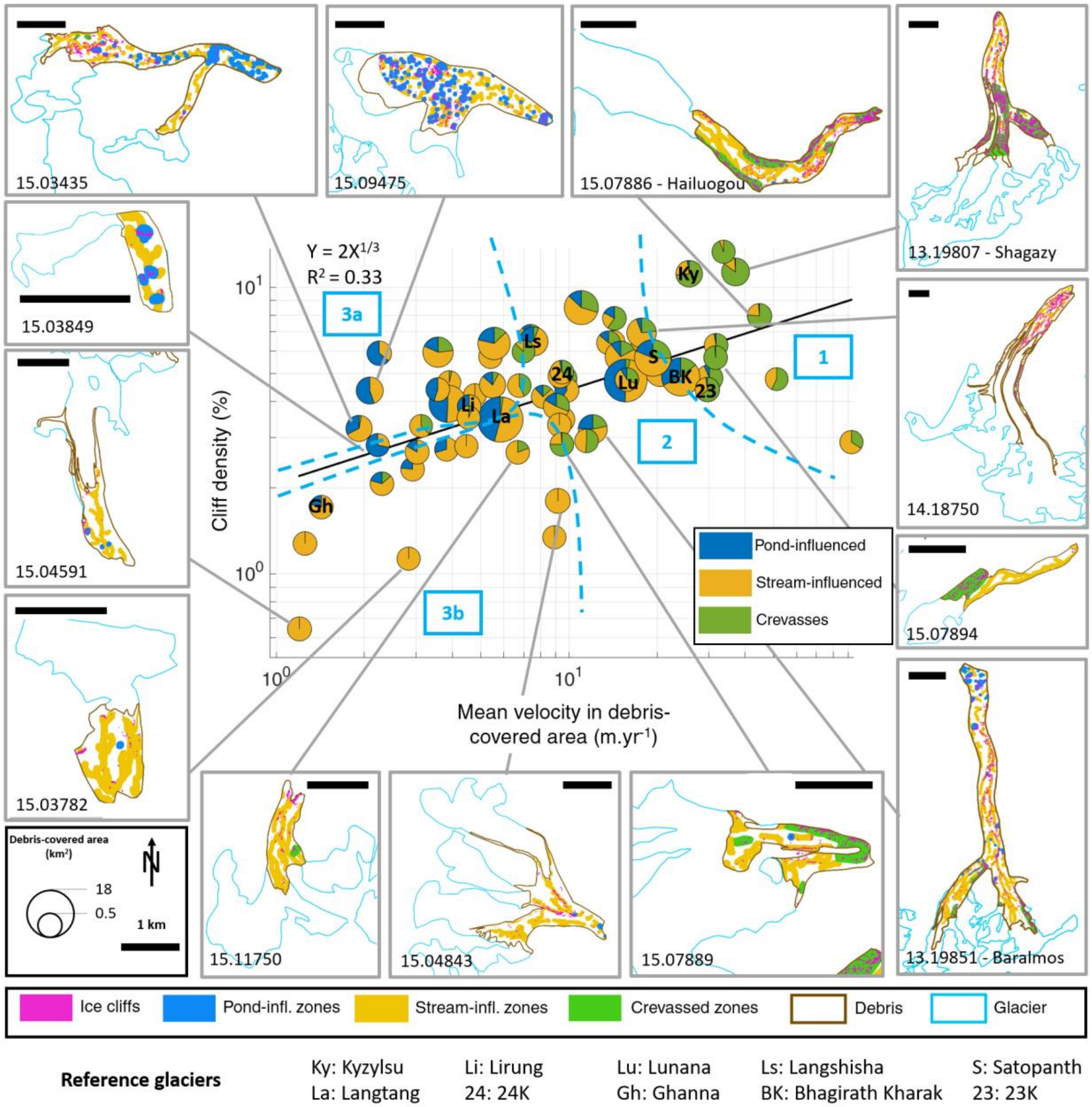

Figure 4: *Glacier-wide cliff density as a function of mean velocity in the debris-covered area for all glaciers where more than 65% of the debris-covered area could be classified. The proportion of undefined cliffs was not represented for readability. The boxes to the side show example maps of some of the glaciers with their surface classifications. Some additional reference glaciers are indicated in the main plot in black. The expression and* R^2 *of the black linear regression are indicated in the upper left corner. In light blue are shown four glacier clusters.*

4 Discussion and conclusions

We have identified the presence of supraglacial streams and ponds, along with the opening of crevasses, to be the main mechanisms responsible for ice cliff formation and development. Newly-formed cliffs tend to be smaller in size and do not have any preferential aspect (Kneib et al., 2021; Fig. S4, S5). Cliffs get reburied when they backwaste away from these supraglacial features (Fig. 2a, b), with the strong control of solar radiation on cliff survival resulting in the preferentially poleward orientation of the total ice cliff population (Buri & Pellicciotti, 2018).

4.1. Ice cliff distribution and glacier state

Velocity stands out as the main control on ice cliff density both at the local and glacier scale (Fig. 3, 4). Interlinkages with other variables means that the cliff density also responds to other local controls, and debris thickness especially, although each category of cliffs responds differently (Fig. 3). The distribution of ice cliffs therefore depends on the glacier dynamics and state. A dynamic debris-covered glacier (mean surface velocity > 10 $m.yr^{-1}$, Fig. 4, 5a, S20a) is usually characterised by thin debris and crevasses which comprise the majority of exposed ice and drain supraglacial streams. Glacier slow-down results in reduced strain rates and the migration of crevasses to the upper sections of the debris-covered area and their eventual disappearance (Fig. 3j, S20b), the extension of stream-influenced cliffs through debris destabilisation and thermo-erosional undercutting (Moore, 2018; Fig. 3a) and possibly the emergence of pond-influenced cliffs. Ponds maintain cliffs in more stagnant zones of thicker debris, also characterised by low longitudinal gradients and driving stress as well as increased hummock prevalence (Benn et al., 2017; Steiner et al., 2019; Watson, Quincey, Carrivick, et al., 2017; Fig. 5c). Such evolution has been observed on other glaciers: on Zmutt Glacier, where it was linked to the development of supraglacial valleys driven by stream incision (Mölg et al., 2020); and on Khumbu Glacier, where high relief zones characterised by growing cliffs and ponds have developed as the glacier has slowed (King et al., 2020; Rowan et al., 2021). Our large dataset enables us to show that this evolution holds across a large number of glaciers, and to identify predictors of cliff type and distribution. The development of large pond-influenced cliffs however requires the accumulation of water in surface depressions, which occurs for larger glaciers with lower longitudinal gradients (Fig. 4, 5c, S17). Most HMA glaciers in this stage of evolution are located in the Central and Eastern Himalaya (Benn et al., 2012, 2017; Racoviteanu et al., 2021; Watson et al., 2016; Watson, Quincey, Carrivick, et al., 2017; Fig. 1). However, some glaciers do not develop such drainage systems due to their relative steepness and small size, resulting in lower ice cliff densities (Fig. 4, 5d, S20d).

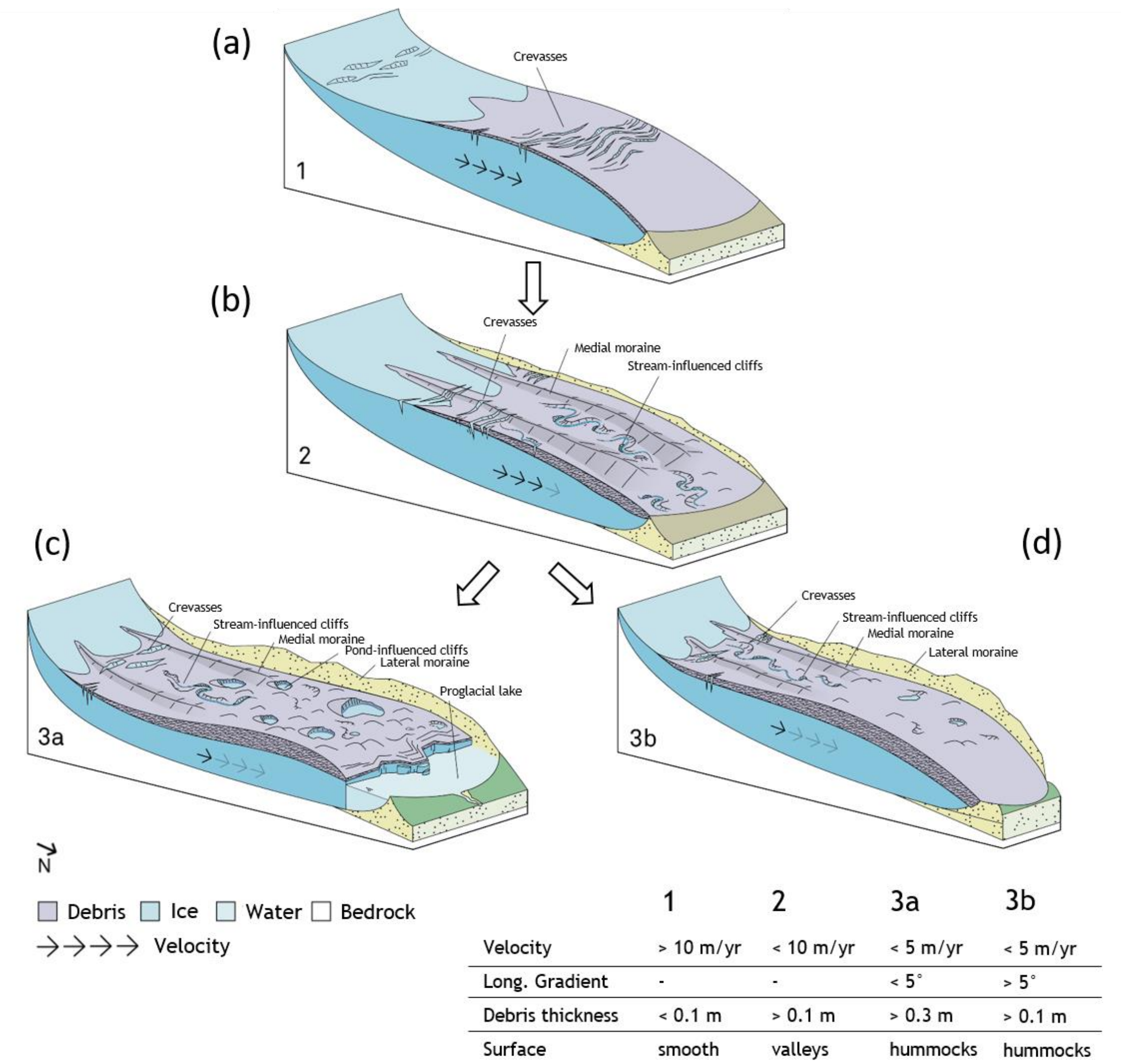

Figure 5: *The four glacier evolution states, with their ice cliff distributions. State 1: fast flowing glacier with thin debris and extensive crevassing. State 2: advanced debris cover, with thicker debris and lower velocities enabling the development of supraglacial valleys and stream-*

influenced cliffs in the non-crevassed areas. State 3a: large stagnating debris-covered tongues, characterised by hummocks, thick debris and ponds maintaining cliffs in these zones. State 3b: stagnating tongues with thick debris, but high enough longitudinal gradient or low enough surface meltwater to prevent the formation of ponds and therefore the survival of cliffs. Figure credit: Martin Heynen.

4.2. Implications for glacier mass balance

We have shown that ice cliff density and characteristics depend on the evolution state of the debris-covered glacier (Fig. 5), which is controlled mainly by dynamics (velocity) and debris thickness. Leveraging this new understanding of how glacier stage affects the presence of cliffs on their surfaces, we have provided the distribution of each type of cliff on glaciers at different stages of evolution (Fig. 3, 4, S20, Table S5). Future efforts should focus on testing the framework developed here by substantially expanding the number of data points with particular attention to include glaciers at distinct stages. Most of the debris-covered glaciers that have been the object of detailed investigations belong to glacier states 2 and 3 and efforts should be made to explore the whole range of evolution when targeting field studies. Already at this stage, however, the relationships detailed in this study outline a framework to estimate ice cliff distribution based on glacier flow characteristics, that are usually available in prognostic flow models, and debris thickness, without having to map the cliffs. Combined with cliff melt enhancement factors (E. S. Miles et al., 2022), this would allow long term estimation of the contribution of ice cliffs to debris-covered glacier mass balance - representing a key modelling advance.

Future work should also target the contribution of crevasses to glacier mass balance. Indeed, these features would likely enhance melt even more than traditional stream- and pond-influenced cliffs due to greater surface roughness at their location increasing turbulent fluxes, and additional reflected shortwave contributions from the opposite crevasse walls (Cathles et al., 2011; Colgan et al., 2016; W. T. Pfeffer & Bretherton, 1987; Purdie et al., 2022). Time-lapse images actually show the upper walls of crevasses backwasting as traditional ice cliffs would (Fig. S21).

Furthermore, their longer-term evolution and influence on shaping the debris-covered glacier surface remains unclear (Kirkbride & Deline, 2013).

Acknowledgments

This project has received funding from the European Research Council (ERC) under the European Union's Horizon 2020 programme (grant agreement 772751) and from the Royal Society via a Newton Advanced Fellowship award (NA170325). The majority of the Pléiades stereo-pairs were provided by Etienne Berthier via the Pléiades Glacier Observatory (PGO) initiative of the French Space Agency (CNES). The remaining images were acquired through the CNES ISIS Programme. We thank the team of the Centre for Research on Glaciers at the Academy of Sciences of Tajikistan who enabled our 2021 fieldwork on Kyzylsu Glacier.

Open Research

The glacier, debris, crevasse, cliff and pond outlines will be made available on Zenodo. Other datasets used include surface velocity from Millan et al. (2022), climate data from ERA5-Land (Muñoz Sabater, 2019), RGI 6.0. glacier outlines (https://nsidc.org/data/nsidc-0770/versions/6), the AW3D 30m DEM (Tadono et al., 2014) and ice thicknesses (Farinotti et al., 2019). Atmospherically-corrected Sentinel-2 images prior to 2019 were obtained from CNES through the PEPS platform (Hagolle et al., 2015). From 2019 and later they were processed directly in Google Earth Engine.

References

Anderson, L. S., Armstrong, W. H., Anderson, R. S., & Buri, P. (2021). Debris cover and the thinning of Kennicott Glacier, Alaska: In situ measurements, automated ice cliff delineation and distributed melt estimates. *Cryosphere*, *15*(1), 265–282. https://doi.org/10.5194/tc-15-265-2021

Anderson, L. S., Armstrong, W. H., Anderson, R. S., Scherler, D., & Petersen, E. (2021). The Causes of Debris-Covered Glacier Thinning: Evidence for the Importance of Ice Dynamics

From Kennicott Glacier, Alaska. *Frontiers in Earth Science, 0*, 723. https://doi.org/10.3389/FEART.2021.680995

Bartlett, O. T., Ng, F. S. L., & Rowan, A. V. (2020). Morphology and evolution of supraglacial hummocks on debris-covered Himalayan glaciers. *Earth Surface Processes and Landforms*, esp.5043. https://doi.org/10.1002/esp.5043

Benn, D. I., Wiseman, S., & Hands, K. A. (2001). Growth and drainage of supraglacial lakes on debrismantled Ngozumpa Glacier, Khumbu Himal, Nepal. *Journal of Glaciology*, *47*(159), 626–638. https://doi.org/10.3189/172756501781831729

Benn, D. I., Bolch, T., Hands, K., Gulley, J., Luckman, A., Nicholson, L. I., et al. (2012, August). Response of debris-covered glaciers in the Mount Everest region to recent warming, and implications for outburst flood hazards. *Earth-Science Reviews*. https://doi.org/10.1016/j.earscirev.2012.03.008

Benn, Douglas I, Thompson, S., Gulley, J., Mertes, J., Luckman, A., & Nicholson, L. (2017). Structure and evolution of the drainage system of a Himalayan debris-covered glacier, and its relationship with patterns of mass loss. *The Cryosphere*, *11*. https://doi.org/10.5194/tc-11-2247-2017

Berthier, E., Vincent, C., Magnússon, E., Gunnlaugsson, Á. Þ., Pitte, P., Le Meur, E., et al. (2014). Glacier topography and elevation changes derived from Pléiades sub-meter stereo images. *The Cryosphere*, *8*, 2275–2291. https://doi.org/10.5194/tc-8-2275-2014

Bolch, T., Buchroithner, M. F., Peters, J., Baessler, M., & Bajracharya, S. (2008). Identification of glacier motion and potentially dangerous glacial lakes in the Mt. Everest region/Nepal using spaceborne imagery. *Natural Hazards and Earth System Sciences*, *8*(6), 1329–1340. https://doi.org/10.5194/nhess-8-1329-2008

Brun, F., Buri, P., Miles, E. S., Wagnon, P., Steiner, J., Berthier, E., et al. (2016). Quantifying volume loss from ice cliffs on debris-covered glaciers using high-resolution terrestrial and aerial photogrammetry. *Journal of Glaciology*. https://doi.org/10.1017/jog.2016.54

Brun, F., Wagnon, P., Berthier, E., Shea, J. M., Immerzeel, W. W., Kraaijenbrink, P. D. A., et al. (2018). Ice cliff contribution to the tongue-wide ablation of Changri Nup Glacier, Nepal, central Himalaya. *The Cryosphere*, *12*(11), 3439–3457. https://doi.org/10.5194/tc-12-3439-2018

Buri, P., & Pellicciotti, F. (2018). Aspect controls the survival of ice cliffs on debris-covered glaciers. *Proceedings of the National Academy of Sciences*, *115*(17), 4369–4374. https://doi.org/10.1073/pnas.1713892115

Buri, P., Pellicciotti, F., Steiner, J. F., Miles, E. S., & Immerzeel, W. W. (2016). A grid-based model of backwasting of supraglacial ice cliffs on debris-covered glaciers. *Annals of Glaciology*, *57*(71), 199–211. https://doi.org/10.3189/2016AoG71A059

Buri, P., Miles, E. S., Steiner, J. F., Ragettli, S., & Pellicciotti, F. (2021). Supraglacial Ice Cliffs Can Substantially Increase the Mass Loss of Debris-Covered Glaciers. *Geophysical Research Letters*, *48*(6). https://doi.org/10.1029/2020GL092150

Cathles, L. M., Abbot, D. S., Bassis, J. N., & MacAyeal, D. R. (2011). Modeling surface-roughness/solar-ablation feedback: application to small-scale surface channels and crevasses of the Greenland ice sheet. *Annals of Glaciology*, *52*(59), 99–108. https://doi.org/10.3189/172756411799096268

Colgan, W., Rajaram, H., Abdalati, W., McCutchan, C., Mottram, R., Moussavi, M. S., & Grigsby, S. (2016, March 1). Glacier crevasses: Observations, models, and mass balance implications. *Reviews of Geophysics*. Blackwell Publishing Ltd.

https://doi.org/10.1002/2015RG000504

Compagno, L., Huss, M., Miles, E. S., McCarthy, M. J., Zekollari, H., Dehecq, A., et al. (2022). Modelling supraglacial debris-cover evolution from the single-glacier to the regional scale: an application to High Mountain Asia. *The Cryosphere*, *16*(5), 1697–1718. https://doi.org/10.5194/tc-16-1697-2022

Dehecq, A., Gourmelen, N., Gardner, A. S., Brun, F., Goldberg, D., Nienow, P. W., et al. (2019). Twenty-first century glacier slowdown driven by mass loss in High Mountain Asia. *Nature Geoscience*, *12*(1), 22–27. https://doi.org/10.1038/s41561-018-0271-9

Egli, P. E., Belotti, B., Ouvry, B., Irving, J., & Lane, S. N. (2021). Subglacial Channels, Climate Warming, and Increasing Frequency of Alpine Glacier Snout Collapse. *Geophysical Research Letters*, *48*(21). https://doi.org/10.1029/2021GL096031

Falaschi, D., Rivera, A., Lo Vecchio Repetto, A., Moragues, S., Villalba, R., Rastner, P., et al. (2021). Evolution of Surface Characteristics of Three Debris-Covered Glaciers in the Patagonian Andes From 1958 to 2020. *Frontiers in Earth Science*, *9*. https://doi.org/10.3389/feart.2021.671854

Farinotti, D., Huss, M., Fürst, J. J., Landmann, J., Machguth, H., Maussion, F., & Pandit, A. (2019). A consensus estimate for the ice thickness distribution of all glaciers on Earth. *Nature Geoscience*, *12*(3), 168–173. https://doi.org/10.1038/s41561-019-0300-3

Ferguson, J. C., & Vieli, A. (2021). Modelling steady states and the transient response of debris-covered glaciers. *The Cryosphere*, *15*(7), 3377–3399. https://doi.org/10.5194/tc-15-3377-2021

Gulley, J. D., Benn, D. I., Screaton, E., & Martin, J. (2009). Mechanisms of englacial conduit formation and their implications for subglacial recharge. *Quaternary Science Reviews*, *28*(19–20), 1984–1999. https://doi.org/10.1016/j.quascirev.2009.04.002

Hagolle, O., Huc, M., Villa Pascual, D., & Dedieu, G. (2015). A Multi-Temporal and Multi-Spectral Method to Estimate Aerosol Optical Thickness over Land, for the Atmospheric Correction of FormoSat-2, LandSat, VENμS and Sentinel-2 Images. *Remote Sensing*, *7*(3), 2668–2691. https://doi.org/10.3390/rs70302668

Herreid, S., & Pellicciotti, F. (2018). Automated detection of ice cliffs within supraglacial debris cover. *The Cryosphere*, *12*, 1811–1829. https://doi.org/10.5194/tc-12-1811-2018

Herreid, S., & Pellicciotti, F. (2020). The state of rock debris covering Earth's glaciers. *Nature Geoscience*, 1–7. https://doi.org/10.1038/s41561-020-0615-0

Immerzeel, W. W., Kraaijenbrink, P. D. A., Shea, J. M., Shrestha, A. B., Pellicciotti, F., Bierkens, M. F. P., & De Jong, S. M. (2014). High-resolution monitoring of Himalayan glacier dynamics using unmanned aerial vehicles. *Remote Sensing of Environment*, *150*, 93–103. https://doi.org/10.1016/j.rse.2014.04.025

Kienholz, C., Rich, J. L., Arendt, A. A., & Hock, R. (2014). A new method for deriving glacier centerlines applied to glaciers in Alaska and northwest Canada. *The Cryosphere*, *8*(2), 503–519. https://doi.org/10.5194/tc-8-503-2014

King, O., Turner, A. G. D., Quincey, D. J., & Carrivick, J. L. (2020). Morphometric evolution of Everest region debris-covered glaciers. *Geomorphology*, *371*, 107422. https://doi.org/10.1016/j.geomorph.2020.107422

Kirkbride, M. P., & Deline, P. (2013). The formation of supraglacial debris covers by primary dispersal from transverse englacial debris bands. *Earth Surface Processes and Landforms*, *38*(15), 1779–1792. https://doi.org/10.1002/esp.3416

Kneib, M., Miles, E. S., Jola, S., Buri, P., Herreid, S., Bhattacharya, A., et al. (2020). Mapping ice cliffs on debris-covered glaciers using multispectral satellite images. *Remote Sensing of Environment*, 112201. https://doi.org/10.1016/j.rse.2020.112201

Kneib, M., Miles, E. S., Buri, P., Molnar, P., McCarthy, M., Fugger, S., & Pellicciotti, F. (2021). Interannual Dynamics of Ice Cliff Populations on Debris-Covered Glaciers From Remote Sensing Observations and Stochastic Modeling. *Journal of Geophysical Research: Earth Surface*, *126*(10). https://doi.org/10.1029/2021JF006179

Kneib, Marin, Miles, E. S., Buri, P., Fugger, S., McCarthy, M., Shaw, T. E., et al. (2022). Sub-seasonal variability of supraglacial ice cliff melt rates and associated processes from time-lapse photogrammetry. *The Cryosphere*, *16*(11), 4701–4725. https://doi.org/10.5194/tc-16-4701-2022

Kraaijenbrink, P. D. A., Shea, J. M., Pellicciotti, F., De Jong, S. M., & Immerzeel, W. W. (2016). Object-based analysis of unmanned aerial vehicle imagery to map and characterise surface features on a debris-covered glacier. *Remote Sensing of Environment*, *186*, 581–595. https://doi.org/10.1016/j.rse.2016.09.013

Loriaux, T., & Ruiz, L. (2021). Spatio-Temporal Distribution of Supra-Glacial Ponds and Ice Cliffs on Verde Glacier, Chile. *Frontiers in Earth Science*, *9*. https://doi.org/10.3389/feart.2021.681071

McCarthy, M., Miles, E., Kneib, M., Buri, P., Fugger, S., & Pellicciotti, F. (2022). Supraglacial debris thickness and supply rate in High-Mountain Asia. *Communications Earth & Environment*, *3*(1), 269. https://doi.org/10.1038/s43247-022-00588-2

McFeeters, S. K. (1996). The use of the Normalized Difference Water Index (NDWI) in the delineation of open water features. *International Journal of Remote Sensing*, *17*(7), 1425–1432. https://doi.org/10.1080/01431169608948714

Miles, E. S., Willis, I. C., Arnold, N. S., Steiner, J., & Pellicciotti, F. (2017). Spatial, seasonal and interannual variability of supraglacial ponds in the Langtang Valley of Nepal, 1999-2013. https://doi.org/10.1017/jog.2016.120

Miles, E. S., Watson, C. S., Brun, F., Berthier, E., Esteves, M., Quincey, D. J., et al. (2018). Glacial and geomorphic effects of a supraglacial lake drainage and outburst event, Everest region, Nepal Himalaya. *The Cryosphere*, *12*, 3891–3905. https://doi.org/10.5194/tc-12-3891-2018

Miles, E. S., Willis, I., Buri, P., Steiner, J. F., Arnold, N. S., & Pellicciotti, F. (2018). Surface Pond Energy Absorption Across Four Himalayan Glaciers Accounts for 1/8 of Total Catchment Ice Loss. *Geophysical Research Letters*, *45*(19), 10,464-10,473. https://doi.org/10.1029/2018GL079678

Miles, E. S., Steiner, J. F., Buri, P., Immerzeel, W. W., & Pellicciotti, F. (2022). Controls on the relative melt rates of debris-covered glacier surfaces. *Environmental Research Letters*, *17*(6), 064004. https://doi.org/10.1088/1748-9326/ac6966

Miles, K. E., Hubbard, B., Irvine-Fynn, T. D. L., Miles, E., Quincey, D. J., & Rowan, A. V. (2020, August 1). Hydrology of debris-covered glaciers in High Mountain Asia. *Earth-Science Reviews*. Elsevier B.V. https://doi.org/10.1016/j.earscirev.2020.103212

Millan, R., Mouginot, J., Rabatel, A., & Morlighem, M. (2022). Ice velocity and thickness of the world’s glaciers. *Nature Geoscience*, *15*(2), 124–129. https://doi.org/10.1038/s41561-021-00885-z

Mölg, N., Bolch, T., Walter, A., & Vieli, A. (2019). Unravelling the evolution of Zmuttgletscher and its debris cover since the end of the Little Ice Age. *The Cryosphere*, *13*(7), 1889–1909. https://doi.org/10.5194/tc-13-1889-2019

Mölg, N., Ferguson, J., Bolch, T., & Vieli, A. (2020). On the influence of debris cover on glacier morphology: How high-relief structures evolve from smooth surfaces. *Geomorphology*, *357*, 107092. https://doi.org/10.1016/j.geomorph.2020.107092

Moore, P. L. (2018). Stability of supraglacial debris. *Earth Surface Processes and Landforms*, *43*(1), 285–297. https://doi.org/10.1002/esp.4244

Moore, P. L. (2021). Numerical Simulation of Supraglacial Debris Mobility: Implications for Ablation and Landform Genesis. *Frontiers in Earth Science*, *9*. https://doi.org/10.3389/feart.2021.710131

Muñoz Sabater, J. (2019). ERA5-Land monthly averaged data from 1981 to present. *Copernicus Climate Change Service (C3S) Climate Data Store (CDS)*. https://doi.org/10.24381/cds.68d2bb30

Nicholson, L. I., McCarthy, M., Pritchard, H. D., & Willis, I. (2018). Supraglacial debris thickness variability: Impact on ablation and relation to terrain properties. *Cryosphere*, *12*(12), 3719–3734. https://doi.org/10.5194/tc-12-3719-2018

Pellicciotti, F., Stephan, C., Miles, E. S., Herreid, S., Immerzeel, W. W., & Bolch, T. (2015). Mass-balance changes of the debris-covered glaciers in the Langtang Himal, Nepal, from 1974 to 1999. *Journal of Glaciology*, *61*(226), 373–386. https://doi.org/10.3189/2015JoG13J237

Pfeffer, W. T., & Bretherton, C. S. (1987). The effect of crevasses on the solar heating of a glacier surface. *The Physical Basis of Ice Sheet Modelling*, *170*, 191–205.

Pfeffer, W. Tad, Arendt, A. A., Bliss, A., Bolch, T., Cogley, J. G., Gardner, A. S., et al. (2014). The randolph glacier inventory: A globally complete inventory of glaciers. *Journal of Glaciology*, *60*(221), 537–552. https://doi.org/10.3189/2014JoG13J176

Purdie, H., Zawar-Reza, P., Katurji, M., Schumacher, B., Kerr, T., & Bealing, P. (2022). Variability in the vertical temperature profile within crevasses at an alpine glacier. *Journal of Glaciology*, 1–15. https://doi.org/10.1017/jog.2022.73

Quincey, D. J., & Glasser, N. F. (2009). Morphological and ice-dynamical changes on the Tasman Glacier, New Zealand, 1990-2007. *Global and Planetary Change*, *68*(3), 185–197. https://doi.org/10.1016/j.gloplacha.2009.05.003

Quincey, D. J., Richardson, S. D., Luckman, A., Lucas, R. M., Reynolds, J. M., Hambrey, M. J., & Glasser, N. F. (2007). Early recognition of glacial lake hazards in the Himalaya using remote sensing datasets. *Global and Planetary Change*, *56*(1–2), 137–152. https://doi.org/10.1016/j.gloplacha.2006.07.013

Racoviteanu, A. E., Nicholson, L., & Glasser, N. F. (2021). Surface composition of debris-covered glaciers across the Himalaya using linear spectral unmixing of Landsat 8 OLI imagery. *The Cryosphere*, *15*, 4557–4588. https://doi.org/10.5194/tc-15-4557-2021

Racoviteanu, A. E., Glasser, N. F., Robson, B. A., Harrison, S., Millan, R., Kayastha, R. B., & Kayastha, R. (2022). Recent Evolution of Glaciers in the Manaslu Region of Nepal From Satellite Imagery and UAV Data (1970–2019). *Frontiers in Earth Science*, *9*. https://doi.org/10.3389/feart.2021.767317

Reid, T. D., & Brock, B. W. (2014). Assessing ice-cliff backwasting and its contribution to total ablation of debris-covered Miage glacier, Mont Blanc massif, Italy. *Journal of Glaciology*. https://doi.org/10.3189/2014JoG13J045

Reynolds, J. (2000). On the formation of supraglacial lakes on debris-covered glaciers. *IAHS-AISH Publication*, *264*, 153–161.

Röhl, K. (2006). Thermo-erosional notch development at fresh-water-calving Tasman Glacier, New Zealand. *Journal of Glaciology*, *52*(177), 203–213. https://doi.org/10.3189/172756506781828773

Röhl, K. (2008). Characteristics and evolution of supraglacial ponds on debris-covered Tasman Glacier, New Zealand. *Journal of Glaciology*. https://doi.org/10.3189/002214308787779861

Rounce, D. R., Hock, R., McNabb, R. W., Millan, R., Sommer, C., Braun, M. H., et al. (2021). Distributed global debris thickness estimates reveal debris significantly impacts glacier mass balance. *Geophysical Research Letters*, e2020GL091311. https://doi.org/10.1029/2020GL091311

Rowan, A. V., Egholm, D. L., Quincey, D. J., Hubbard, B., King, O., Miles, E. S., et al. (2021). The Role of Differential Ablation and Dynamic Detachment in Driving Accelerating Mass Loss From a Debris-Covered Himalayan Glacier. *Journal of Geophysical Research: Earth Surface*, *126*(9), e2020JF005761. https://doi.org/10.1029/2020JF005761

Sakai, A., & Fujita, K. (2010). Formation conditions of supraglacial lakes on debriscovered glaciers in the Himalaya. *Journal of Glaciology*, *56*(195), 177–181. https://doi.org/10.3189/002214310791190785

Sakai, A., & Takeuchi, N. (2000). *Debris-Covered Glaciers*. IAHS Publ.

Sakai, A., Nakawo, M., & Fujita, K. (1998). Melt rate of ice cliffs on the Lirung Glacier, Nepal Himalayas, 1996. *Bulletin of Glacier Research*, *16*, 57–66.

Sakai, A., Nakawo, M., & Fujita, K. (2002). Distribution Characteristics and Energy Balance of Ice Cliffs on Debris-covered Glaciers, Nepal Himalaya. *Arctic, Antarctic, and Alpine Research*, *34*(1), 12–19. https://doi.org/10.1080/15230430.2002.12003463

Salerno, F., Thakuri, S., D'Agata, C., Smiraglia, C., Manfredi, E. C., Viviano, G., & Tartari, G.

(2012). Glacial lake distribution in the Mount Everest region: Uncertainty of measurement and conditions of formation. *Global and Planetary Change*, *92–93*, 30–39. https://doi.org/10.1016/j.gloplacha.2012.04.001

Sato, Y., Fujita, K., Inoue, H., Sunako, S., Sakai, A., Tsushima, A., et al. (2021). Ice Cliff Dynamics of Debris-Covered Trakarding Glacier in the Rolwaling Region, Nepal Himalaya. *Frontiers in Earth Science*, *9*, 398. https://doi.org/10.3389/FEART.2021.623623/BIBTEX

Scherler, D., Wulf, H., & Gorelick, N. (2018). Global Assessment of Supraglacial Debris-Cover Extents. *Geophysical Research Letters*. https://doi.org/10.1029/2018GL080158

Schwanghart, W., & Scherler, D. (2014). Short Communication: TopoToolbox 2 – MATLAB-based software for topographic analysis and modeling in Earth surface sciences. *Earth Surface Dynamics*, *2*(1), 1–7. https://doi.org/10.5194/esurf-2-1-2014

Sharp, R. P. (1949). Studies of superglacial debris on valley glaciers. *American Journal of Science*, *247*(5), 289–315. https://doi.org/10.2475/ajs.247.5.289

Shean, D. E., Alexandrov, O., Moratto, Z. M., Smith, B. E., Joughin, I. R., Porter, C., & Morin, P. (2016). An automated, open-source pipeline for mass production of digital elevation models (DEMs) from very-high-resolution commercial stereo satellite imagery. *ISPRS Journal of Photogrammetry and Remote Sensing*, *116*, 101–117. https://doi.org/10.1016/j.isprsjprs.2016.03.012

Steiner, J. F., Buri, P., Miles, E. S., Ragettli, S., & Pellicciotti, F. (2019). Supraglacial ice cliffs and ponds on debris-covered glaciers: Spatio-temporal distribution and characteristics. *Journal of Glaciology*, *65*(252), 617–632. https://doi.org/10.1017/jog.2019.40

Stokes, C. R., Popovnin, V., Aleynikov, A., Gurney, S. D., & Shahgedanova, M. (2007). Recent glacier retreat in the Caucasus Mountains, Russia, and associated increase in supraglacial debris cover and supra-/proglacial lake development. In *Annals of Glaciology* (Vol. 46, pp. 195–203). https://doi.org/10.3189/172756407782871468

Tadono, T., Ishida, H., Oda, F., Naito, S., Minakawa, K., & Iwamoto, H. (2014). Precise Global DEM Generation by ALOS PRISM. *ISPRS Annals of the Photogrammetry, Remote Sensing and Spatial Information Sciences*, *II–4*, 71–76. https://doi.org/10.5194/isprsannals-II-4-71-2014

Watson, C. S., Quincey, D. J., Carrivick, J. L., & Smith, M. W. (2016). The dynamics of supraglacial ponds in the Everest region, central Himalaya. *Global and Planetary Change*, *142*, 14–27. https://doi.org/https://doi.org/10.1016/j.gloplacha.2016.04.008

Watson, C. S., Quincey, D. J., Carrivick, J. L., & Smith, M. W. (2017). Ice cliff dynamics in the Everest region of the Central Himalaya. *Geomorphology*, *278*, 238–251. https://doi.org/10.1016/j.geomorph.2016.11.017

Watson, C. S., Quincey, D. J., Smith, M. W., Carrivick, J. L., Rowan, A. V, & James, M. R. (2017). Quantifying ice cliff evolution with multi-temporal point clouds on the debris-covered Khumbu Glacier, Nepal. https://doi.org/10.1017/jog.2017.47

Watson, C. S., King, O., Miles, E. S., & Quincey, D. J. (2018). Optimising NDWI supraglacial pond classification on Himalayan debris-covered glaciers. *Remote Sensing of Environment*, *217*, 414–425. https://doi.org/10.1016/j.rse.2018.08.020

Additional references in supporting information

Fugger, S., Fyffe, C.L., Fatichi, S., Miles, E., McCarthy, M., Shaw, T.E., Ding, B., Yang, W., Wagnon, P., Immerzeel, W., Liu, Q., Pellicciotti, F., 2022. Understanding monsoon controls on the energy and mass balance of glaciers in the Central and Eastern Himalaya. Cryosph. 16, 1631–1652. https://doi.org/10.5194/tc-16-1631-2022

Geophysical Research Letters

Supporting Information for

Controls on Ice Cliff Formation, Distribution and Characteristics on Debris-Covered Glaciers

M. Kneib[1, 2], Catriona Fyffe[3], Evan S. Miles[1], Shayna Lindemann[1], Thomas E. Shaw[1], Pascal Buri[1], Michael McCarthy[1], Boris Ouvry[4], Andreas Vieli[4], Yota Sato[5], Philip D.A Kraaijenbrink[6], Chuanxi Zhao[7,8], Peter Molnar[2], Francesca Pellicciotti[1,3]

[1] High Mountain Glaciers and Hydrology Group, Swiss Federal Institute, WSL, Birmensdorf, Switzerland.

[2] Institute of Environmental Engineering, ETH Zürich, Zürich, Switzerland

[3] Department of Geography and Environmental Sciences, Northumbria University, Newcastle upon Tyne, UK

[4] Department of Geography, University of Zurich, 8057 Zurich, Switzerland

[5] Graduate School of Environmental Studies, Nagoya University, Nagoya, Japan

[6] Utrecht University, Department of Physical Geography, PO Box 80115, 3508 TC, Utrecht, The Netherlands.

[7] College of Earth and Environmental Sciences, Lanzhou University, Lanzhou 730000, China

[8] State Key Laboratory of Tibetan Plateau Earth System, Environment and Resources (TPESER), Institute of Tibetan Plateau Research, Chinese Academy of Sciences

Contents of this file

Text S1 to S2
Figures S1 to S21
Tables S1 to S5

Text S1. Ice cliff formation

1.1. Multi-temporal UAV data

Here we took advantage of multi-temporal Unsupervised Aerial Vehicle (UAV) surveys over portions of five of the studied glaciers: Trakarding, Langtang, Lirung, 23K and 24K Glaciers (Brun et al., 2016; Chuanxi et al., in prep; Immerzeel et al., 2014; Kraaijenbrink et al., in prep; Sato et al., 2021; Table S1; Fig. S1). The surveys were conducted over a period of 2-5 years, with a repeat time of at least one year (Table S1). The resolution of the original DEMs and orthoimages varied between 0.1 and 0.2 m, and they were all co-registered using surrounding stable terrain (see details in Chuanxi et al., in prep.; Kraaijenbrink et al., in prep.; Sato et al., 2021;). From 2016 we used all available cloudless Sentinel-2 images (10m resolution) of the survey domains taken during the melt season to identify seasonal ponds. These images were atmospherically-corrected using the MAJA processing workflow (Hagolle et al., 2015).

1.2. Identification of newly-formed ice cliffs

We manually identified newly-formed cliffs in the orthoimages as patches of bare ice that were not visible in previous images, irrespective of their slope, accounting for glacier flow (Kneib et al., 2021). The outlines of these newly-formed cliffs were further derived manually. The DEMs were resampled to 1m to derive slope and aspect of all pixels, and to map supraglacial channels using a flow-routing algorithm following the same approach as for the Pléiades DEMs (Schwangart & Scherler, 2014).

The mechanisms underlying the ice cliff formation were determined by a single operator based on 1/ the proximity to ponds (including seasonal ponds identified in the Sentinel-2 images), visible streams or supraglacial channels and 2/ the initial shape of the cliffs and the general organisation of the glacier surface at this location. This classification, as well as the ice cliff outlines, were then validated by a second independent operator.

1.3. Main results

We identified 202 newly-formed cliffs (38 for Langtang, 27 for Lirung, 57 for Trakarding, 38 for 23K and 42 for 24K) and classified the formation mechanisms as ‘pond-influenced’, ‘stream-influenced’, ‘crevasses’ or ‘undefined’ when the formation mechanism was not clear. Since the same classification was used for newly-formed cliffs and the entire cliff population, we could directly compare the characteristics of the newly-formed cliff pixels with the values obtained from looking at the entire cliff population with the Pléiades data, specifically for the UAV survey domains (Fig. S2-S5).

The proportion of cliff categories was mostly consistent between newly-formed cliffs and the entire cliff population, except for Lirung where the triggering mechanism for most newly-formed cliffs could not be determined, and for Trakarding, where the proportion of pond-influenced new cliffs was greater (Fig. S2). There were no consistent differences in the slope distribution of the newly-formed cliffs and the whole cliff population within these five domains. The slope of crevasses was consistently shallower, which was likely due to the DEM resolution being too coarse to represent their slope accurately.The slope distribution of the stream-influenced, pond-influenced and undefined cliffs was overall similar for the total cliff population, while the slope of the newly-formed pond-influenced cliffs tended to be steeper than for the other categories (Fig. S3). The most striking differences were visible in the aspect distributions, where the full cliff population was generally oriented north-west to north, except for Lirung, while the newly-formed cliffs seemed to either be completely random (e.g. for Trakarding) or preferentially oriented in the general glacier flow direction (Fig. S4). In terms of cliff size, the newly-formed cliffs were consistently smaller, and so for all categories (Fig. S5).

1.4. Discussion points

This focused study of the characteristics of newly-formed cliffs enabled us to link ice cliff formation with ice cliff distribution. Ice cliff formation mechanisms are indeed expected to have a strong influence on the distribution of ice cliffs across the glacier surface due to the high cliff birth and death rates (Kneib et al., 2021). The relatively long-term monitoring periods and the large number of sites covered here, with various glaciological and climatic characteristics (Fugger et al., 2022; Kneib et al., 2022; Sato et al., 2021), enabled us to identify a large number of ice cliff formation events and outline a number of interesting patterns. The main outcome was that as for ice cliff distribution, the formation mechanisms were driven by the glacier hydrology, including the proglacial or englacial hydrology for some of the crevasse-opening scenarios (Fig. S6). Other interesting findings were that there was no preferential north-facing aspect for newly-formed cliffs, which was additional evidence for the faster reburial of south-facing cliffs (Buri & Pellicciotti, 2018). Additionally, newly-formed cliffs tended to be smaller in size, which confirmed the observations made at other sites with coarser resolution sensors (Kneib et al., 2021).

There remained limitations in the analysis of these patterns due to the relatively small area covered and the observational bias to the lower part of the debris-covered area of these glaciers. Additionally, despite the relatively high frequency of repeat surveys, the time intervals usually remained too long to precisely describe the formation mechanisms (Kneib et al., 2022). For instance, the 'pond-influenced' formations could have been due to pond drainage or filling, but this was not always clear due to too long time intervals between images so we kept the generic term. Similarly for 'stream-influenced' formations, the exact mechanism was not always clear and the presence of water in the channel could not always be verified from the images (based on field observations from the various sites we anyway expected the water level in the streams to vary considerably seasonally), so a classification based on the presence of meanders in the surface DEMs was usually a strong argument to classify the newly-formed cliffs as stream-influenced. Crevasses were easily identifiable from their elongated, sometimes slightly curved shapes, but the triggering mechanism responsible for crevasse opening could not always be clearly identified (Reid & Brock, 2014; Steiner et al., 2019) and could vary from simple shear at the glacier lateral margins (for 24K especially) to the influence of proglacial lakes or streams entering the glacier laterally (for Trakarding especially, Fig. S6). We did not see any evidence of englacial conduit collapse for the duration of the monitoring periods, although the development of concentric crevasses preluding some of these events on debris-covered glaciers have been described at several locations in the Swiss Alps (Mölg et al., 2019; Egli et al., 2021; Fig. S6). Similarly, we did not have enough evidence to categorize formation events as being solely caused by slope steepening from differential melt, and for the large majority of events the hydrology or the glacier dynamics seemed to play a decisive role (Sharp, 1949; Moore, 2021). These formation events were actually most likely due to a combination of factors leading to slope steepening prior to the emergence of the new cliff, and the formation mechanisms that we identified most likely mainly reflected the 'triggering' event leading to debris removal and cliff formation.

Text S2. Ice cliff, pond and stream delineation

Ice cliffs and ponds were derived automatically in each Pléiades scene following the Spectral Curvature method for cliffs, which is based solely on spectral characteristics (Kneib et al., 2020), and the Normalized Difference Water Index (NDWI) for ponds (McFeeters, 1998; Watson et al., 2016; 2018; Miles et al., 2017b). False positive identifications due to local shadows or changing geology were filtered out manually (Fig. S7, S8).

We accounted for pond seasonality by automatically mapping areas with a Normalized Difference Water Index (NDWI) value greater than 0.1 in all 10 m resolution Sentinel-2 images of the previous melt season (May-November), after filtering clouds and shaded areas (Kneib et al., 2020; McFeeters et al., 1998; Watson et al., 2018). We retained as ponds (at least temporary ones) the areas for which more than three cloudless Sentinel-2 images were available and where the NDWI was greater than 0.1 more than 33% of the time. False positives were removed manually and the resulting pond density values are consistent with the ones from the Pléiades images (Fig. S9) and additionally account for strong seasonal variability at some of the sites (E. S. Miles et al., 2017b; Watson et al., 2016). The final pond outlines were defined as the union between the Pléiades and Sentinel-2 outlines.

The minimum cliff and pond detection size is given by the resolution of the Pléiades data (2m). The uncertainties in the mapping of cliffs and ponds were assessed by eroding and dilating the mapped features by 0.5 pixels (1 m for cliffs, 5 m for ponds), and taking the upper (+42% for cliffs, +77% for ponds) and lower (-38% and -49%) area bounds as uncertainty values (Brun et al., 2018; Fig. S10). The Pléiades outlines were validated at one of the glaciers with near-contemporaneous outlines obtained from a 1m-resolution UAV orthoimage (Fig. S11).

Using the Pléiades DEMs, we mapped supraglacial channels (used as a proxy for supraglacial streams) across all the glaciers using the TopoToolbox flow routing algorithm (Schwangart & Scherler, 2014), after filling the DEM sinks shallower than 5m and removing the crevassed areas. These 'streams' were defined as the pixels with a contributing upstream area higher than 10000 m^2 and were used to calculate stream sinuosity (Anderson, Armstrong, Anderson, Scherler et al., 2021; Mölg et al., 2020).

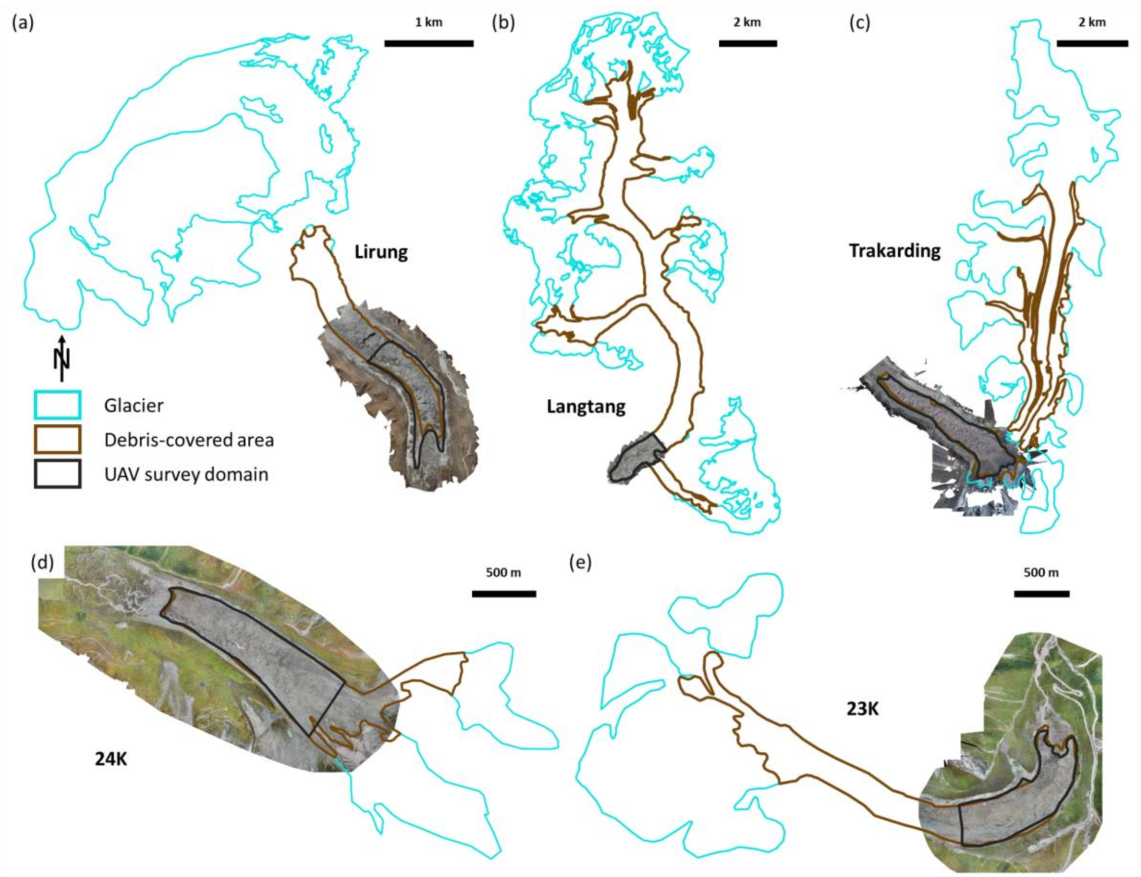

Figure S1. UAV survey domain for each glacier. Background images are the (a) Lirung 10/2017, (b) Langtang 04/2018, (c) Trakarding 10/2017, (d) 24K 09/2018 and (e) 23K 09/2018 UAV orthoimages. Glacier and debris outlines are the ones derived from the corresponding Pléiades images.

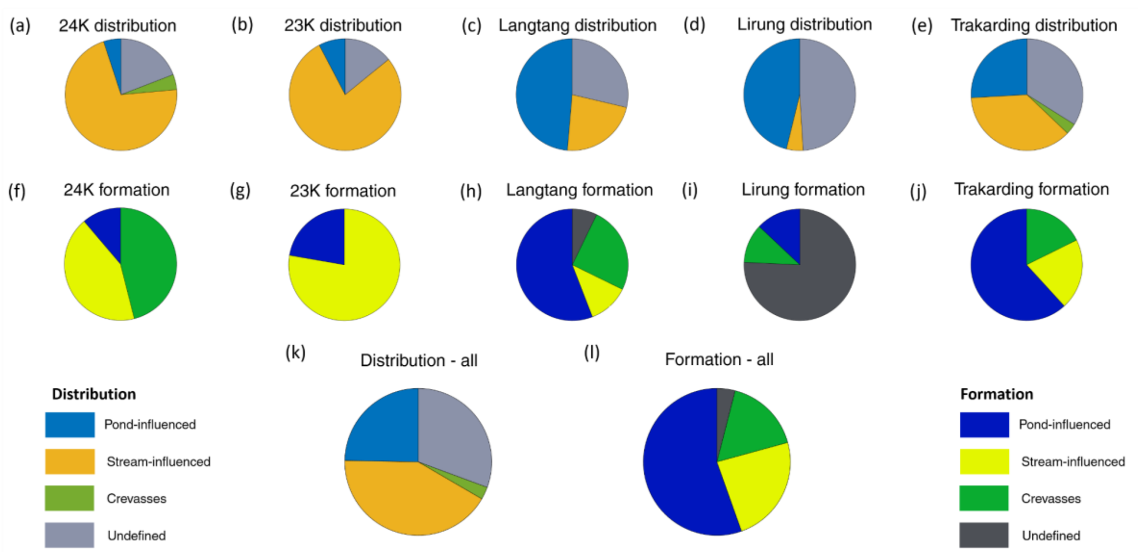

Figure S2. Area proportion of different ice cliff categories within the five UAV survey domains from the total cliff population derived from the Pléiades data (a-e) and from the newly-formed cliffs identified in the multi-temporal UAV data (f-j). (k-l) Combination of all five sites, weighted by the area of the survey domain and the duration of the UAV study period.

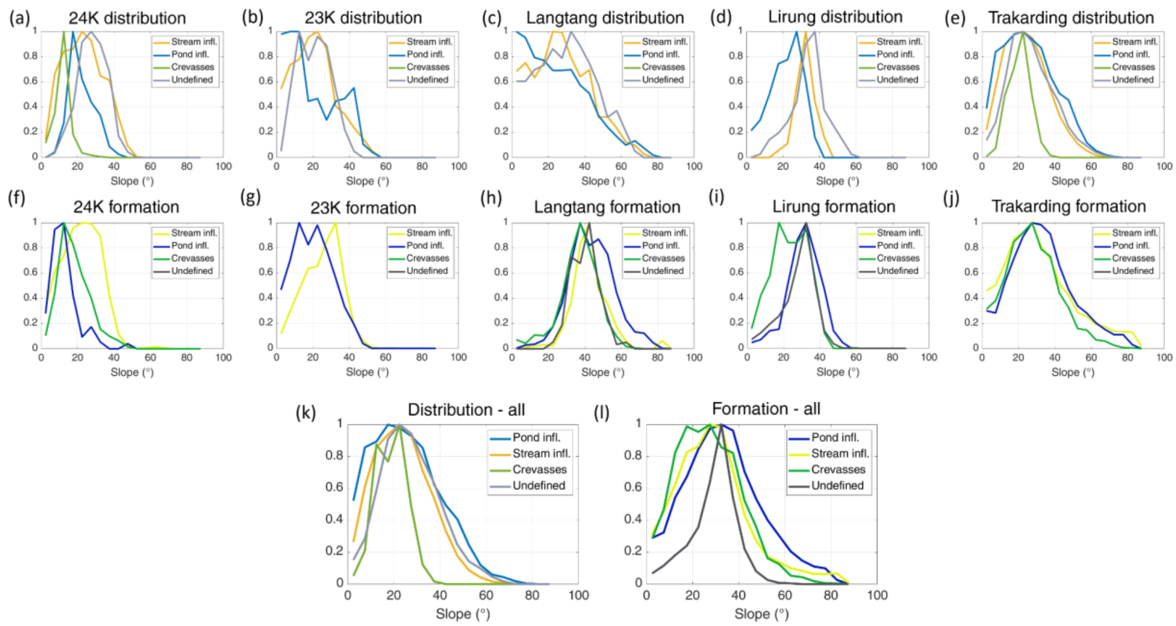

Figure S3: Slope distribution of the pixels of different ice cliff categories within the five UAV survey domains from the total cliff population derived from the Pléiades data (a-e) and from the newly-formed cliffs identified in the multi-temporal UAV data (f-j). (k-l) Combination of all five sites.

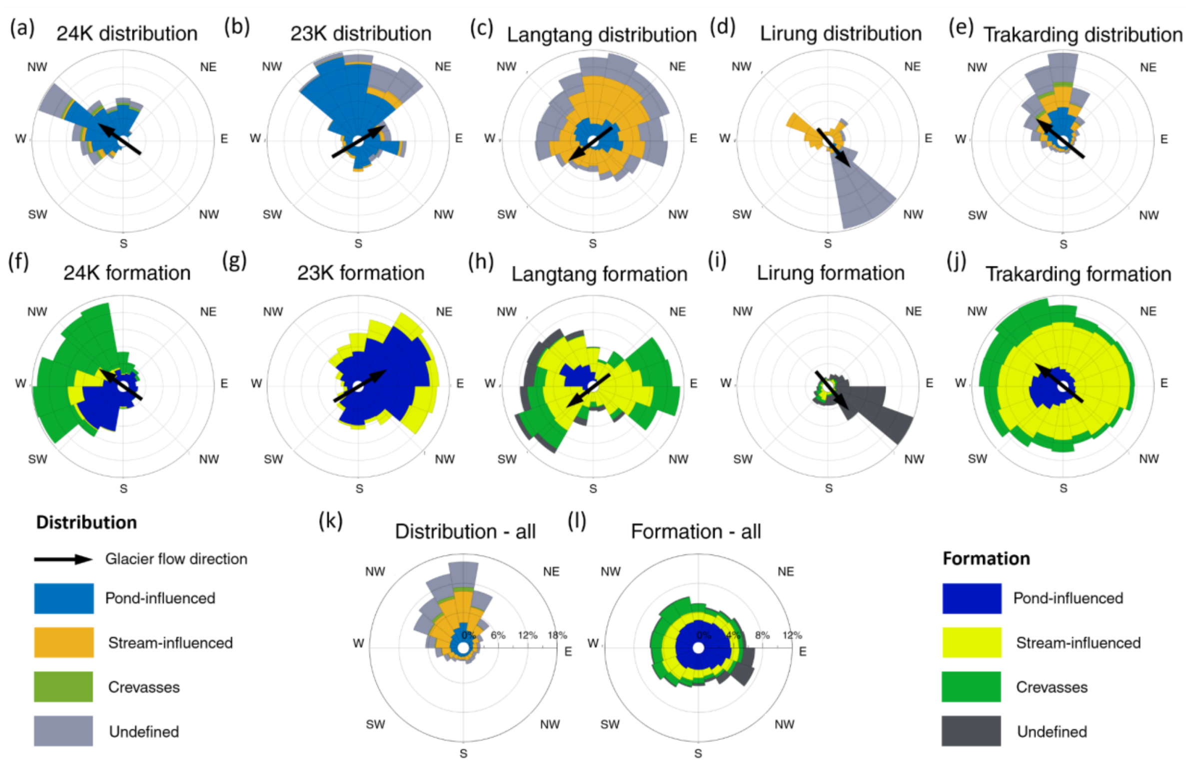

Figure S4: Aspect distribution of the pixels of different ice cliff categories within the five UAV survey domains from the total cliff population derived from the Pléiades data (a-e) and from the newly-formed cliffs identified in the multi-temporal UAV data (f-j). (k-l) Combination of all five sites.

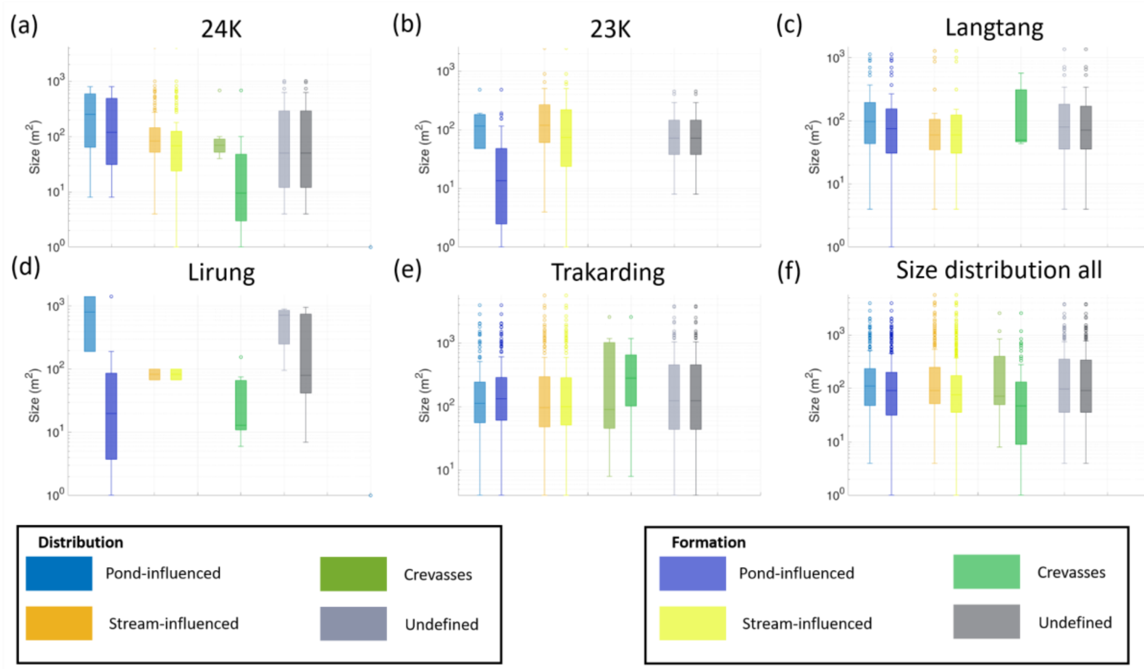

Figure S5: Size distribution of the cliffs of different ice cliff categories within the five UAV survey domains from the total cliff population derived from the Pléiades data and from the newly-formed cliffs identified in the multi-temporal UAV data (a-e). (f) Combination of all five sites.

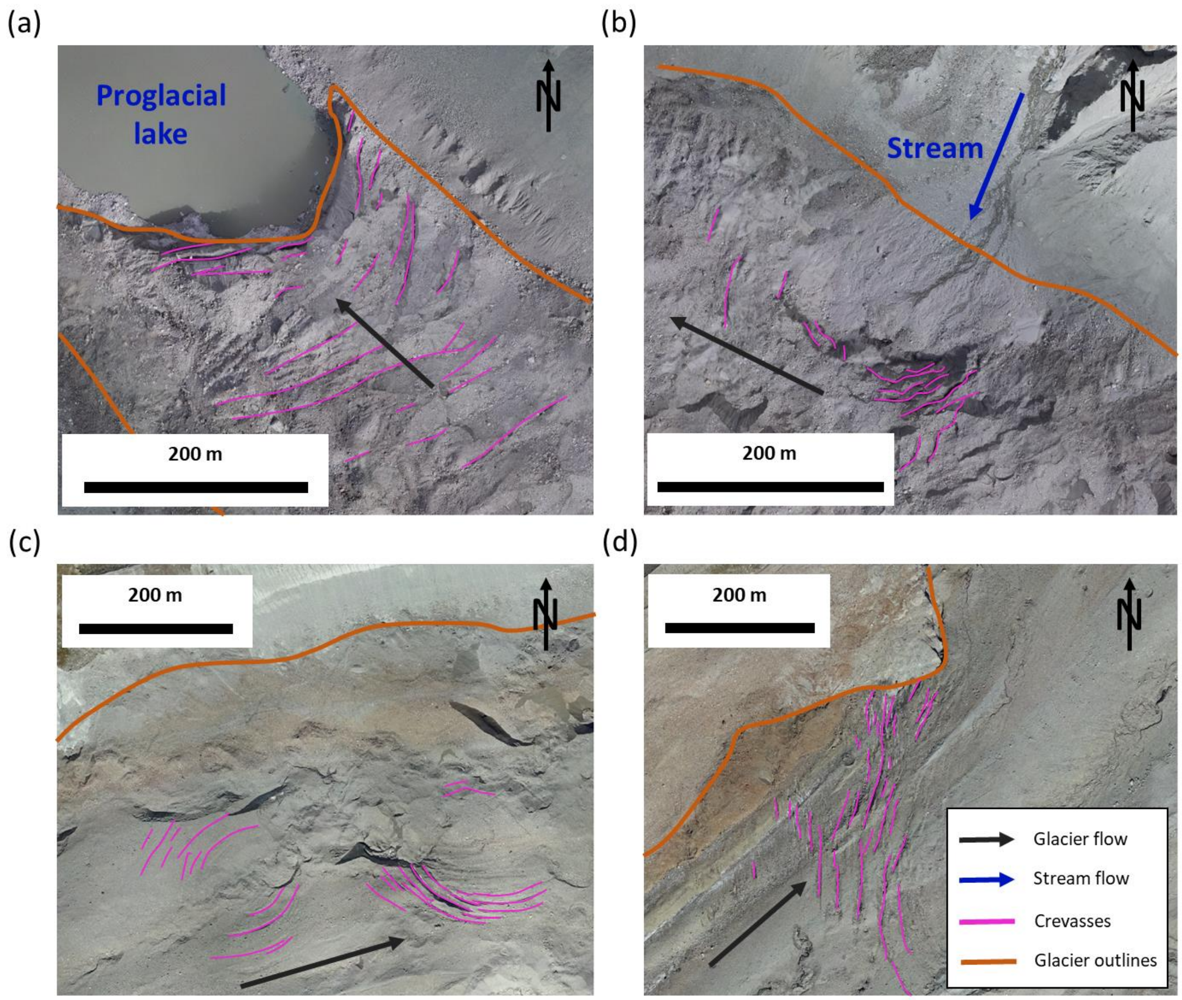

Figure S6: Crevasse patterns on (a-b) Trakarding Glacier, 10/2019 and (c-d) Zmutt Glacier, 09/2018. (a) Influence from a proglacial lake. (b) Stream entering the glacier from the side. (c) Circular crevasses symptomatic of englacial or subglacial conduit, likely preceding a conduit collapse. (d) Simple shear situation at the glacier lateral margins.

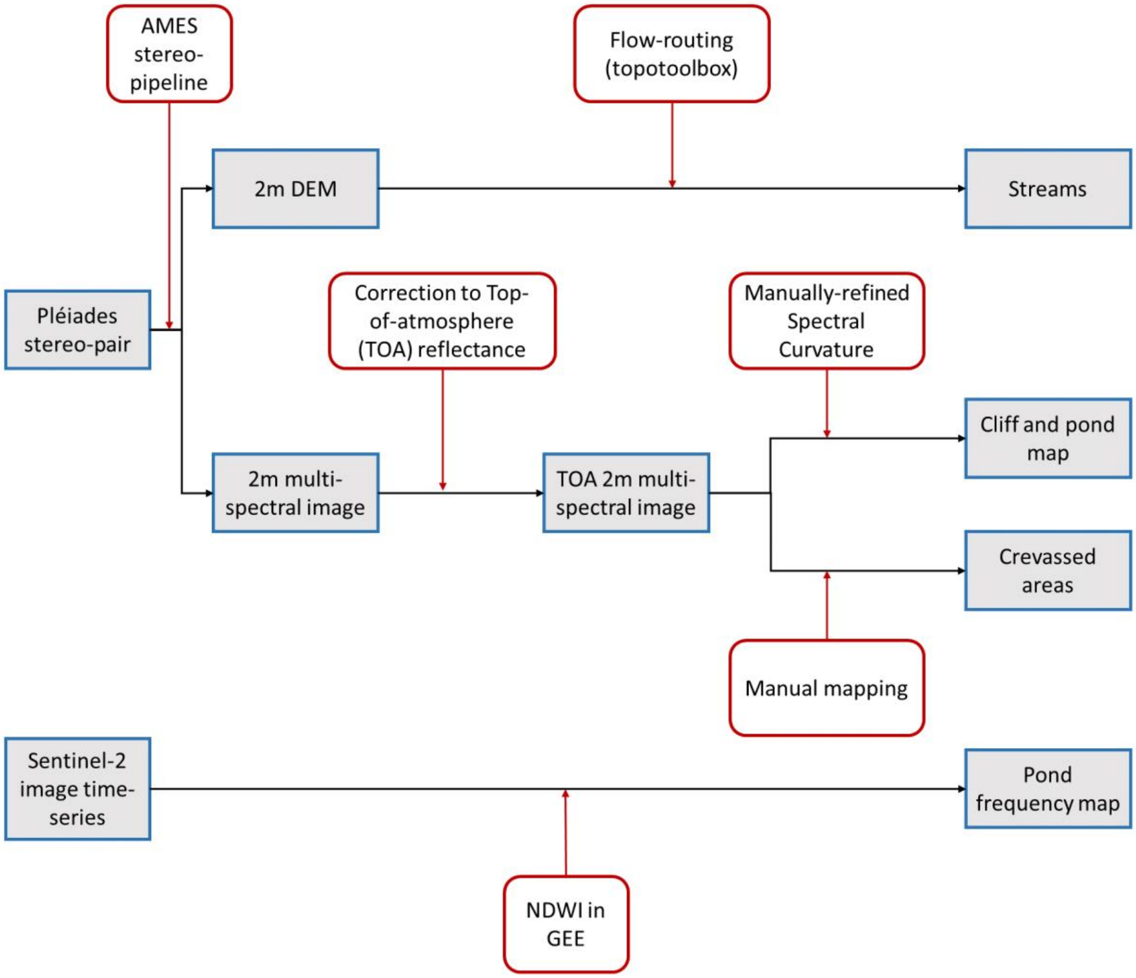

Figure S7: Processing steps of the Pléiades and Sentinel-2 images to obtain final cliff, pond, stream and crevasse maps.

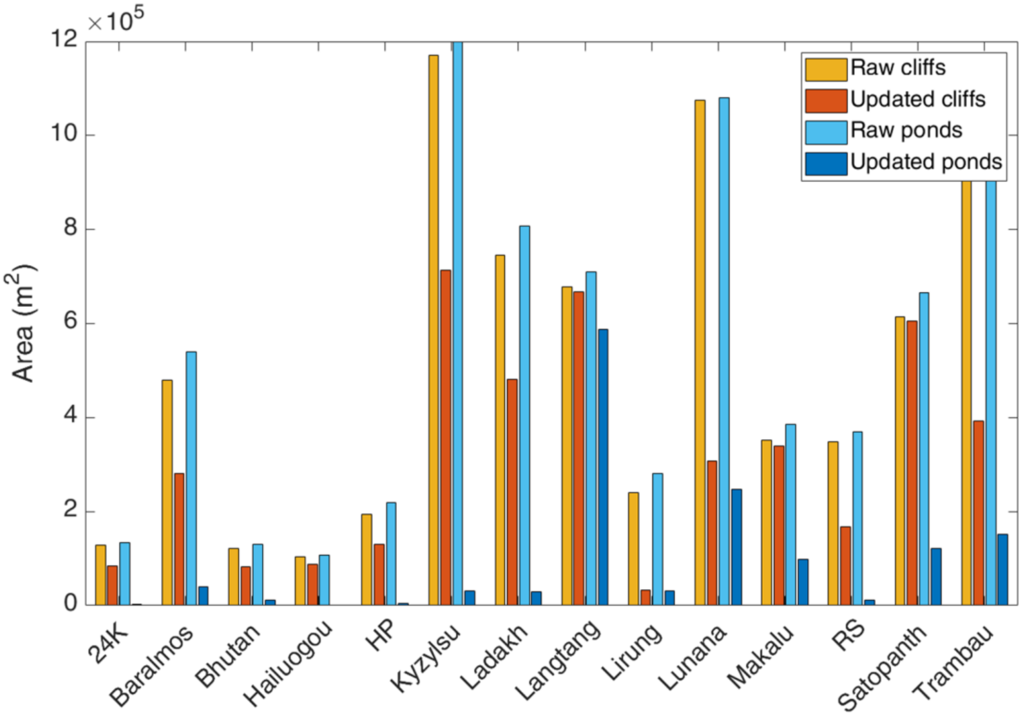

Figure S8: Cliff and pond area before and after manual trimming of automatically derived outlines for each scene.

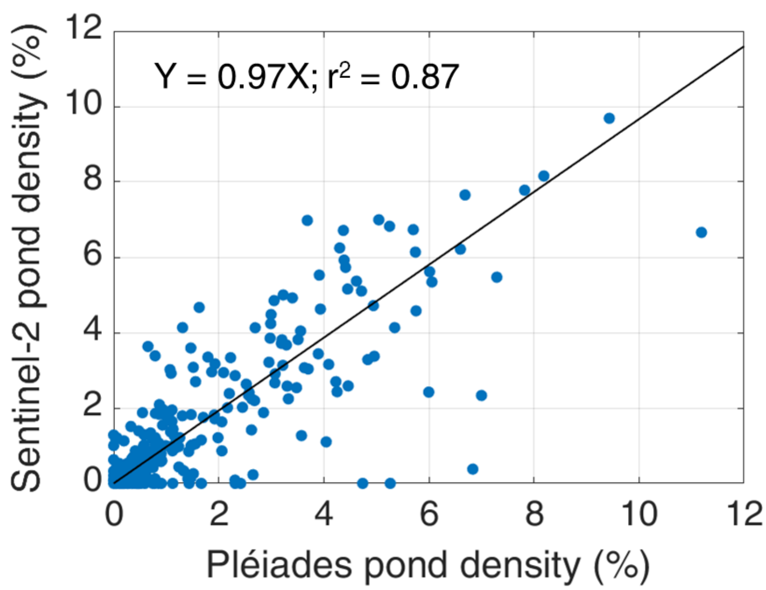

Figure S9: S2 ponds VS Pléiades ponds for each bin.

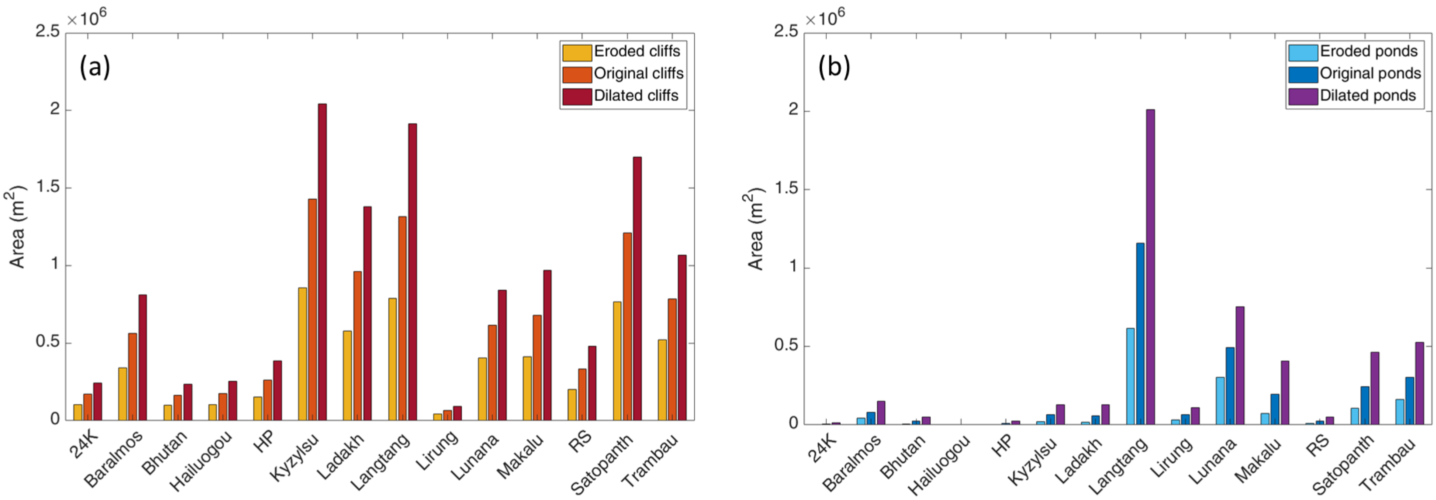

Figure S10: (a) Cliff and (b) pond original, dilated and eroded area for each scene.

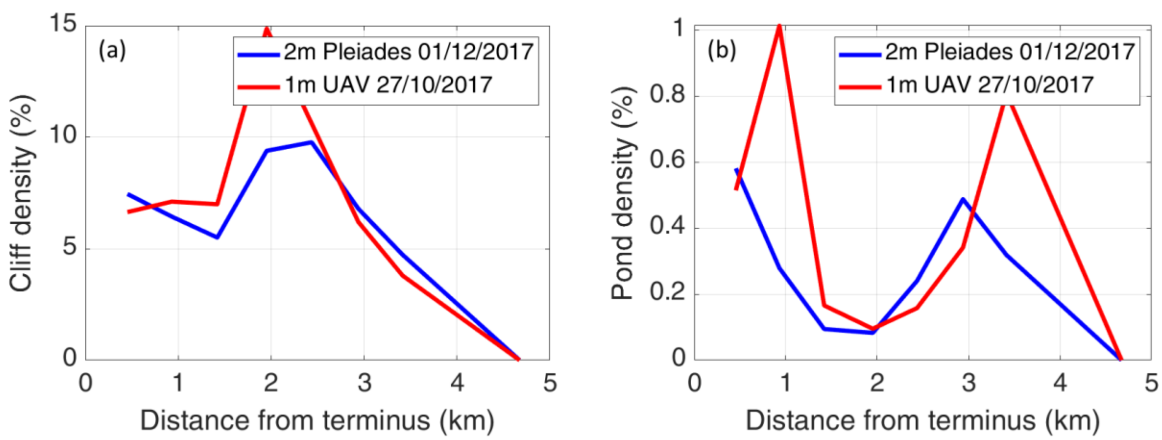

Figure S11: Cliff (a) and pond (b) density on Trakarding Glacier as a function of distance from the terminus calculated based on the Pléiades outlines (01/12/2017) from this study and those independently derived using a 1m UAV orthoimage (27/10/2017).

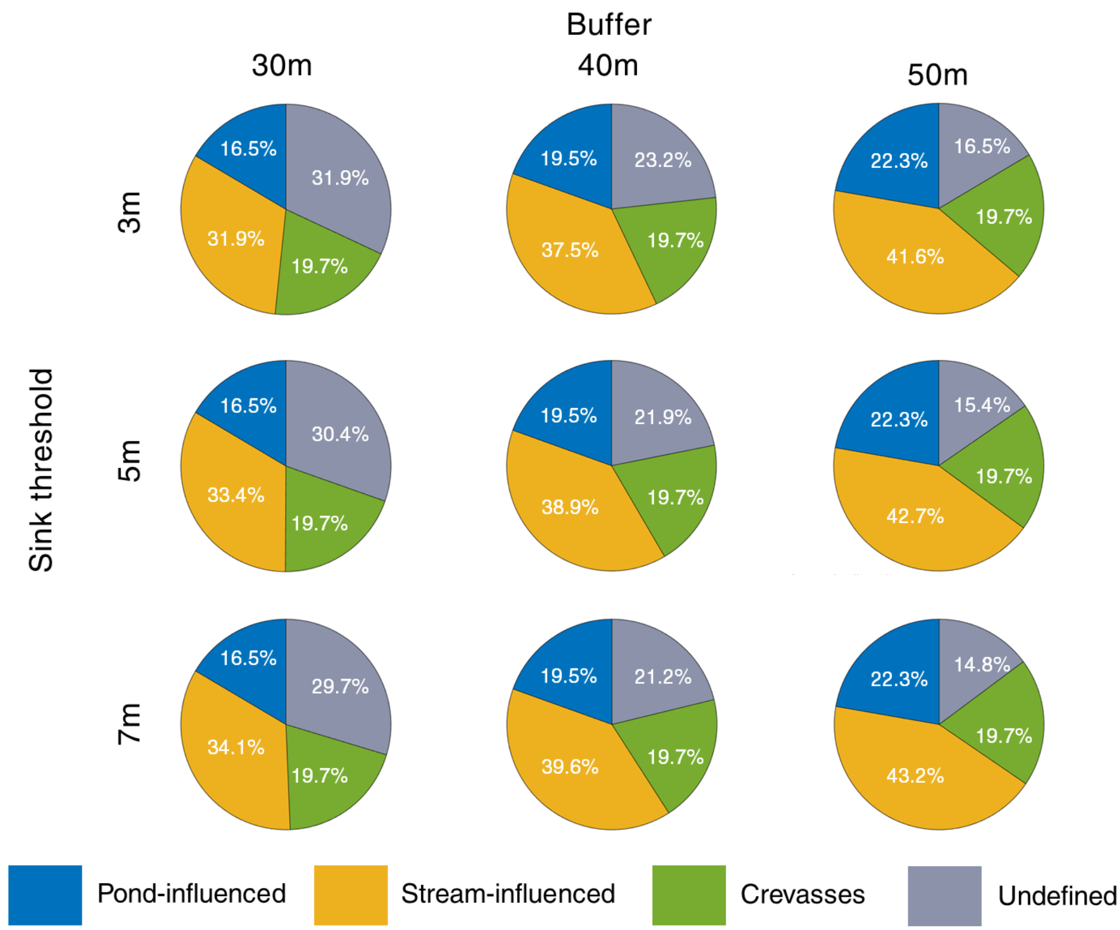

Figure S12: Area proportion of each cliff category depending on the DEM sink filling threshold for the mapping of the streams and the stream and pond buffer, for all cliff pixels.

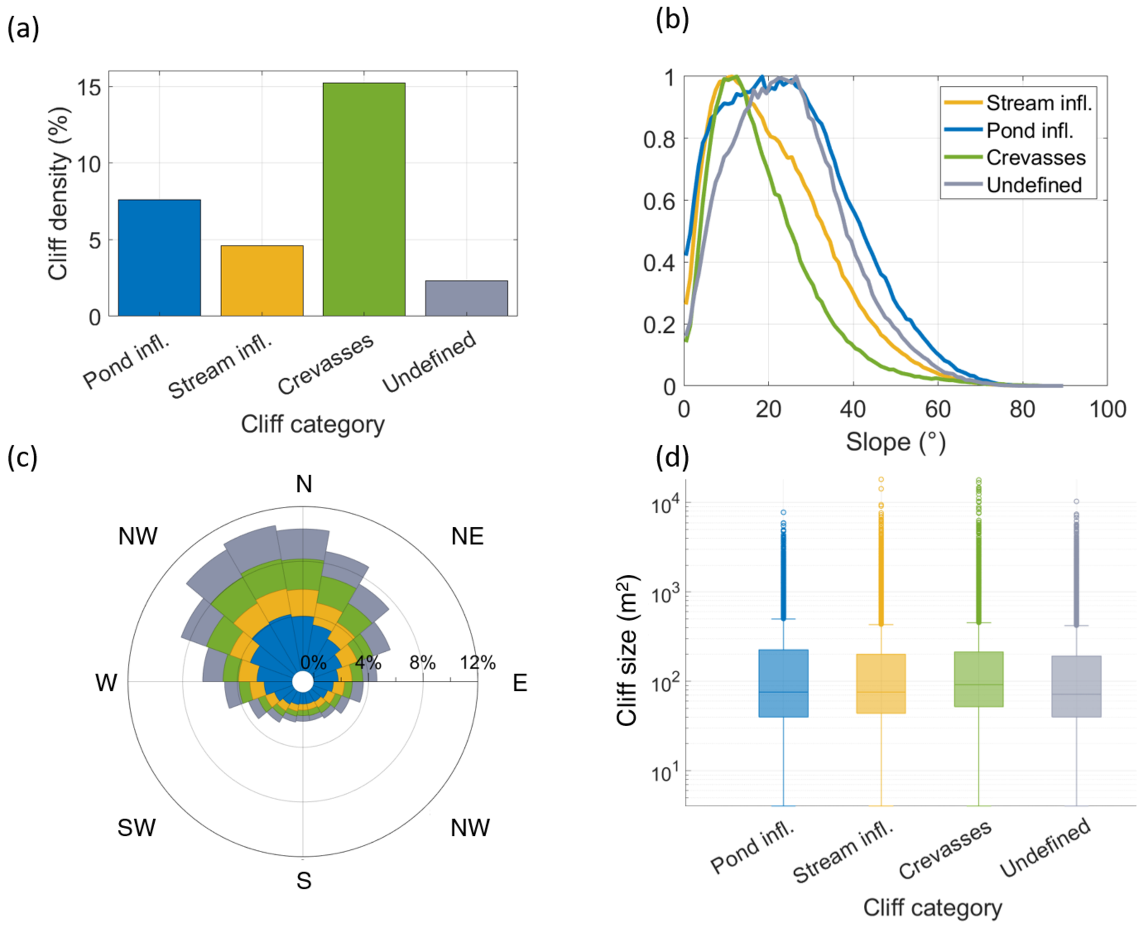

Figure S13: (a) Ice cliff density within buffer areas, (b) normalised slope distribution and (c) aspect distribution for all cliff pixels. (d) Size distribution of individual cliffs (defined as 8-connected objects in the cliff map) showing the median, 25th and 75th percentiles. The circles are considered as outliers.

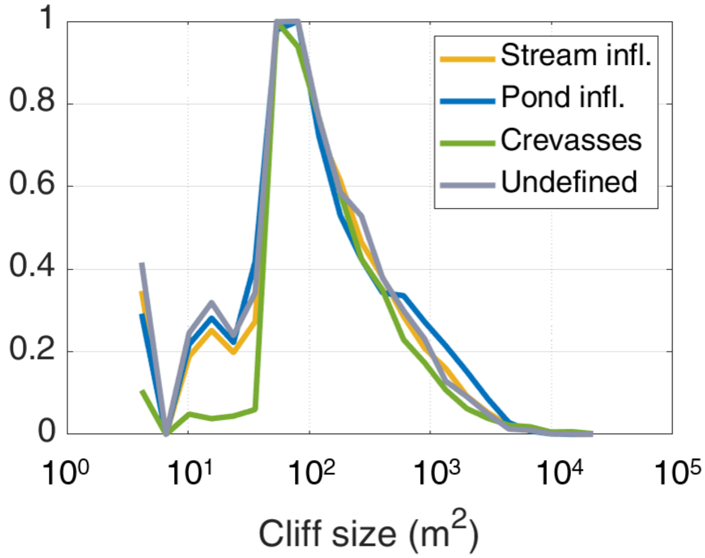

Figure S14: Normalised size distribution of the different cliff categories. The distributions are limited by the resolution of the Pléiades pixels (4 m^2), and the ability of the operator to identify ice cliffs less than ~25 pixels or 100 m^2 (Kneib et al., 2020).

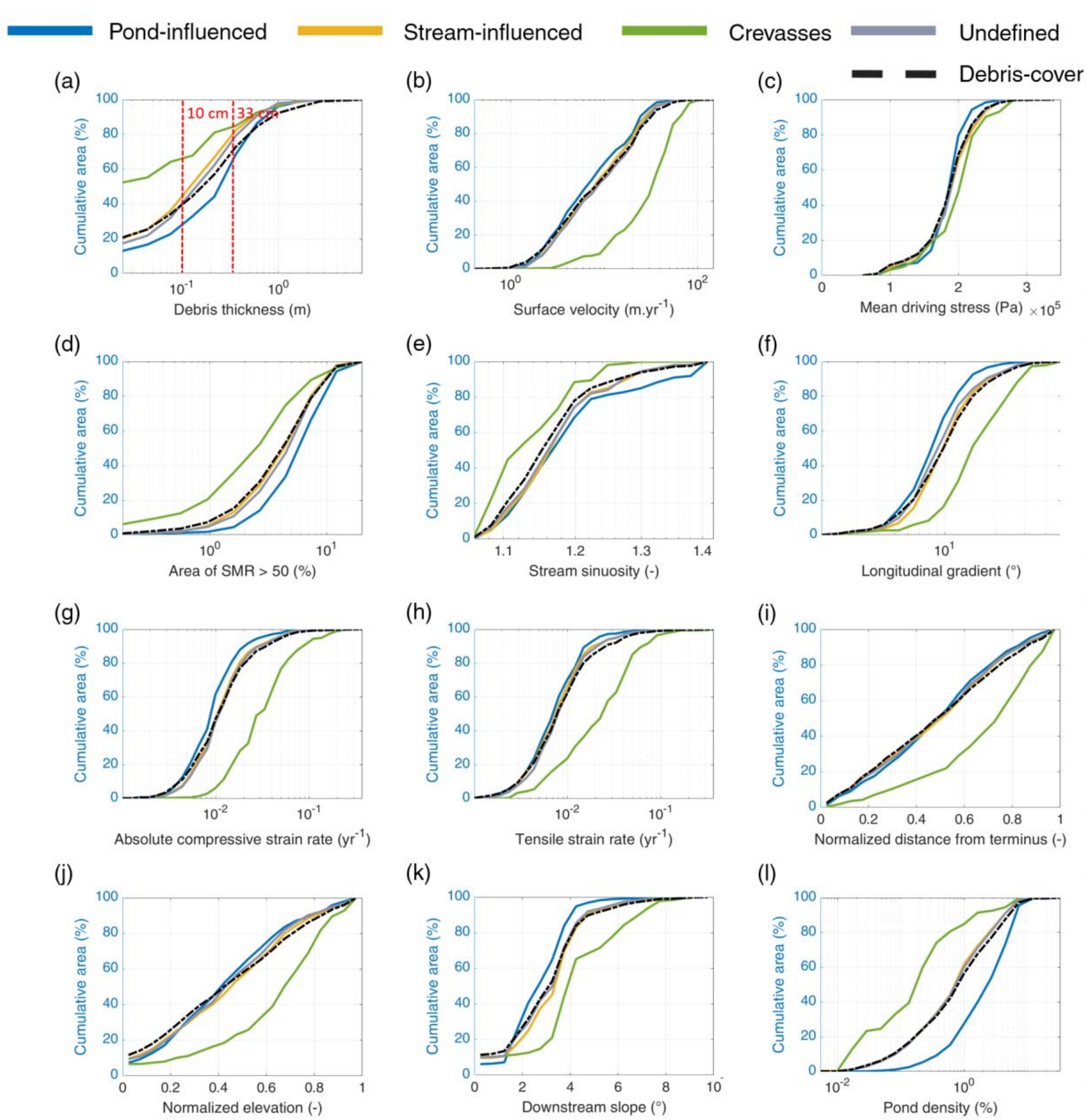

Figure S15: Cliff cumulative area in each category as a function of various metrics for all bins of all glaciers where more than 65% of the debris-covered area could be classified. The black line shows the cumulative area of all the bins.

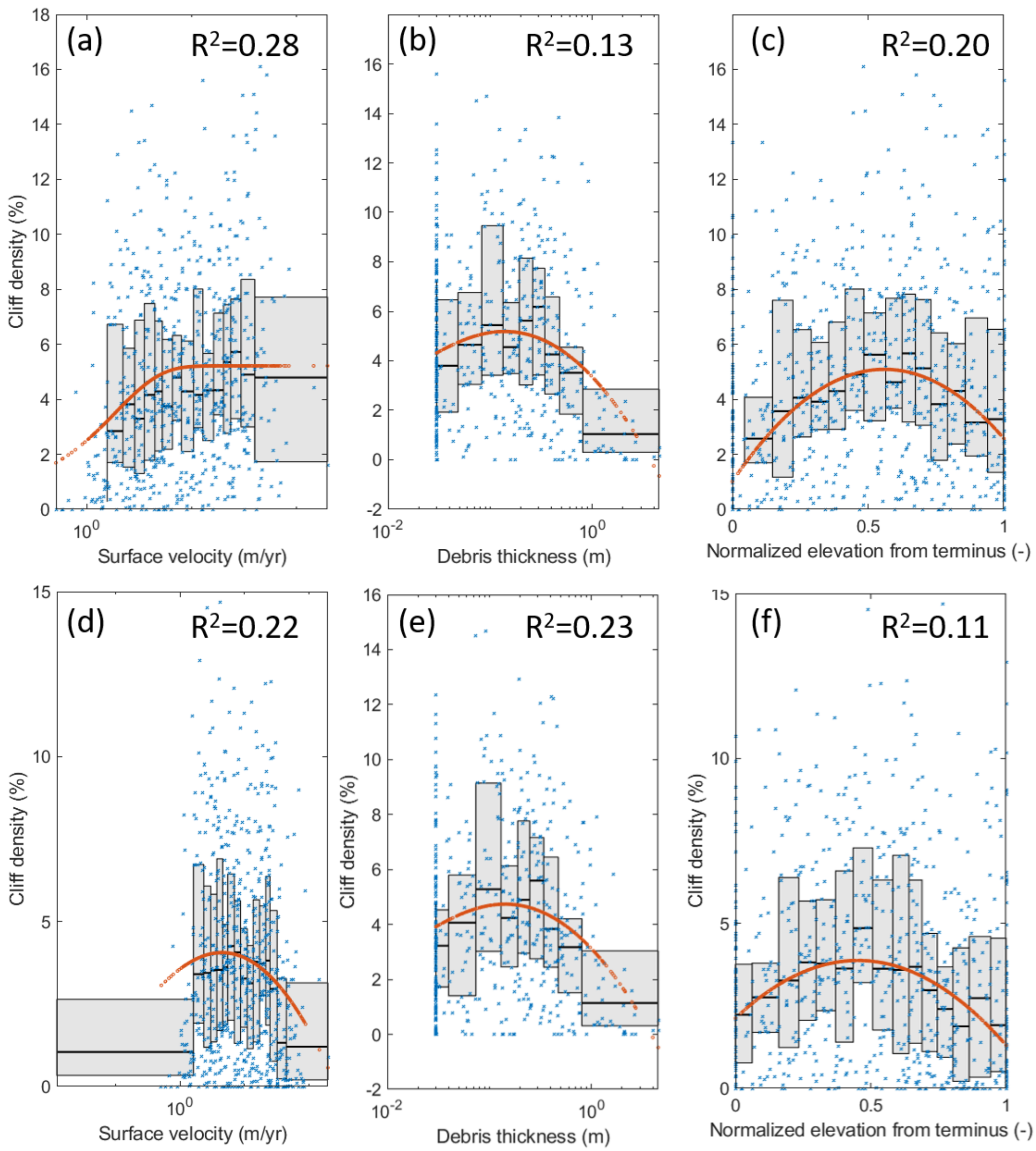

Figure S16: Cliff density with (a-c) and without crevasses (d-f) as a function of (a,d) surface velocity, (b,e) debris thickness and (c,f) normalized elevation from terminus for all bins of all glaciers for which more than 65% of the debris-covered area could be classified. The grey zones indicate the median and the interquartile range where each bin includes one tenth of the data. The red dots show a polynomial fit to the median values and the R^2 the results of this fit for the binned data.

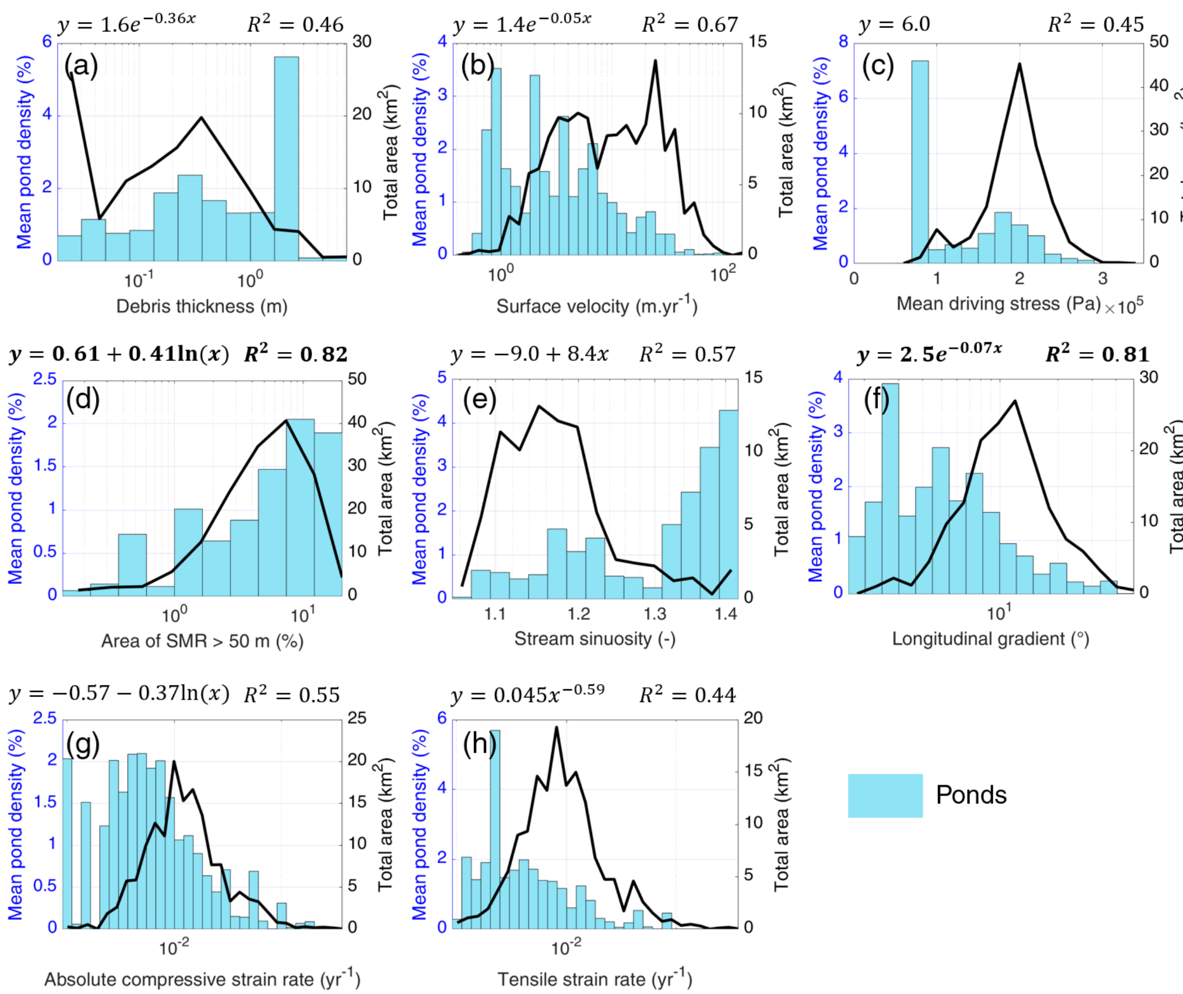

Figure S17: Mean pond density as a function of different variables for all bins of all glaciers where more than 65% of the debris-covered area could be classified: (a) debris thickness, (b) surface velocity, (c) mean driving stress, (d) 'hummockiness', (e) stream sinuosity, (f) longitudinal gradient, (g) absolute compressive strain rate and (h) tensile strain rate. The black line shows the area distribution of all the bins. The equations on top of the plot show the best linear relationships that could be found between the mean pond density (y) and the different variables (x), with their respective R^2 value, only accounting for the points with more than 10 observations. The relationships with an R^2 value higher than 0.8 are indicated in bold.

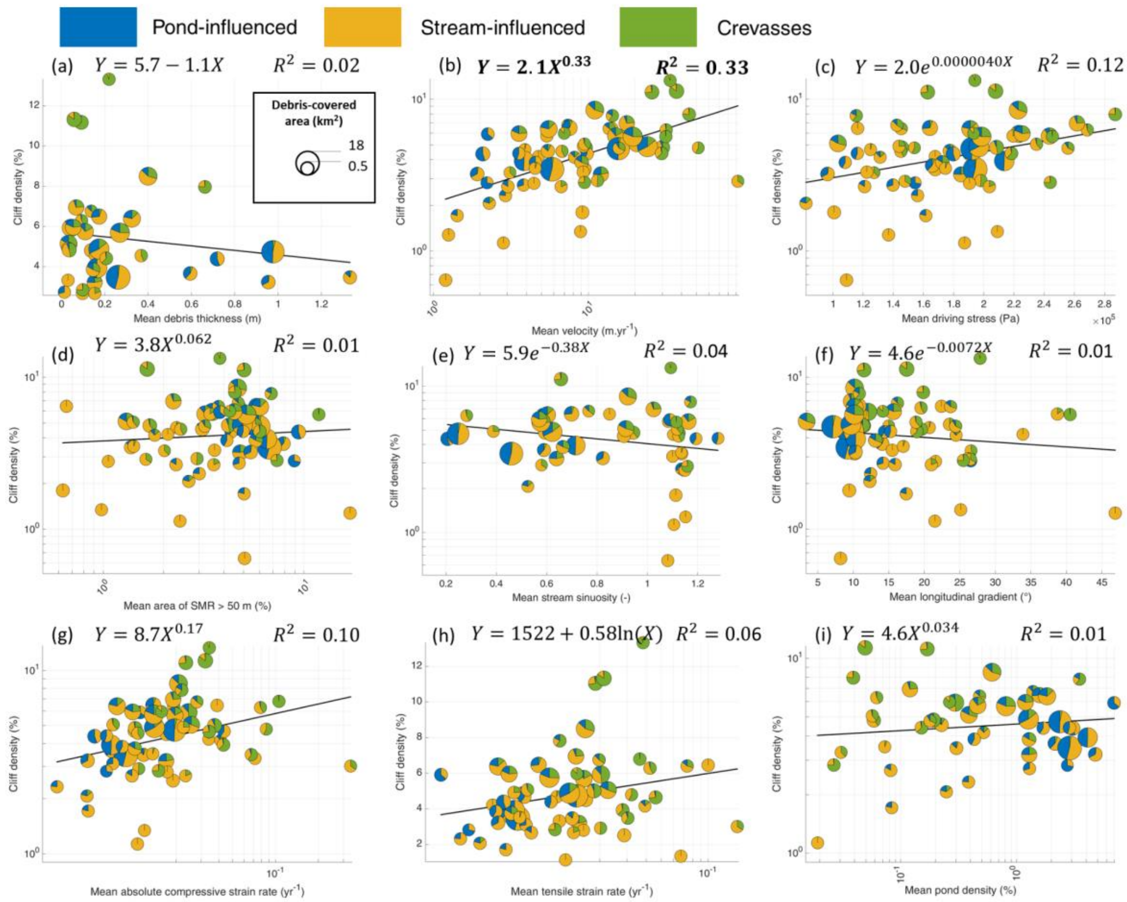

Figure S18: Cliff density for all glaciers where more than 65% of the debris-covered area could be classified, as a function of mean (a) debris thickness, (b) velocity, (c) driving stress, (d) hummockiness, (e) stream sinuosity, (f) longitudinal gradient, (g) compressive strain rate, (h) tensile strain rate, (i) pond density.

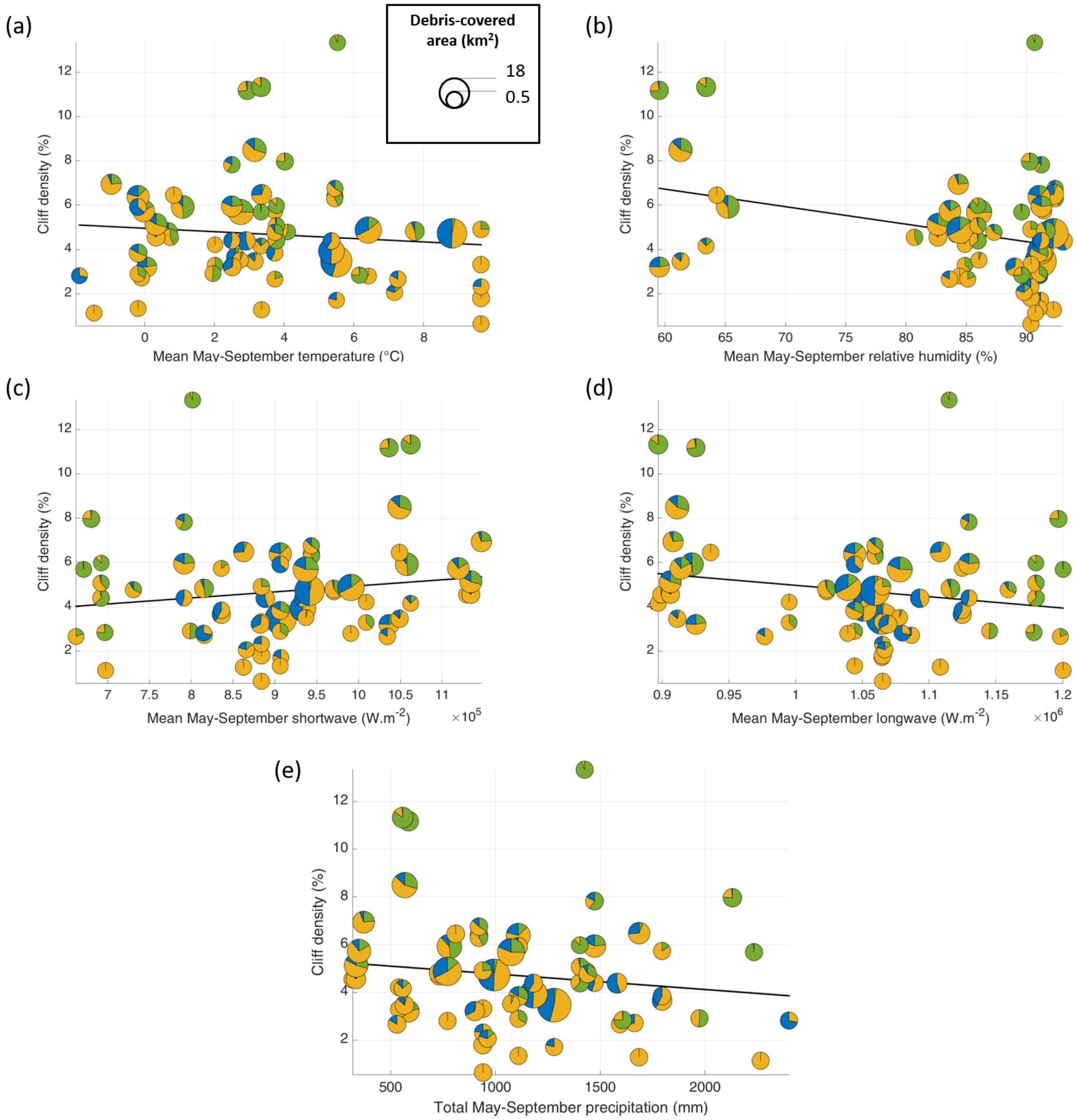

Figure S19: Cliff density for all glaciers where more than 65% of the debris-covered area could be classified, as a function of May-September (a) air temperature, (b) relative humidity, (c) incoming shortwave radiation and (d) incoming longwave radiation. The climatic variables are from ERA5-Land reanalysis data (Muñoz-Sabater et al., 2019), and the air temperature was lapsed to the mean elevation of the debris-covered area considering the mean above-debris lapse rates (-0.0088°C.m^{-1}) following Shaw et al. (2016). The proportion of undefined cliffs was not represented for better readability.

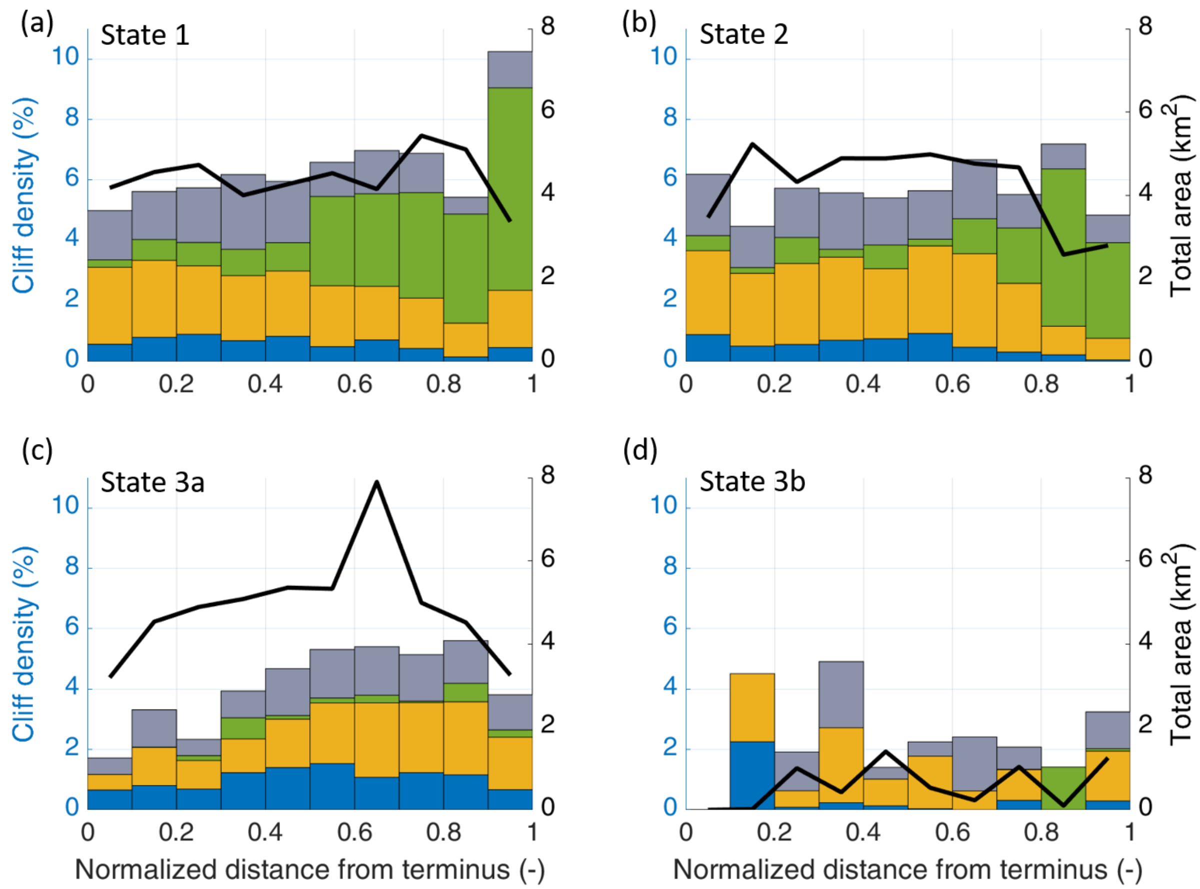

Figure S20: Mean cliff density split by cliff category for all bins of all glaciers where more than 65% of the debris-covered area could be classified as a function of normalized distance from the terminus. The glaciers are split per glacier evolution states (a) 1, (b) 2, (c) 3a and (d) 3b. The categorization is based on the segmentation indicated in blue dashed lines in figure 4.

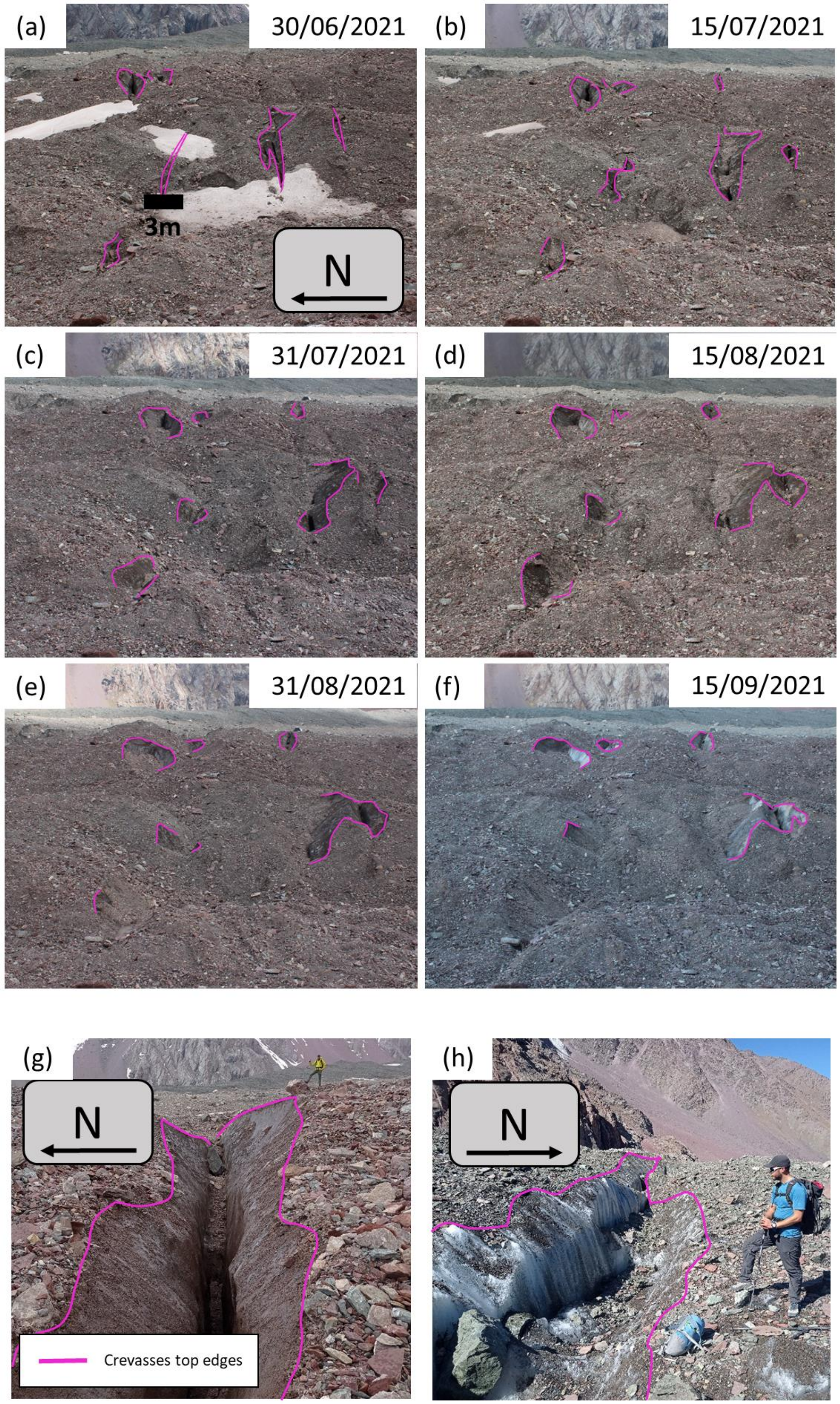

Figure S21: Crevasses on Kyzylsu Glacier (a-f) at bi-weekly time-steps during the 2021 melt season and (g-h) close-up views of other crevasses in September 2021 (image credit: Marin Kneib).

Table S1. Multi-temporal UAV datasets. The Trakarding data are from Sato et al. (2021), the 23K and 24K data are from Chuanxi et al. (in prep) and the Langtang and Lirung data are from Kraaijenbrink et al. (in prep) as well as from Immerzeel et al. (2014) and Brun et al. (2016).

Glacier	UAV survey dates	Original DEM and ortho resolution (m)	Resampled DEM resolution (m)	Survey domain area (km²)	Survey domain (% total debris-covered area)
Trakarding (RGI-15.03448)	27/10/2017	0.2	1	2.9	43
	18/10/2018	0.2			
	18-19/10/2019	0.2			
23K (RGI-15.11752)	27/09/2018	0.08	1	0.51	38
	13/08/2019	0.07			
	12/10/2019	0.07			
	20/08/2020	0.08			
	22/10/2020	0.1			
24K (RGI-15.11758)	27/09/2018	0.09	1	0.59	64
	13/08/2019	0.07			
	12/10/2019	0.07			
	20/08/2020	0.13			
	22/10/2020	0.09			
Langtang (RGI-15.04121)	07/05/2014	0.1	1	1.5	8.2
	22/10/2015	0.1			
	04/05/2016	0.1			
	09/10/2016	0.1			

	26/04/2017	0.1			
	22/10/2017	0.1			
	22/04/2018	0.1			
Lirung (RGI-15.04045)	18/05/2013	0.1	1	0.47	0.49
	22/10/2013	0.1			
	01/05/2014	0.1			
	10/2014	0.25			
	18/10/2015	0.1			
	30/04/2016	0.1			
	06/10/2016	0.1			
	20/04/2017	0.1			
	19/10/2017	0.1			
	28/04/2018	0.1			

Table S2. Pléiades stereo-images used in this study.

Acquisition name	Acquisition date	Location (coordinates of center point)	Number of debris-covered glaciers in scene (>65% of debris-covered area mapped)	Source
24K	20/09/2021	29.77°N, 95.70°E	5	Royal Society
Baralmos	13/09/2021	39.03°N, 71.37°E	4	ERC RAVEN
Bhutan	08/11/2017	28.10°N, 90.27°E	4	PGO
Hailuogou	29/09/2021	29.56°N, 101.94°E	3	Royal Society
HP	12/09/2020	32.25°N, 77.43°E	5	PGO
Kyzylsu	19/09/2021	39.06°N, 71.50°E	5	ERC RAVEN
Ladakh	24/09/2020	33.76°N, 76.30°E	5	PGO
Langtang	14/06/2019	28.28°N, 85.73°E	8	ERC RAVEN
Lirung	13/10/2019	28.23°N, 85.54°E	3	ERC RAVEN
Lunana	07/11/2017	28.12°N, 90.15°E	1	PGO
Makalu	16/10/2018	27.85°N, 87.04°E	7	PGO
RS	15/10/2017	28.76°N, 83.52°E	8	PGO
Satopanth	18/09/2021	30.78°N, 79.35°E	5	ERC RAVEN
Trambau	01/12/2017	27.89°N, 86.51°E	7	PGO

Table S3. Characteristics of each studied glacier. The mean glacier aspect was obtained from the AW3D 30m DEMs (Tadono et al., 2014).

RGI Region	RGI ID	Pléiades scene	Glacier state	Glacier area (km^2)	Debris-covered area (km^2)	Debris-covered area (%)	Area classified (%)	Mean glacier aspect (°)	Cliff density (%)	Pond density (%)
13	19878	Baralmos	2	30.04	8.33	28	74	-62	5.6	0.1
13	19863	Baralmos		8.57	3.81	44	16	4	6.7	0.1
13	18355	Baralmos		1.39	0.23	17	63	-177	2.9	0
13	19836	Baralmos	2	1.65	0.88	53	81	-75	4.8	0

13	19851	Baralmos	2	7.77	5.01	64	93	-3	2.9	1.0
13	19833	Baralmos		1.69	1	59	88	-56	1.0	0
15	02369	Bhutan		4.92	1.44	29	46	156	6.4	0.6
15	02370	Bhutan	1	1.98	0.26	13	71	-177	4.7	0
15	02372	Bhutan	2	1.74	0.76	44	91	-151	5.4	0.2
15	02373	Bhutan	1	10.71	0.65	6	87	-108	5.9	0.1
15	02375	Bhutan	2	5.1	0.77	15	88	-70	6.4	0.9
14	15547	Himachal Pradesh	3a	2.6	0.55	21	68	-99	4.7	0
14	15491	Himachal Pradesh		5.51	1.72	31	41	-66	2.2	0.1
14	15536	Himachal Pradesh	2	4.48	2.73	61	94	-32	4.7	0.1
14	15988	Himachal Pradesh		15.04	4.04	27	54	-17	2.0	0
14	15471	Himachal Pradesh	3a	0.62	0.17	27	97	-17	3.1	0
14	15990	Himachal Pradesh		14.42	1.96	14	55	-14	1.9	0
14	15989	Himachal Pradesh		9.29	2.08	22	51	135	1.4	0.3
14	15437	Himachal Pradesh	3a	1.03	0.1	10	85	-110	4.1	0
14	15991	Himachal Pradesh		3.37	0.76	23	83	-61	3.7	0
13	19847	Kyzylsu	1	9.77	3.01	31	95	-4	10.9	0.1
13	19824	Kyzylsu	2	3.73	2.07	55	98	-24	3.3	0.2
13	18354	Kyzylsu	2	22.76	9.11	40	91	10	8.0	0.2
13	19807	Kyzylsu	1	12.69	4.06	32	85	-11	11.2	0
13	18358	Kyzylsu	2	0.52	0.34	65	87	29	3.8	0.2
14	18750	Ladakh	1	34.1	5.37	16	75	32	6.7	0.1
14	18904	Ladakh	3a	2.92	1.02	35	72	-18	4.5	0
14	18909	Ladakh	3a	14.58	2.76	19	72	41	4.4	0.1
14	18948	Ladakh	1	69.97	7.55	11	70	26	4.7	0.3
14	18940	Ladakh	2	22.25	6.97	31	89	43	5.4	0.2
15	09457	Langtang		12.32	5.6	45	50	-95	2.6	1.3
15	04119	Langtang	3a	13.65	2.88	21	97	159	3.0	1.8
15	04121	Langtang	3a	54.8	18.23	33	100	-173	3.0	2.2
15	09474	Langtang	3a	24.79	11.69	47	88	160	3.3	3.4
15	09476	Langtang	2	3.73	1.19	32	108	-161	1.9	7.2
15	04036	Langtang	3b	1.3	0.65	50	74	116	1.7	0.1
15	09475	Langtang	3a	4.35	3.41	78	94	80	3.5	2.5
15	04176	Langtang	2	19.9	5.08	26	106	-81	5.9	1.3
15	04308	Langtang	3b	1.22	0.73	60	108	-74	1.0	0.1

15	03957	Lirung	2	0.68	0.48	71	76	-175	2.9	0
15	04045	Lirung	3a	6.33	0.96	15	92	156	3.4	0.3
15	03956	Lirung	3a	1.45	0.7	48	79	-156	1.3	0
15	09457	Lirung		12.32	5.6	45	36	-95	1.0	0.9
15	02358	Lunana	2	11.23	7.16	64	37	136	0.8	4.0
15	02229	Lunana		32.47	15.96	49	93	179	4.0	1.3
15	03401	Makalu	2	7.28	2.81	39	80	-124	3.6	0.8
15	03378	Makalu	3b	2.81	0.74	26	78	-110	2.2	1.2
15	03366	Makalu		26.5	3.01	11	49	124	6.9	0.3
15	03849	Makalu	3a	0.55	0.28	51	96	171	2.3	1.9
15	03372	Makalu	1	1.44	0.51	35	73	67	2.7	0
15	03727	Makalu	3b	0.92	0.45	49	76	15	4.3	0
15	03619	Makalu	3a	30.73	7.9	26	90	119	5.8	1.1
15	03728	Makalu	3a	9.88	1.45	15	80	-120	3.9	1.2
15	04870	Rikha Samba	2	4.77	1.05	22	70	-59	4.8	0
15	04591	Rikha Samba	3b	3.04	1.07	35	74	168	0.7	0.4
15	04843	Rikha Samba	3b	6.69	1.73	26	82	93	2.1	0.1
15	04411	Rikha Samba	3b	1.77	0.65	37	88	139	2.1	0.3
15	04410	Rikha Samba	3b	1.59	0.76	48	95	10	1.9	0.2
15	04854	Rikha Samba	2	4.88	0.78	16	88	-126	4.9	0.1
15	04830	Rikha Samba	1	30.93	3.49	11	90	-95	4.7	0.4
15	04568	Rikha Samba	1	6.33	0.66	10	71	79	12.8	0
15	07122	Satopanth	1	34.86	12.42	36	91	97	4.3	0.7
15	07190	Satopanth	3b	1.22	0.37	30	83	180	2.8	0
15	06942	Satopanth	3a	1.7	0.46	27	89	-4	3.6	0.1
15	07123	Satopanth		19.27	4.77	25	64	42	6.3	0.2
15	06861	Satopanth	3b	3.29	1.07	33	68	35	2.5	0.1
15	07122	Satopanth	1	22.95	10.95	48	89	57	5.1	0.4
15	03776	Trambau		0.41	0.18	44	83	-112	2.1	0.3
15	03782	Trambau	3b	1.73	0.59	34	93	170	1.1	0
15	03531	Trambau		1.41	1.06	75	52	-111	3.2	0.6
15	03498	Trambau		3.31	1.18	36	38	-139	3.2	0
15	03448	Trambau		30.97	6.69	22	57	-99	6.0	0.7
15	03943	Trambau	1	1.99	0.81	41	76	-166	7.1	2.6
15	03926	Trambau	3a	1.19	0.86	72	89	169	3.3	2.1
15	03428	Trambau	3a	15.97	6.09	38	68	-136	5.5	0.7

15	03435	Trambau	3a	4.7	2.73	58	95	77	2.9063	3.4
15	09771	Trambau		19.74	5.13	26	39	-143	7.0	0.1
15	09764	Trambau		1.62	0.53	33	81	149	2.0	1.0
15	11750	24K	3b	3.14	0.67	21	100	-3	2.7	0
15	11752	24K	1	4.07	1.34	33	100	85	4.2	0.1
15	11758	24K	2	1.97	0.92	47	100	-66	4.9	0.1
15	11765	24K	2	1.31	0.69	53	100	47	4.6	0.1
15	11760	24K	3a	1.33	0.3	23	100	-11	5.8	0.4
15	07886	Hailuogou	1	19.07	1.57	8	100	93	7.8	0
15	07889	Hailuogou	2	5.44	0.92	17	100	69	2.8	0
15	07894	Hailuogou	1	1.25	0.65	52	100	70	4.4	0

Table S4: Mean and standard deviation of the lognormal distribution of cliff size for the different cliff categories.

Cliff category	Mean	Standard deviation
All	4.46	1.39
Pond-influenced	4.50	1.46
Stream-influenced	4.44	1.41
Crevasses	4.72	1.18
Undefined	4.34	1.42

Table S5: Best fitting relationships between binned density of different cliff categories (As shown in Fig. 4) and different predictors. Highlighted in green, blue and yellow are respectively the best, second best and third best relationships (based on R^2).

Cliff type	Velocity	Debris thickness	Longitudinal gradient	Driving stress	Pond density
All	R^2=0.73 Y = 3.7+0.10X	R^2=0.94 $Y = 6.0e^{-0.48X}$	R^2 =0.17 Y = 3.2+0.73ln(X)	R^2=0.58 $Y = 2.9+(1.3x10^{-5})X$	R^2=0.12 $Y =5.0e^{-0.013X}$
Pond-infl.	R^2 =0.34 $Y = 0.94e^{-0.019X}$	R^2 =0.27 $Y = 0.95e^{-0.28X}$	R^2=0.88 $Y = 1.8e^{-0.084X}$	R^2=0.15 $Y = 1.1e^{-0.0000036X}$	R^2=0.95 $Y = 0.74X^{0.59}$
Stream-infl.	R^2=0.08 Y = 2.0-0.0099X	R^2=0.86 $Y = 2.5e^{-0.48X}$	R^2=0.03 Y = 1.8-0.0078X	R^2=0.07 $Y=1.7+(2.0x10^{-6})X$	R^2=0.74 $Y = 2.2e^{-0.053X}$
Crevasses	R^2=0.83 Y = -0.65+0.12X	R^2=0.24 Y = 0.32-0.15ln(X)	R^2=0.52 $Y = 0.11X^{0.87}$	R^2=0.36	R^2=0.60 $Y = 0.23X^{-0.51}$

				$Y = -1.0+(1.3\text{x}10^{-5})X$	
Undefined	$R^2=0.14$ $Y = 0.94X^{0.14}$	$R^2=0.74$ $Y = 1.9e^{-0.57X}$	$R^2=0.21$ $Y = 1.5e^{-0.012X}$	$R^2=0.01$ $Y = 1.4+(3.0\text{x}10^{-7})X$	$R^2=0.58$ $Y = 1.6e^{-0.052X}$

Cliff type	Absolute compressive strain rate	Tensile strain rate	Hummockiness	Stream sinuosity	Normalized distance from terminus
All	$R^2=0.82$ $Y = 11+1.3\ln(X)$	$R^2=0.55$ $Y = 11X^{0.15}$	$R^2=0.60$ $Y = 5.0X^{0.038}$	$R^2=0.08$ $Y = 3.1e^{0.44X}$	$R^2=0.77$ $Y = 4.1e^{0.51X}$
Pond-infl.	$R^2=0.62$ $Y = 1.0e^{-20X}$	$R^2=0.82$ $Y = 1.1e^{-34X}$	$R^2=0.93$ $Y = 0.26+0.076X$	$R^2=0.22$ $Y = 0.42X^{2.5}$	$R^2=0.09$ $Y = 0.85+0.065\ln(X)$
Stream-infl.	$R^2=0.03$ $Y = 2.1X^{0.04}$	$R^2=0.74$ $Y = 2.4e^{-16X}$	$R^2=0.22$ $Y = 1.5X^{0.083}$	$R^2=0.23$ $Y = 1.4+4.9\ln(X)$	$R^2=0.02$ $Y = 2.0e^{-0.065X}$
Crevasses	$R^2=0.88$ $Y = 403X^{1.6}$	$R^2=0.84$ $Y = -0.17+103X$	$R^2=0.72$ $Y = 1.8-0.44\ln(X)$	$R^2=0.12$ $Y = 2.1X^{-6.8}$	$R^2=0.84$ $Y = 0.18e^{2.9X}$
Undefined	$R^2=0.14$ $Y = 1.9X^{0.092}$	$R^2=0.42$ $Y = 1.6e^{-8.7X}$	$R^2=0.54$ $Y = 1.0X^{0.15}$	$R^2=0.01$ $Y = 2.2e^{-0.39X}$	$R^2=0.02$ $Y = 1.4e^{-0.075X}$

Cliff type	Normalized elevation	Downstream slope
All	$R^2=0.59$ $Y = 6.0X^{0.17}$	$R^2=0.64$ $Y = 4.1e^{0.077X}$
Pond-infl.	$R^2=0.09$ $Y = 0.92e^{-0.36X}$	$R^2=0.51$ $Y = 1.3-0.17X$
Stream-infl.	$R^2=0.05$ $Y = 2.0+0.087\ln(X)$	$R^2=0.05$ $Y = 2.10e^{-0.030X}$
Crevasses	$R^2=0.72$ $Y = 0.18e^{2.8X}$	$R^2=0.69$ $Y = -1.1+0.68X$
Undefined	$R^2=0.02$ $Y = 1.4e^{-0.13X}$	$R^2=0.15$ $Y = 1.6e^{-0.041X}$